American University in Cairo

AUC Knowledge Fountain

Theses and Dissertations

Student Research

Spring 2-22-2020

Novel On-chip Optical Modulator Designs

Mohamed Mahmoud Ibrahim Ibrahim Elsayed
The American University in Cairo AUC

Follow this and additional works at: https://fount.aucegypt.edu/etds

Part of the Hardware Systems Commons

Recommended Citation

APA Citation
Elsayed, M. M. (2020).*Novel On-chip Optical Modulator Designs* [Master's Thesis, the American University in Cairo]. AUC Knowledge Fountain.
https://fount.aucegypt.edu/etds/1769

MLA Citation
Elsayed, Mohamed Mahmoud Ibrahim Ibrahim. *Novel On-chip Optical Modulator Designs*. 2020. American University in Cairo, Master's Thesis. *AUC Knowledge Fountain*.
https://fount.aucegypt.edu/etds/1769

This Master's Thesis is brought to you for free and open access by the Student Research at AUC Knowledge Fountain. It has been accepted for inclusion in Theses and Dissertations by an authorized administrator of AUC Knowledge Fountain. For more information, please contact thesisadmin@aucegypt.edu.

The American University in Cairo

School of Sciences and Engineering

Nanotechnology Department

M. Sc. Thesis

Novel On-chip Optical Modulator Designs

A thesis submitted in partial fulfilment of the requirements of the degree of Master of Science in Nanotechnology

Presented By:

Mohamed Mahmoud Ibrahim Ibrahim Elsayed

Supervised By:

Associate Prof. Mohamed Abdel Azim Swillam

J A N – 2 0 2 0

The American University in Cairo

School of Sciences and Engineering

Nanotechnology Department

Novel On-chip Optical Modulator Designs

Mohamed Mahmoud Ibrahim Ibrahim Elsayed

Examiners Committee

Name	Signature
Dr. Mohamed Swillam (Advisor) Associate Professor, Physics Department, AUC	____________________
Dr. Ahmed Mahmoud (Internal Examiner) Assistant Professor, Electronics & Communications Department, AUC	____________________
Dr. Mahmoud A. Abdalla (External Examiner) Associate Professor, Electromagnetic Waves Group, Electronic Engineering Department, MTC, College	____________________
Dr. Ehab El Sawy (Moderator) Assistant Professor, Chemistry Department, AUC	____________________

____________________ ____________________

Program Director Dean

DECLARATION

I hereby certify that this material, which I now submit for assessment on the programme of study leading to the award of **Master of Science in Nanotechnology** is entirely my own work, that I have exercised reasonable care to ensure that the work is original, and does not to the best of my knowledge breach any law of copyright, and has not been taken from the work of others save and to the extent that such work has been cited and acknowledged within the text of my work.

Signed: ______________________________

Student ID No.: ______________________________

Date: ______________________________

To Nourhan, my amazing wife, whose sacrificial care for me and our children made it possible for me to complete this work. To our children, Layan and Yaseen, who are the fruits of our lives and our source of inspiration. To the soul of our son, Karim, may Allah bring us together to hold him in our hands one more time.

ACKNOWLEDGMENT

First of all, I would like to thank almighty Allah for granting me the strength to accomplish this work. I would like also to express my deepest gratitude to my supervisor, mentor, teacher, and older brother **Dr. Mohamed Swillam** for his constant support and guidance academically and personally. Moreover, my sincere thanks to the **AUC**, the **SSE faculty members** and the **Nanotechnology program staff** as well. Thank you from my heart to my colleagues and all the past and present member of **NRL group** who were always like family to me. This work was made possible by an NPRP award from the Qatar National Research Fund (member of **Qatar Foundation**), so thank you to them as well.

No words can describe my gratitude towards **my parents** who sacrificed a lot to make me the man who I am today. **My younger brothers** and their constant love and taking pride in my achievements. I am so proud of both of you as well. **My big family** who is always there for good and bad times. And of course, **my small lovely family**. My wife who stood by me through this journey and who helped me overcome any obstacles while trying to reach this point. My little daughter and son, the fruits of my life and my source of inspiration.

ABSTRACT

The huge increments in data traffic and communication over the past few decades have pushed the conventional electronic communication systems to their physical limits in terms of data rate, bandwidth and capacity. The continuous shrinking of feature sizes, the increase in the microelectronic integrated circuits complexity, and the increasing demand for higher speeds and data rates have all stimulated seeking new technology to replace the currently present microelectronics industry rather than improving it. Photonics is one of the most likely candidates to answer this pursuit for its compatibility with the fiber optic industry, which has shown a great success in large-scale communication since around 50 years ago.

Silicon photonics, in particular, is very interesting for the scientific community for its compatibility with the foundries which are the bases for microelectronic industries around the globe. Advancements in silicon photonic would rather enable the integration of both electronic and optical system components on the same chip, which is a very important step in the transition towards all-optical on-chip systems. The huge interest in silicon photonics over the past two decades has brought forth a number of applications in various fields, such as biosensing, displays, on- and off-chip interconnection, artificial intelligence, internet of things, big data centres, and telecommunications.

In practice, there are many ways of realizing and fabricating on-chip silicon waveguides. Ion exchange process is one of the most commonly used techniques in fabricating glass waveguides as it offers ease of application, low cost, and low equipment requirements. Unfortunately, numerical constraints render the modelling of this process challenging due to the presence of computational instabilities at certain conditions. In the first part of this thesis, this issue is worked out by introducing a novel numerical model based on finite element method formulation. In the second part of the thesis, we concentrate on one of the promising applications of silicon photonics, which is the telecommunications.

Optical communication systems include many components such as, light sources, photodetectors, multiplexers, filters, resonators, optical interconnects, switches, couplers, splitters, and modulators. The optical modulator is considered the most essential component in an optical communication system as it converts the incoming electric digital

data into an optical data stream. Its acts as a binding link between both the optical and electronic domains on the chip. Therefore, electro-optical modulators have gained enormous attention during the past few years.

Weak electro-optical effects in intrinsic silicon have stimulated the search for novel materials to be responsible for the modulation of the light beam. Surface plasmon polaritons, which propagate at a metal-dielectric interface, allow the confinement of light in subwavelength dimensions. However, they introduce large losses to the system. Transparent conducting oxides, especially indium tin oxide (ITO), provide metal-like response when exposed to a gating voltage while maintaining lower losses than noble metals. In the second part of the thesis, we propose two novel electro-optical on-chip integrated modulators based on the utilization of ITO as the active material.

TABLE OF CONTENTS

LIST OF FIGURES IV

LIST OF TABLES VIII

LIST OF ACRONYMS/ABBERVIATIONS IX

LIST OF PUBLICATIONS XI

1 INTRODUCTION 1

1.1 History of Communication Forms 1
1.2 Moore's Law and Beyond 1
1.3 Optical Fibers and Silicon Photonics 3
1.4 Optical Modulation 3
1.5 Thesis Structure 4

2 BACKGROUND AND LITERATURE REVIEW 5

2.1 Optical Communication System Components 5
2.1.1 On-chip Lasers and Photodetectors 6
2.1.2 Multiplexers and Demultiplexers 8
2.1.3 Power Splitters / Combiners and Y-junctions 9
2.1.4 Optical Filters 10
2.1.5 Interconnects in PICs 11
2.1.6 Optical Modulators 13
2.2 Optical Modulation Schemes 14
2.2.1 Acousto-optic Modulation 15
2.2.2 Thermo-optic Modulation 15
2.2.3 Electro-optic Modulation 16
2.3 Optical Modulator Structures 17
2.3.1 Mach-Zehnder Interferometers 17
2.3.2 Multimode Interferometers 18
2.3.3 Electro-absorption Modulators 19
2.3.4 Subwavelength Grating Waveguides 20
2.3.5 Directional Couplers 22
2.3.6 Ring Resonators 23
2.4 Electro-optic Active Media 25
2.4.1 Semiconductors 25
2.4.2 Electro-optic Polymers 26
2.4.3 Graphene 27
2.4.4 Transparent Conducting Oxides 27
2.5 Optical Modulator Performance Parameters 30
2.5.1 Extinction Ratio 31
2.5.2 Insertion Loss 31
2.5.3 Modulation Speed 32
2.5.4 Energy Consumption 32

3 RECENT ADVANCES IN ITO-BASED ELECTRO-OPTICAL MODULATORS 33

3.1 Silicon Electro-optical Modualtors based on a Tunable Plasmonic Tri-core Directional Coupler [38] 33
3.1.1 Device Structure 33
3.1.2 Concept of Operation 34
3.1.3 Results 35
3.2 ITO-integrated Silicon Directional Coupler for Electr-optic Modulation Application [36] 36
3.2.1 Device Structure 36
3.2.2 Concept of Operation 37
3.2.3 Results 37
3.3 Hybrid ITO Tri-core Directional Coupler Optical Modulator based on the Epsilon-near-zero Characteristics of ITO [39] 38
3.3.1 Device Structure 38
3.3.2 Concept of Operation 40
3.3.3 Results 41
3.4 Hybrid Plasmonic ITO-based Electro-absorption Modulator [40] 41
3.4.1 Device Structure 41
3.4.2 Concept of Operation 43
3.4.3 Results 43
3.5 ITO On-chip Electro-optical Modulator based on Ring Resonator Structure [41] 44
3.5.1 Device Structure 44
3.5.2 Concept of Operation 45
3.5.3 Results 46

4 RING RESONATOR ELECTRO-OPTICAL ITO-BASED MODULATOR 47

4.1 Device Structure 47
4.2 Modal Analysis 48
4.2.1 Access Waveguide Width 48
4.2.2 Ring Cavity Width 49
4.2.3 Ring Cavity Modal Analysis 50
4.2.4 Separation Gap and Outer Radius 51
4.3 Results and Device Performance 52
4.4 Conclusion 55

5 DIRECTIONAL COUPLER ELECTRO-OPTICAL ITO-BASED MODULATOR 56

5.1 Design Procedure 56
5.1.1 Device Structure 56
5.1.2 Concept of Operation 58
5.2 Modal Analysis 59
5.3 Results and Discussion 59
5.4 Conclusion 64

6 LINEARIZED FEM SOLUTION OF THE ION-EXCHANGE NONLINEAR DIFFUSION MODEL 66

6.1 Introduction to the Problem 66
6.2 Ion Exchange Process Modeling 67
6.3 Linearized Finite Element Method Formulations 69
6.3.1 Forward-time Technique 70
6.3.2 Backward-time Technique 70
6.3.3 Crank Nicholson Technique 71
6.4 Results and Discussion 73

6.5 Conclusion 76

7 SILICON PHOTONICS FABRICATION AND CHARACTERIZATION EFFORTS 77

7.1 Mask Layout 77
7.2 Fabrication Sequence 79
7.3 Silicon-on-insulator 79
7.4 Conclusion 83

8 CONCLUSION AND FUTURE WORK 84

REFERENCES 86

LIST OF FIGURES

Fig. 1-1 The predicted number of electronic components fitted on a single chip [3]. 2
Fig. 2-1 The fundamental components of an integrated optical modulator. 5
Fig. 2-2 The basic components of a communication system [4]..6
Fig. 2-3 Composite photonic crystal structure with square and rectangular air holes lattice [9]. ..7
Fig. 2-4 (a) A 3D bird's eye view schematic and (b) a 2D cross-sectional cut of integrated on-chip laser, modulator and photodetector based on GaN deposited on silicon substrate [10]. 8
Fig. 2-5 A schematic of the proposed OADM in [13]. 9
Fig. 2-6 (a) A top view schematic of the device showing its two constituents: the adiabatic coupler section and the Y-junction section. Relationships between the excited input mode and the output supermodes for excitation from (b) WG_1 and (b) WG_2. 10
Fig. 2-7 The output spectrum of a bandpass optical filter used in MC-VLC systems to separate the colors of blue, green, yellow and red [19]. 11
Fig. 2-8 The evolution of optical communication systems and the usage of optical interconnects within the system through the past four decades [20]. 12
Fig. 2-9 A micrograph image of a four-port mode-selective silicon router for optical interconnection [22]. 13
Fig. 2-10 A simple illustration of optical modulator by IBM. 14
Fig. 2-11 The acousto-optic effect in an optical modulator [23]. 15
Fig. 2-12 The change in the refractive index of silicon with respect to the applied electric field at wavelengths of 1.07 μm and 1.09 μm [23]. 17
Fig. 2-13 A schematic of a simple Mach-Zehnder interferometer [4]. 18
Fig. 2-14 A schematic showing a simple concept of operation of a conventional MMI [24]......19
Fig. 2-15 A schematic view of an electro-absorption modulator [4]. 19
Fig. 2-16 (a) A 3D bird's eye view of a silicon-on-insulator grated structure. (b,left) The dispersion relation of the structure highlighting the three modes of operation: radiation, Bragg reflection, and subwavelength. (b,right) The field intensity profiles in the three regimes compared to a homogenous waveguide [25]..21
Fig. 2-17 A schematic of a simple directional coupler device [4]. 22
Fig. 2-18 The concept of operation of directional coupler devices [26]. 23
Fig. 2-19 A schematic of a simple ring resonator modulator structure [4]. 24
Fig. 2-20 The complex permittivity of the ITO (real part – solid line, imaginary part – dashed line) with respect to the applied gating voltage on the ITO. 30

Fig. 2-21 The variation in both the real (solid line) and the imaginary (dashed line) components of the refractive index of the ITO across a range of wavelengths from 1.5 μm to 1.6 μm when exposed to a potential of 2.35 V. 30
Fig. 3-1 Schematic view and the concept of operation of the proposed silicon electro-optic modulator. (a) A bird's eye view of the structure demonstrating the compatibility of the device with CMOS technologies. (b) A cross-sectional view of the device [38]. 34
Fig. 3-2 The E_y field component measured at a cross-section of the plasmonic Si-ITO-SiO_2-Si waveguide (a) at the "Off" state and (b) the "On" state [38]. 35
Fig. 3-3 The optical output power of the proposed electro-optical modulator at an operating wavelength of 1550 nm. The insets at the left show the field intensity distribution inside the device at both (above) "Off" state and (bottom) "On" state. 35
Fig. 3-4 (a) A 3D schematic of the proposed EOM device in [36]. (b) A 2D cross-sectional view of the device's structure. 36
Fig. 3-5 The field intensity distribution across the device at both (a) the "Off" and (b) the "On" states [36]. 38
Fig. 3-6 (a) A 3D bird's eye view of the electro-optical modulator proposed in [39]. (b) A 2D cross-sectional view of the device. 39
Fig. 3-7 The normalized field distributions across a cross-section cut of the device for (a) the even and (b) odd modes at the "Off" state, and (c) the even and (d) the odd modes at the "On" state [39]. 40
Fig. 3-8 The normalized field intensity along the device at both (solid blue) the "Off" and (dashed red) the "On" states [39]. 41
Fig. 3-9 Schematic of an electro-absorption modulator based on an ITO-integrated hybrid plasmonic waveguide as the modulation section: (a) a 2D cross-sectional view, and (b) a 3D bird's eye view [40]. 42
Fig. 3-10 The normalized field intensities monitored at the center of the SiO_2 slot layer along the device at both (a) the "Off" and (b) the "On" states [40]. 43
Fig. 3-11 A 3D schematic of the proposed device. An access silicon strip waveguide is coupled to a hybrid plasmonic ring resonator including an ITO layer. The inset at the right shows the cross-sectional view of the coupling region [41]. 44
Fig. 3-12 The transmission spectra through the device at different applied voltages [41]. 45
Fig. 4-1 a) A sideview schematic of the modulator device. The ring (on the right) contains an embedded ITO layer. b) A bird's eye 3D view of the modulator device with the positions of the contacts illustrated. 48
Fig. 4-2 Normalized propagation losses of the fundamental mode vs. the width of the access waveguide. 49

Fig. 4-3 The change in the effective refractive index of the fundamental mode inside the ring cavity vs. its width. The pale red dot indicates the intersection between the designed width and the required effective index....50
Fig. 4-4 Normalized field intensity at the ring cavity in both a) “On” state (V_g = 0 V), and b) “Off” state (V_g = 2.35 V)....51
Fig. 4-5 The transmission spectra through the ring resonator of an outer radius of 980 nm at different separation gaps ranging from 90 nm to 190 nm....52
Fig. 4-6 The output spectrum of a TM-excited mode at both the “On” and “Off” states at a ring’s outer radius of 980 nm....53
Fig. 4-7 The extinction ratios (left) and the insertion losses (right) to several devices with an outer radius ranging from 970 nm to 1 μm....53
Fig. 4-8 The extinction ratio of the device at different separation gaps ranging from 90 nm to 190 nm....54
Fig. 5-1 An electro-optic ITO-integrated modulator based on a directional coupler design. a) A bird’s eye view of the structure, b) A cross-sectional view taken at the section cut in (a)....57
Fig. 5-2 The variation in the effective refractive index of a TM-excited mode inside the coupler section waveguide against its width....58
Fig. 5-3 The normalized electric field distribution E_z across a vertical plane cut of the device at the “On” state: (a) even mode – (b) odd mode, and the “Off” state: (c) even mode – (d) odd mode....60
Fig. 5-4 The normalized field intensity E_z propagating through the device in both (a) the “On” state (V_g = 0 V) and (b) the “Off” state (V_g = 2.35 V)....61
Fig. 5-5 (a) The ER and (b) IL achieved by the proposed device over a wideband of operation for a separation gap of 100 nm and 50 nm....62
Fig. 5-6 The ER obtained from the ITO-integrated EOM for different values of gating potentials ranging from 0 V to 3 V....63
Fig. 5-7 The electrostatic contour lines across a cross-section of the coupler arm waveguide at a gating voltage of 2.35 V....63
Fig. 6-1 A simple flowchart of the solution process....72
Fig. 6-2 2D BT technique normalized concentration map at $\alpha = 0.9999$, diffusion coefficient $D = 0.0186\ \mu m^2/min$, constant diffusion time $T = 500\ min$ and constant step size $\Delta t = 0.1\ min$ and $\Delta x = \Delta y = 0.875\ \mu m$ 74
Fig. 6-3 2D CN technique normalized concentration map at $\alpha = 0.9999$, diffusion coefficient $D = 0.0186\ \mu m^2/min$, constant diffusion time $T = 500\ min$ and constant step size $\Delta t = 0.1\ min$ and $\Delta x = \Delta y = 0.875\ \mu m$ 74

Fig. 6-4 1D backward-time technique normalized concentration profile at $\alpha = 0.99$, normal diffusion time 1800 min, and total annealing time 700 min. The normalized concentrations after 300 min and 500 min of annealing are also illustrated. 75
Fig. 6-5 2D backward-time technique normalized concentration map at $\alpha = 0.99$. A total diffusion time of $500\ \mathrm{min}$ is followed by an annealing time of $200\ \mathrm{min}$, diffusion coefficient $D = 0.0186\ \mu\mathrm{m}^2/\mathrm{min}$ and constant step size $\Delta t = 0.1\ \mathrm{min}$ and $\Delta x = \Delta y = 0.875\ \mu\mathrm{m}$. 75
Fig. 7-1 A broad view of the different components included in the mask layout. The components are (from left to right): 90º bends, 180º bends, straight waveguides, and directional couplers. ..77
Fig. 7-2 Closer views of the different components of the mask. (a) 90º bends, (b) straight waveguides, (c) 180º bends, and (d) directional couplers...78
Fig. 7-3 A very close-up view of a directional coupler of the fabricated mask. Two 90º bends along the directional coupler are shown. 78
Fig. 7-4 A cross-sectional SEM image taken after the deposition of the SiO_2 and Si layers. The thickness of the SiO_2 layer is depicted in the image...80
Fig. 7-5 A cross-sectional SEM image taken after the deposition of the SiO_2 and Si layers. The thickness of the Si layer is depicted in the image...81
Fig. 7-6 Optical microscope images of some of the fabricated components: (a) directional coupler, (b) a close-up view of a directional coupler, and (c) input/output tapered waveguide. .83

LIST OF TABLES

Table I The effective refractive indices of the modes inside the ring cavity in both “On” and “Off” states........51
Table II Summary of the performance parameters of the proposed device (in bold) compared with other ITO-based modulators. 55
Table III Effective refractive indices of the even and odd modes at both the “On” and “Off” states........60
Table IV A comparison between the parameters achieved by our proposed design vs. other ITO-integrated modulators based on directional coupler devices........64
Table V A summary of the values of the global mass matrices $\boldsymbol{Meff}$ and load vectors $\boldsymbol{Feff}$ of the three mentioned techniques FT, BT and CN........72
Table VI The mean squared error of the three techniques (FT, BT and CN) compared to the numerical solution obtained by an FEM-based commercially-available tool – COMSOL Multiphysics........73
Table VII A summary of the recipe’s parameters for SiO_2 deposition 80
Table VIII A summary of the recipe’s parameters for Si deposition 81
Table IX A summary of the recipe’s parameters for Si etching at a rate of 100 nm/min........82

LIST OF ACRONYMS/ABBERVIATIONS

IoT	Internet of Things
PIC	Photonic integrated chip
WDM	Wavelength division multiplexing
OADM	Optical add-drop multiplexer
BG	Bragg grating
MDM	Mode division multiplexing
VLC	Visible light communication
FEM	Finite element method
MC-VLC	Multi-color visible light communication
EO	Electro-optical
EOM	Electro-optical modulator
MZI	Mach-Zehnder interferometer
MMI	Multimode interferometer
EA	Electro-absorption
EAM	Electro-absorption modulator
SWG	Subwavelength grating
SPP	Surface plasmon polariton
TCO	Transparent conducting oxide
ENZ	Epsilon-near-zero

ITO	Indium tin oxide
ER	Extinction ratio
IL	Insertion loss
CMOS	Complementary metal-oxide-semiconductor
MOS	Metal-oxide-semiconductor
FDTD	Finite difference time domain
PML	Perfect matched layer
IPA	Isopropyl alcohol
DI	Deionized
PE-CVD	Plasma-enhanced chemical vapor deposition
UV	Ultraviolet
DRIE	Deep reactive ion etching
ICP	Inductively coupled plasma
sccm	Standard cubic centimetre per minute
RPM	Rounds per minute

LIST OF PUBLICATIONS

Journal Papers

[A] **M. M. Badr**, M. M. Elgarf, and M. A. Swillam, “Silicon ring resonator electro-optical modulator utilizing epsilon-near-zero characteristics of indium tin oxide,” *Phys. Scr.*, Aug. 2019.

[B] **M. M. Badr**, M. Y. Abdelatty, and M. A. Swillam, “Ultra-fast Silicon Electro-optic Modulator based on ITO-integrated Directional Coupler,” *Phys. Scr.*, vol. 94, no. 6, Apr. 2019.

[C] M. Y. Abdelatty, **M. M. Badr**, and M. A. Swillam, “Compact Silicon Electro-Optical Modulator Using Hybrid ITO Tri-Coupled Waveguides,” *J. Light. Technol.*, vol. 36, no. 18, pp. 4198–4204, Sep. 2018.

[D] M. Y. Abdelatty, **M. M. Badr**, and M. A. Swillam “High-speed hybrid plasmonic electro-optical absorption modulator exploiting epsilon-near-zero effect in indium-tin-oxide,” *J. Nanophotonics*, vol. 12, no. 03, p. 1, Aug. 2018.

[E] **M. M. Badr**, and M. A. Swillam, “Linearized finite-element method solution of the ion-exchange nonlinear diffusion model,” *J. Nanophotonics*, vol. 11, no. 2, p. 026013, Jun. 2017.

Conference Papers

[F] A. E. Afifi, R. S. Elshamy, **M. M. Badr**, M. M. El-Rayany, and M. A. Swillam, "Novel silicon-on-insulator Michelson interferometer for optical filtering and wavelength demultiplexing applications." *Silicon Photonics XIV*. Vol. 10923. International Society for Optics and Photonics, 2019.

[G] A. F. Amer, **M. M. Badr**, and M. A. Swillam. "VO2/ITO Hybrid Plasmonic High Performance Electro-Optical Modulator." *Laser Science*. Optical Society of America, 2018.

[H] M. Y. Abdelatty, **M. M. Badr**, and M. A. Swillam. "Hybrid plasmonic electro-optical absorption modulator based on epsilon-near-zero characteristics of ITO." *Integrated Optics: Devices, Materials, and Technologies XXII*. Vol. 10535. International Society for Optics and Photonics, 2018.

[I] **M. M. Badr**, M. Y. Abdelatty, and M. A. Swillam. "All-silicon transparent conducting oxide-integrated electro-optical modulator." *Integrated Optics: Devices, Materials, and Technologies XXII*. Vol. 10535. International Society for Optics and Photonics, 2018.

[J] **M. M. Badr**, M. Y. Abdelatty, and Mohamed A. Swillam. "All-silicon directional coupler electro-optic modulator utilizing transparent conducting oxides." *Laser Science*. Optical Society of America, 2017.

[K] M. Y. Abdelatty, **M. M. Badr**, and M. A. Swillam. "Hybrid Plasmonic Electro-Optical Directional Coupler Based Modulator Based on Electrically Tuning the ITO's Properties." *Frontiers in Optics*. Optical Society of America, 2017.

[L] **M. M. Badr**, and M. A. Swillam. "Solving the nonlinear diffusion model of the ion exchange process using finite element method." *Physics and Simulation of Optoelectronic Devices XXV*. Vol. 10098. International Society for Optics and Photonics, 2017.

Chapter One

1 INTRODUCTION

1.1 HISTORY OF COMMUNICATION FORMS

Communication, in its simplest definition, is a process of sending and receiving information among people. It facilitates and enables the spread of knowledge and establishment of relationships. Since the dawn of history, mankind had to innovate new ways of communication rather than the face-to-face method. The earliest known form of distant communication is using the smoke signals. They were used by the ancients in warfare, to express danger, or to notify the tribe of sources of food and water. This method of sending long-distance messages was the only reliable way until late 18th century when the Chappe's telegraph system was introduced [1]. Later in early 19th century, Samuel Morse along other inventors developed a recording electric telegraph [2]. It uses electrical signals, which are usually conveyed via dedicated telecommunication lines, to send information over very long distances. Later in the 70s of the 19th century, Graham Bell has invented the telephone, the first instrument ever that could enable the transmission of human voice. They enabled people to speak with each other without the usage of any forms of coding over very long distances for the first time in history.

1.2 MOORE'S LAW AND BEYOND

In the 20th century, the field of electronics has emerged, and few decades later, integrated electronics began to be applied in most devices. In 1965, Gordon E. Moore has noticed and predicted that every two years, the number of electronic components on a single chip would double; later referred to as 'Moore's law' [3]. By that time, he has predicted that by the year 1975, the estimated number of components on a single chip would reach about 65,000. The findings of his early study are shown in Fig. 1-1. Even though, Moore's study was concerned with the CMOS technology, it has become evident that this law could be extended to other existing technologies.

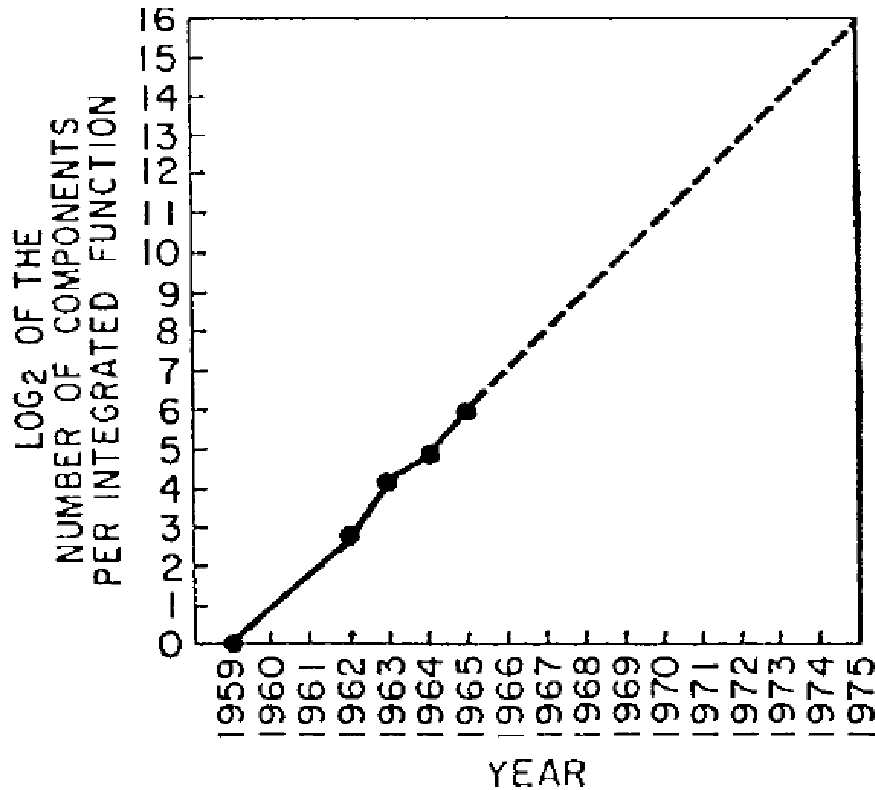

Fig. 1-1 The predicted number of electronic components fitted on a single chip [3].

Now, we are living in an era of information and data transfer. Every year, the data traffic in the carrier networks increases by nearly 60 % [4]. Moreover, the introduction to cloud-computing and internet of things (IoT) services would increase the data traffic of machine-to-machine communication by 90% [4]. According to a forecast report by Cisco [5], by the year 2021, around 20.6 zettabyte of information would constitute the global data traffic. These huge amounts of data along the increasing needs for higher data rates, bandwidths and network capacities have pushed the conventional CMOS technology to its physical limits. For example, reducing the transistor size to less than few nanometers is a very hideous task which is limited by the physical sizes of atoms and molecules, which are in range of few angstroms. Therefore, a pursuit for a new technology that will lead and continue the scaling trend, according to Moore's law, has gained a great attention since early 21st century. Silicon photonics is a preferable candidate as it provides factory-compatibility with the currently existing CMOS foundries across the globe. It provides larger bandwidths, larger system capacities and higher data rates increasing the speeds from hundreds of megabits per second (MBPS) to few gigabits per second (GBPS).

1.3 OPTICAL FIBERS AND SILICON PHOTONICS

Since the 1970s, optical fiber technology has proven a huge success in large-scale network communication. It contributes to the basis of intercontinental communication systems, such as the broadband internet and high definition televisions. Optical fibers offer low loss, low cost, robust, secure, interference-resistant, and fast mean of sending data for thousands of kilometres. With proper investments in this technology, the internet speeds have increased from 16 MBPS to 2 GBPS in 2016 [6]. Despite these huge advancements, in order to make the most out of this technology, the optical involvement in the systems has to reach the device level. This urge need has directed the attention of the scientific community towards the field of silicon photonics.

Silicon photonics enable the realization of nanophotonic devices along the electronic components on the same chip. The technology is CMOS-compatible, and it opens up a new vista towards higher performance levels and more on-chip applications and functionalities. Among the most important applications of silicon photonics is biosensing and telecommunications. One of the most important building blocks of on-chip integrated optical communication systems is the optical modulator. It converts the digital electric bits of information to an optical data stream.

1.4 OPTICAL MODULATION

Optical modulator is a vital component in optical communication systems. The user's message is coded and transformed to symbols used for the physical system. After that, the modulator's role is to carry this message over a continuous stream of light. The most commonly used modulation scheme in optical communication is the electro-optical modulation, where applying a voltage induces a change in the optical properties of the device. Weak electro-optic effects in silicon require the integration of other materials to provide the electro-optic response to the device, namely electro-optic active media.

One of the novel electro-optic active media is transparent conducting oxides (TCOs). They are invisible to light and provide high electric conductivity through an excess in free carriers. Applying gating potential induces a change in the concentration of free carriers inside the material, which increases the optical losses. This key feature allows the

modulation of light in response to the potential applied on the device. Indium tin oxide (ITO) is the most commonly utilized TCO in optical modulators.

1.5 THESIS STRUCTURE

This thesis mainly consists of two parts. The first part is considered with the fabrication and realization process of optical waveguides, while novel ITO-based electro-optic modulators are proposed in the second part.

- In this chapter, we give an introduction to silicon photonics and optical modulation, while highlighting the motivation of the work.

- In chapter 2, we provide the reader with a broad and detailed background about many concepts and theories. First, we discuss the different components of optical communication systems with the state-of-the-art work in the different tracks. After that, we present the different modulation schemes with more details on the electro-optical modulation in particular. Different modulator structures and geometries are then elaborated along the various types of electro-optical active media. Finally, the key performance parameters by which the modulator is evaluated are given.

- In chapter 3, we review some recent advances in ITO-based electro-optic modulators.

- For the first part of the thesis, in chapters 4 and 5, we propose two novel ITO-based electro-optical modulators. The first design is based on a ring resonator structure, while the other is based on a directional coupler.

- For the second part of the thesis, in chapter 6, we address a challenge in fabricating silicon waveguides. A finite element method formulation is introduced to solve instability issue when modeling ion-exchange waveguides. While in chapter 7, we introduce our efforts in different silicon photonics fabrication and characterization techniques.

- An overall conclusion of the thesis as well as the proposed future work is discussed in chapter 8.

Chapter Two

2 BACKGROUND AND LITERATURE REVIEW

In this chapter, a thorough review of the different components of the integrated optical communication systems, especially the modulator, is given. In general, integrated optical modulators are constituted from three fundamental categories as shown in Fig. 2-1: (1) the modulation scheme, (2) the physical structure of the device, and (3) the active medium which is responsible for modulating the signal in the device. Most of the schemes, structures and active media, which are used in constructing the optical modulators, are discussed and reviewed. Moreover, the key performance parameters are surveyed as well.

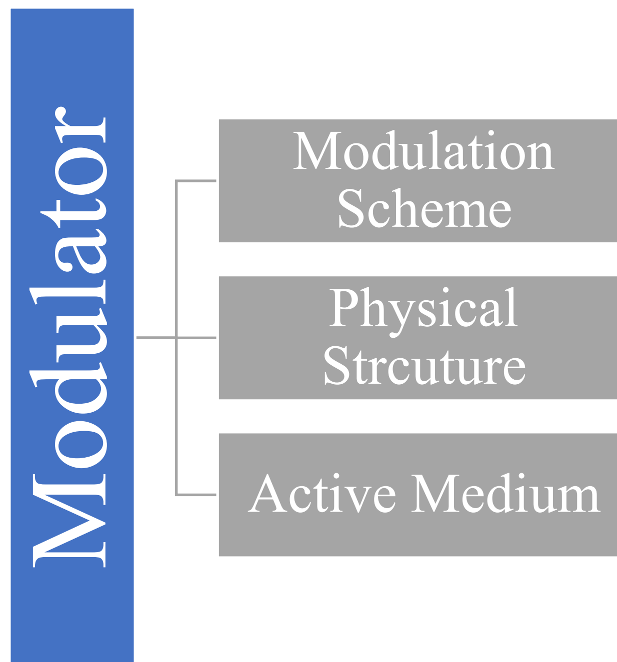

Fig. 2-1 The fundamental components of an integrated optical modulator.

2.1 OPTICAL COMMUNICATION SYSTEM COMPONENTS

At present, the systems of optical fiber communication can support long distance communication with low losses in the range of 1.3 μm – 1.6 μm at high data rates. Fiber optics is considered the cornerstone of intercontinental data transmission, that enables many services for the population of the globe; most importantly, the internet. The rapid evolution of the fiber optics field and its emphasis on our daily lives has stimulated the

need for integrated on-chip optical devices [7]. A general high-level hierarchy of communication system components are depicted in Fig. 2-2. The shown architecture can be broken into several components including: (1) lasers / photodetectors for transmitting and receiving the data, (2) multiplexers / demultiplexers for combining data from different sources into the channel, (3) power splitters / combiners and Y-junctions, (4) filters, (5) interconnects for connecting the different system modules, and (6) optical modulators, which are the core focus of this thesis.

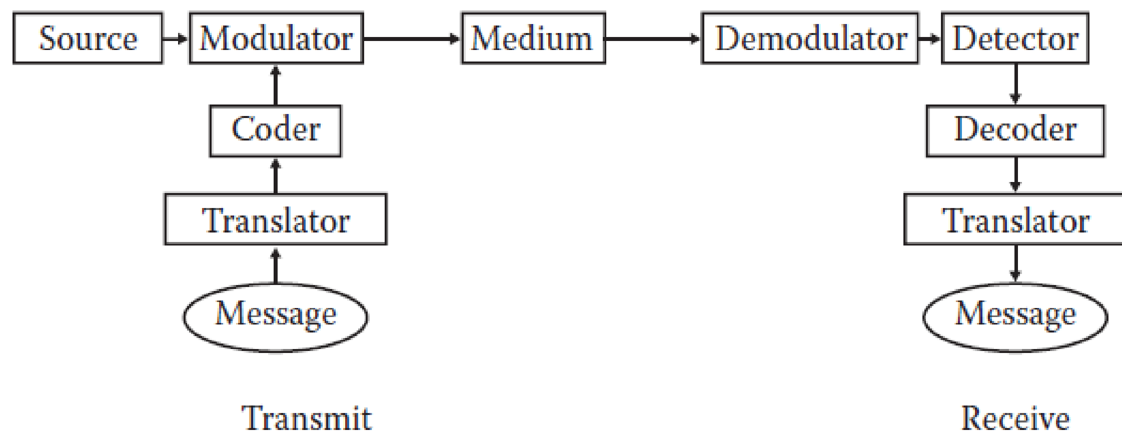

Fig. 2-2 The basic components of a communication system [4].

2.1.1 On-chip Lasers and Photodetectors

For any optical network, whether a photonic integrated chip (PIC) or an optic fiber system, a light source is an essential component. For silicon photonics, light sources have always been a critical issue due to the weak electroluminescence of silicon [8]. Therefore, there is a huge interest in the community towards the research and development of low-cost, fast-response, wideband and reliable lasers. Lasers can be incorporated in the system whether in an off-chip or on-chip manner. Off-chip lasers can be thought of as photon supply for the circuit. However, in most cases and applications, an on-chip laser is a better option that provides compatibility and mobility for the whole system.

Up until the last decade, controlling the direction of the beam generated from the on-chip lasers was performed by external mechanical methods. A novel concept to introduce beam steering of the laser output on-chip using photonic crystal structure is presented [9]. In Fig. 2-3, a schematic of a photonic crystal with air holes in both rectangular and square

structures is shown. The asymmetrical structure of the lattice leads to a shift in the output beam of the laser.

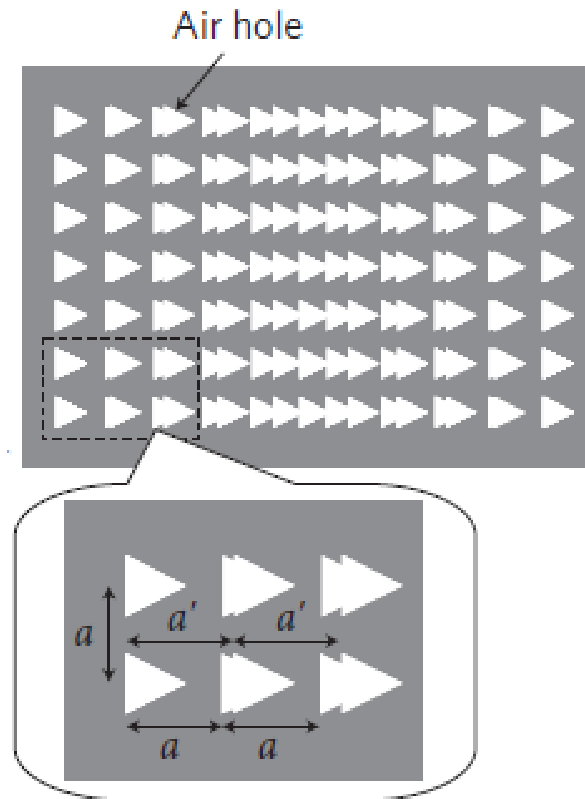

Fig. 2-3 Composite photonic crystal structure with square and rectangular air holes lattice [9].

As much important as the laser to the integrated optic systems, a reliable and fast photodetector is an essential component to the system as well. Consisted of P-N junctions, a photodetector acts like a light sensor that can convert the incident photons to electric signals. Recently, a GaN-based system integrating laser, modulator and photodetector on the same chip is reported [10]. The absorption of the modulator section is altered by changing the value of the applied potential. The photodetector can efficiently detect the output power of the modulator section and converting the power to an electric signal. A 3D bird's eye view as well as a 2D cross-sectional cut of the device is shown in Fig. 2-4. The whole integrated system is based on GaN technology grown on silicon. This high level of integration between different system components brings the scientific community one step closer towards fully integrated all-optical systems.

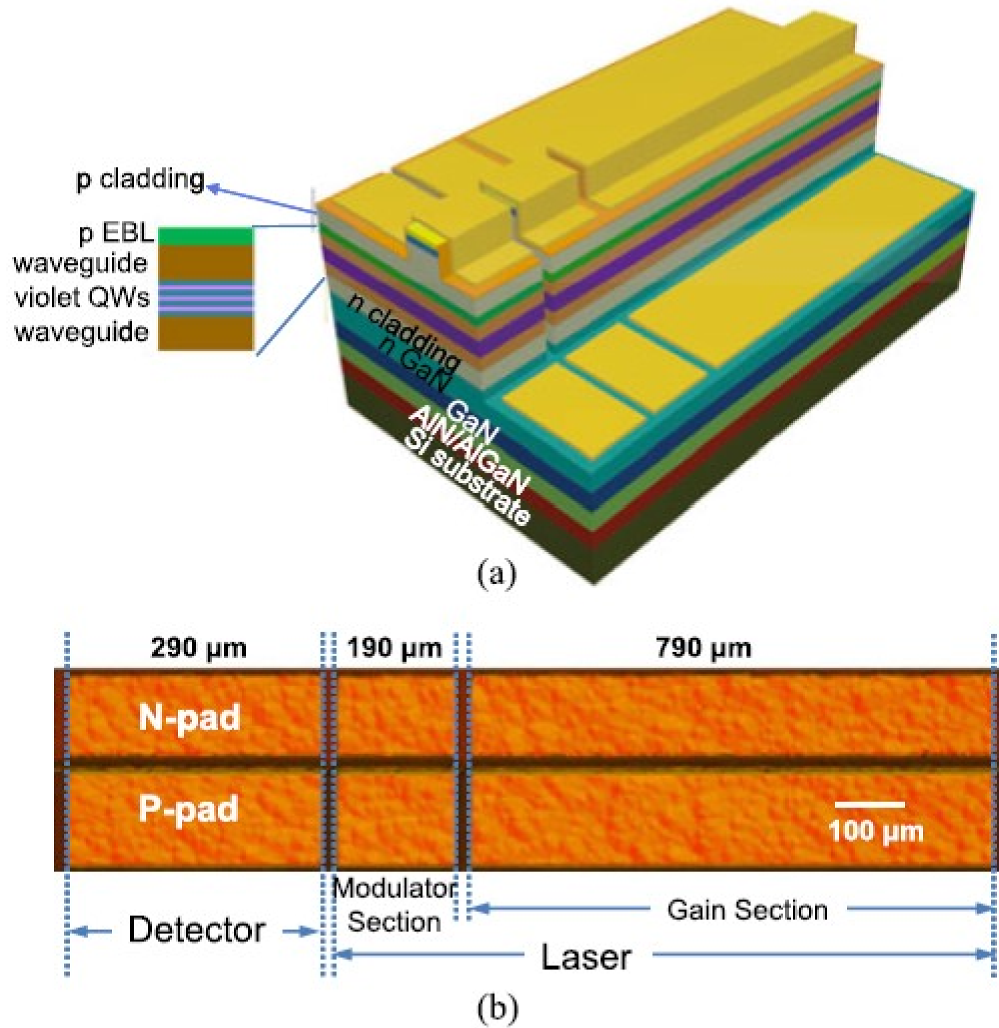

Fig. 2-4 (a) A 3D bird's eye view schematic and (b) a 2D cross-sectional cut of integrated on-chip laser, modulator and photodetector based on GaN deposited on silicon substrate [10].

2.1.2 Multiplexers and Demultiplexers

A key component of any optical communication system is the optical multiplexer. It enables the transmission of several channels of data through the same optical fiber without causing an interference between the sent messages. This comes of a great importance for the high data traffic imposed by the huge amount of information being transferred every day. Consequently, huge research has been directed towards providing different techniques to improve the capacity of the systems. Wavelength division multiplexing (WDM) is the most commonly used technique of multiplexing in optical multiplexers. It is considered a simple and a straightforward method to increase the capacity of the communication systems by sending several wavelengths on the same optical path [11],

[12]. A compact optical add-drop multiplexer (OADM) based on Bragg grating (BG) and mode selection on a silicon-on-insulator (SOI) platform is proposed recently [13]. A schematic of the OADM device is shown in Fig. 2-5.

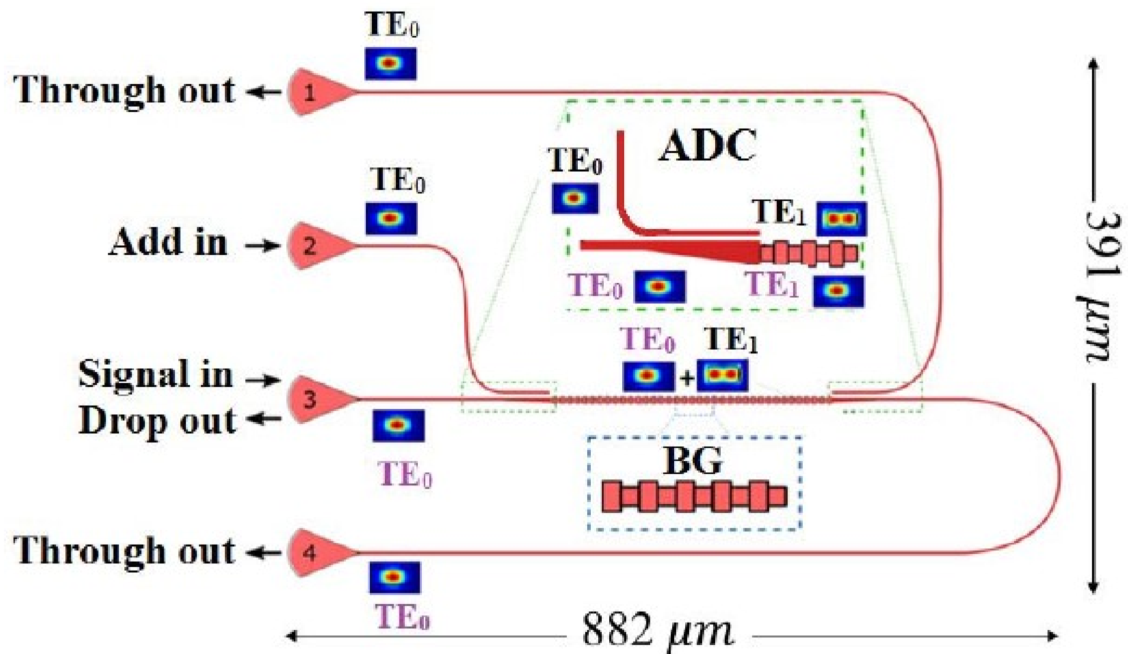

Fig. 2-5 A schematic of the proposed OADM in [13].

As shown in Fig. 2-5, the two multiplexed channels in the BG region are also demultiplexed at the other end. This is also a crucial feature in optical communication systems, where demultiplexing the channels into their original form is critical so that each message or piece of information is sent to its designated destination.

2.1.3 Power Splitters / Combiners and Y-junctions

Another important component of optical communication system is the power splitter / combiner. It is used to split power into different paths, routing and switching at system-level architecture. It acts as an essential tool for on-chip splitting of the power achieving low losses and low crosstalk interference operating over a broadband range of wavelengths. S-bends as well as Y-junctions are used in data routing and direction on the PIC. Power splitters can also be used to separate different modes in a multimode waveguide through mode division multiplexing (MDM) system. The MDM technique allows the usage of different guided modes inside the waveguide as separate signal carriers, which offers a new dimension in expanding the capacity of a single wavelength

channel [14], [15]. Recently, an ultra-broadband multimode 3dB optical power splitter is designed [16]. The device consists of two close waveguides based on SOI technology as shown in Fig. 2-6a. An adiabatic coupler section is followed by a symmetric Y-junction. In Fig. 2-6b and Fig. 2-6c, the outputs of the device as supermodes in case of four fundamental modes excited from WG_1 and WG_2, respectively.

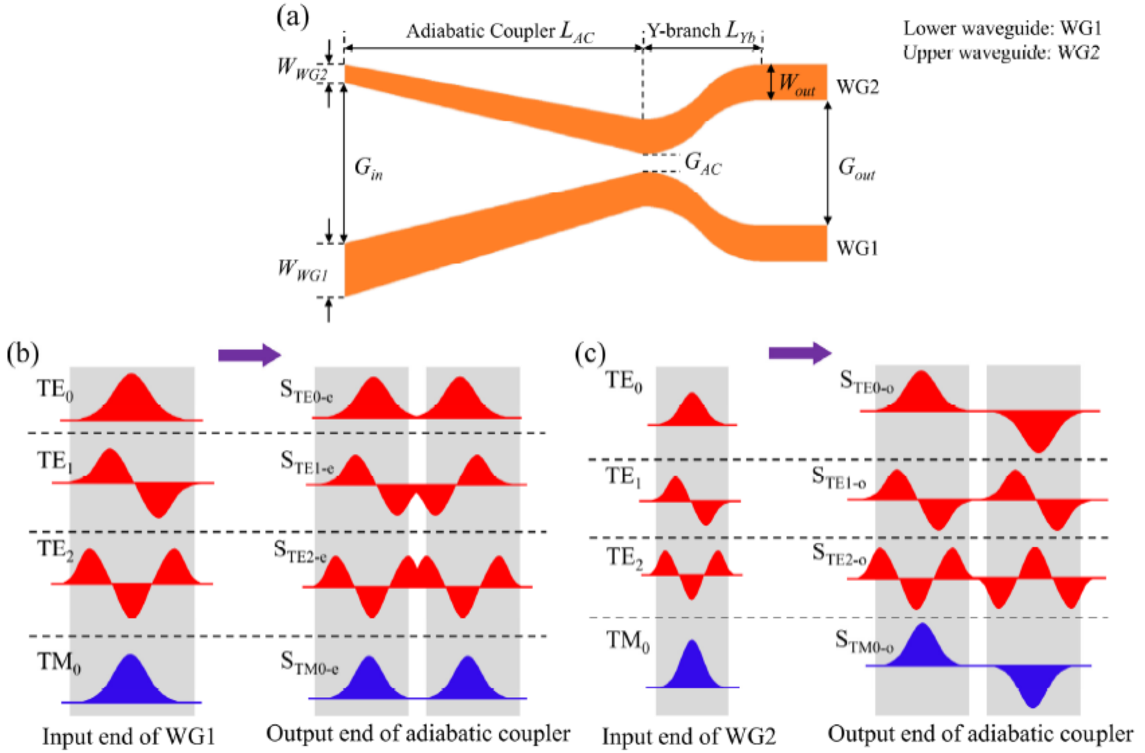

Fig. 2-6 (a) A top view schematic of the device showing its two constituents: the adiabatic coupler section and the Y-junction section. Relationships between the excited input mode and the output supermodes for excitation from (b) WG_1 and (b) WG_2.

2.1.4 Optical Filters

Towards the urge need for increasing and expanding the capacities of optical communication systems, different multiplexing techniques have been intensively studied as mentioned in the previous subsections. One way of demultiplexing the data, especially those depending on WDM scheme, is optical filtering. Optical filters can be used in separating several wavelength-based channels travelling through a single optical path. In recent years, for instance, visible light communication (VLC) has gained a tremendous interest from the scientific community as it offers both lighting and data communication simultaneously [17], [18]. In order to achieve high data rate transmission through a VLC system, WDM is used creating a new system of multi-color visible light communication

(MC-VLC). However, an optical bandpass filter is crucial for such systems to separate the different colors effectively and efficiently. Recently, several novel optical filter designs are proposed for MC-VLC systems [19]. The four colors of blue, green, yellow and blue are successfully separated with low leakage losses and minimal crosstalk among the different channels as shown in Fig. 2-7.

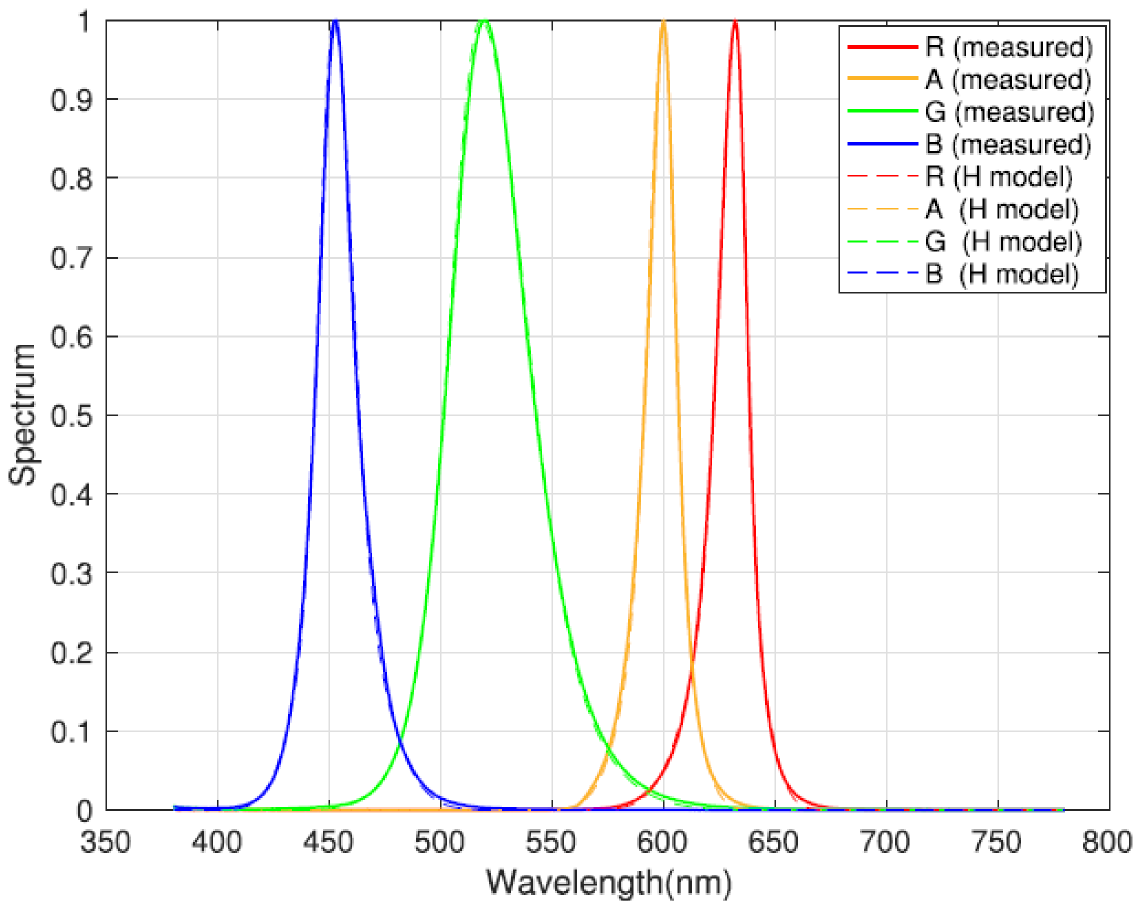

Fig. 2-7 The output spectrum of a bandpass optical filter used in MC-VLC systems to separate the colors of blue, green, yellow and red [19].

2.1.5 Interconnects in PICs

In order to keep up with the unprecedented exponentially growing rate of technology, new ways of interconnection between the different components, devices and modules on the chip must be found. The recent progress in data transfer has stimulated the urgent need for many technologies, such as accelerator chips, employing multiple cores on one chip, scaling data centres and high-performance computing systems. On-chip optical

interconnection has enabled a huge advancement in the mentioned tracks by providing a low loss, high bandwidth and a high data rate up to many Gbits/s from hundreds of Mbits/s [20], [21]. Consequently, a huge interest in using optical interconnection between the several core on-chip is developed in the recent years as illustrated in Fig. 2-8.

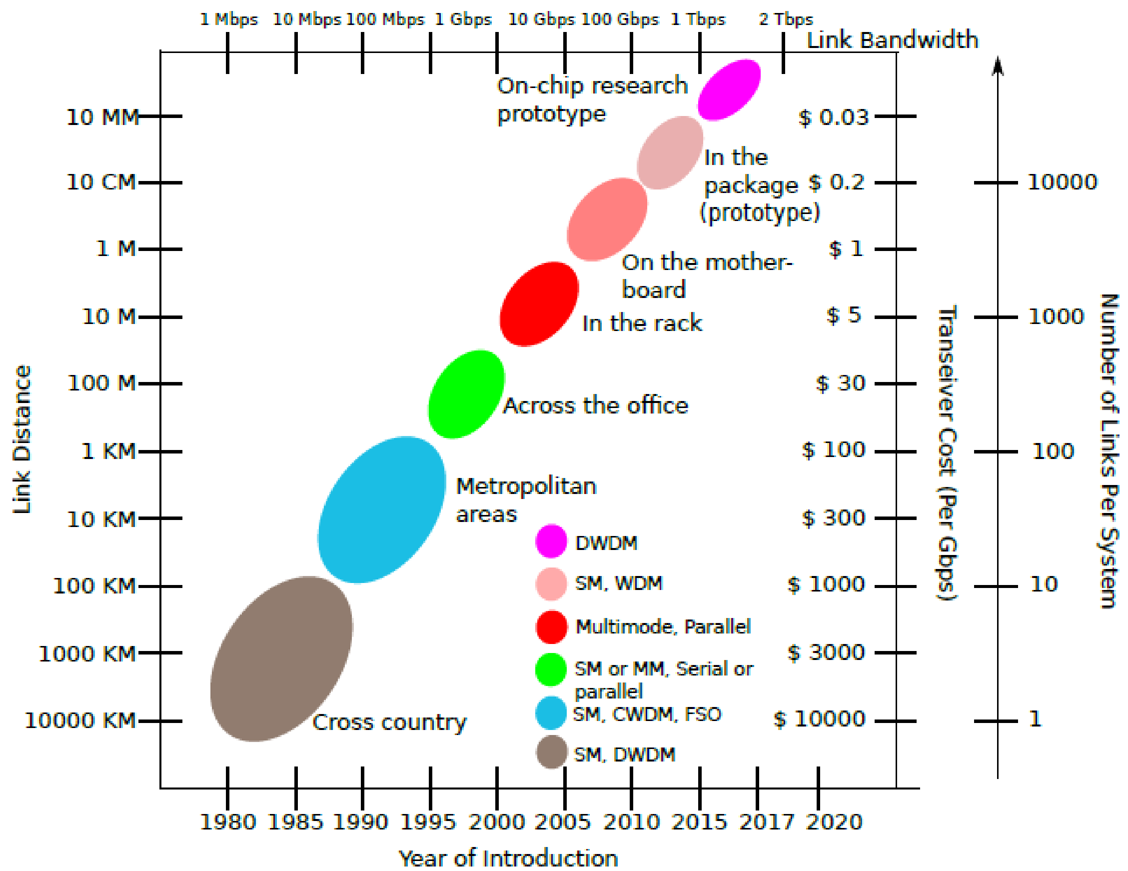

Fig. 2-8 The evolution of optical communication systems and the usage of optical interconnects within the system through the past four decades [20].

Recently, a silicon optical router based on four-port mode-selective technology has been proposed to be utilized as an optical interconnect [22]. A passive routing features ensure the optical connection establishment between on-chip modules without consuming power. Input signals can be routed from one port to another based on the mode of operation. A micrograph image of the device showing the four input/output ports is displayed in Fig. 2-9.

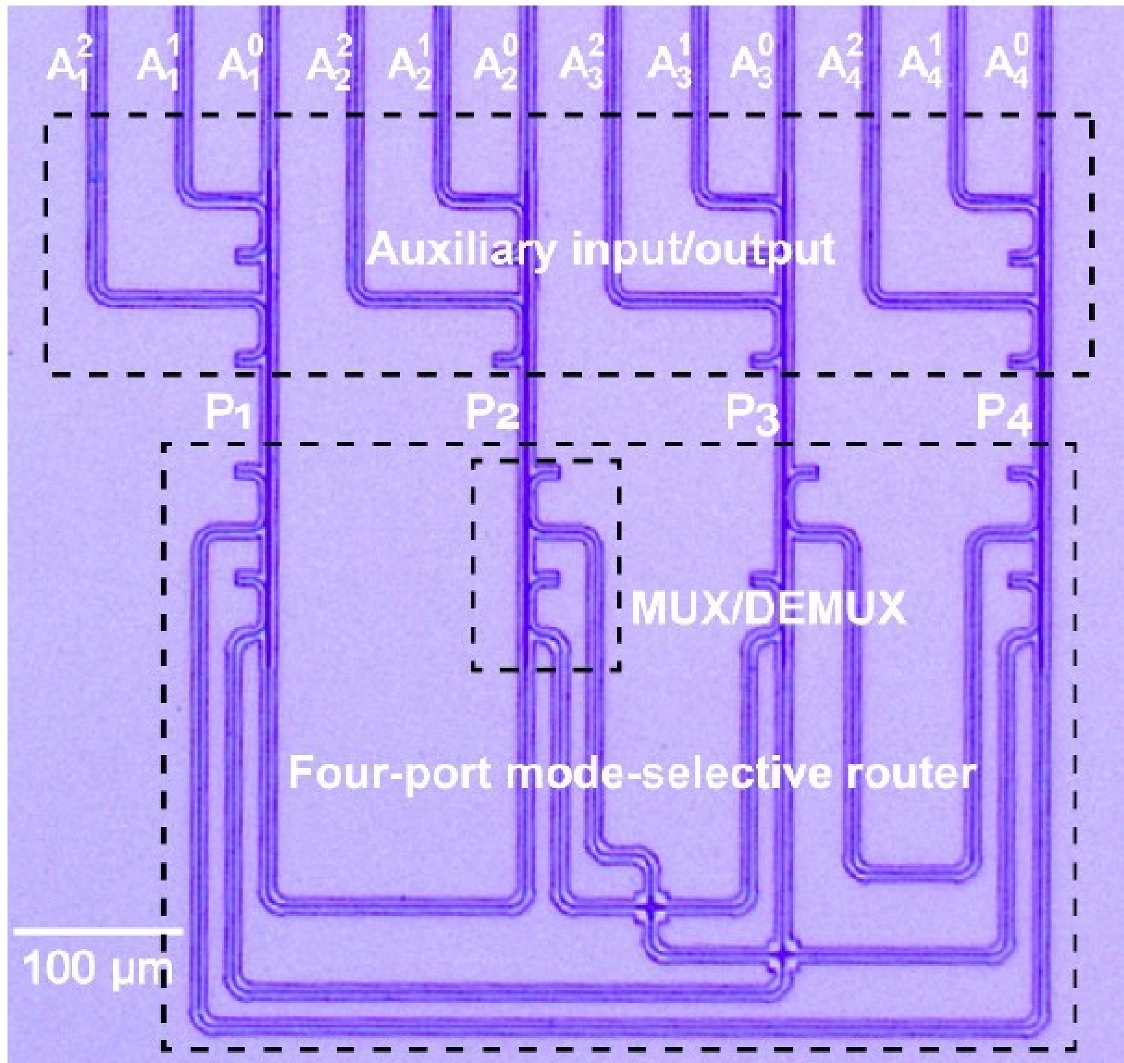

Fig. 2-9 A micrograph image of a four-port mode-selective silicon router for optical interconnection [22].

2.1.6 Optical Modulators

The increased demand for higher telecommunication network capacities and bandwidth has pushed the conventional micro-electronic systems to their limit. Optical communication systems are to replace the currently existent traditional electronic systems as they offer more security, larger bandwidth, higher data rates and lower power consumption. However, in order to be able to transmit digital electronic data across these systems, an optical modulator is fundamental in modulating the optical light according to the electric signal. As shown in Fig. 2-2, the modulator block has two inputs, a traditional digital electronic signal, encoded from the message intended to be transmitted, as well as a light source with continuous optical stream. The optical modulator is the most important

building block of optical communication systems as it acts as a linking bridge between both the electronic and optical domains. It converts the electronic digital signal into a modulated optical data stream as illustrated in Fig. 2-10. Due to its huge importance in realizing fully integrated on-chip optical communication systems, optical modulators are chosen as the core focus of this thesis. In the upcoming sections, the different optical modulation schemes, the different modulator structures, as well as several electro-optic active media are discussed and reviewed.

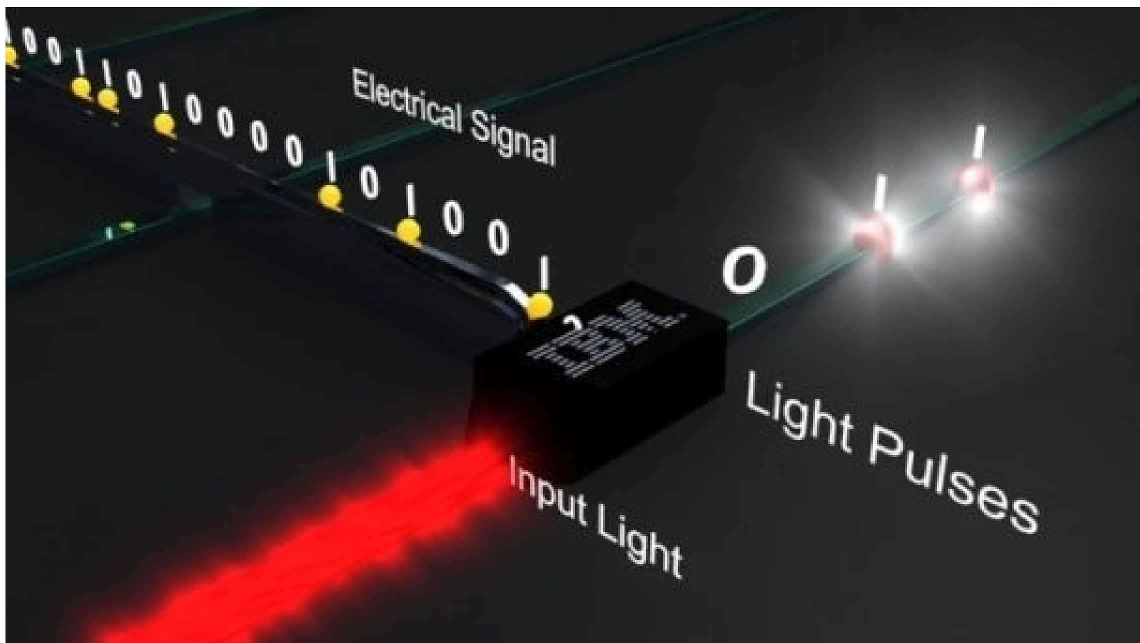

Fig. 2-10 A simple illustration of optical modulator by IBM.

2.2 OPTICAL MODULATION SCHEMES

The modulation of light inside the optical modulator can be achieved using different mechanisms depending on the material utilized. In this section, a brief review of different physical modulation schemes is given. Usually, modulation occurs when the optical properties of the active material change as a result of exposure to an external acoustic wave, rise in the temperature, or an electric field. Depending on the crystal structure of the material, it acts differently to the different external stimuli. In the following subsections, we will discuss the effects of acousto-optic modulation, thermo-optic modulation and electro-optic modulation.

2.2.1 Acousto-optic Modulation

The acousto-optic effect is defined as the change that occurs in the optical properties of the material in response to its subjection to a sound wave. As shown in Fig. 2-11, an acousto-optic crystal is a material whose refractive index is altered when an acoustic wave travels through it [23]. Sound waves act in solids in the same manner as they do in liquids and gases through relaxations and compressions in the space. In solids, these vibrations lead to variations in the positions of the molecules with respect to their original position. Consequently, the material becomes denser in the compression region, hence, a higher index of refraction. On the other hand, at the region of the material where the sound wave is relaxed, a lower refractive index is achieved due to the lesser density of the molecules.

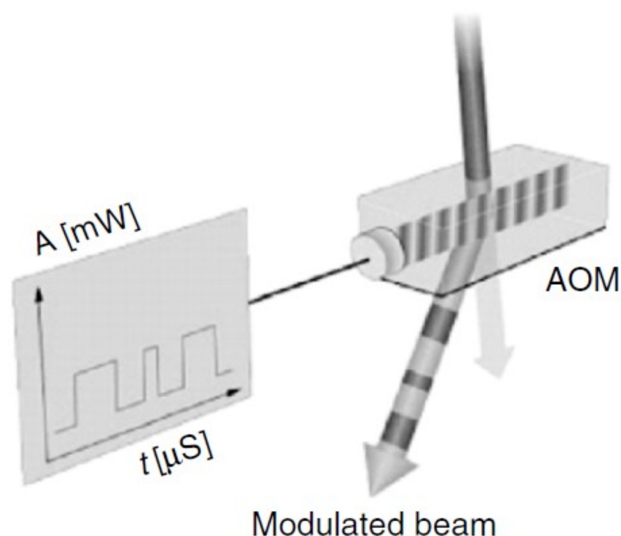

Fig. 2-11 The acousto-optic effect in an optical modulator [23].

2.2.2 Thermo-optic Modulation

For better understanding of the thermo-optic effect, we define the refractive index of the material as a complex number in the form $n + ik$, where n and k are the real and imaginary parts of the refractive index, respectively. The imaginary part of the refractive index is responsible for the optical losses inside the material, and it is directly related to the absorption coefficient α by the relation $k = \alpha\lambda/4\pi$.

Since the refractive index is not constant with respect to changes in the temperature, a thermo-optic effect occurs in several materials. The change in the refractive index is

originated from three distinct physical phenomena: (1) the expansion of the material's crystal with temperature. (2) the shrinkage of the bandgap induced by temperature increase. (3) the change in the distribution and generation rates of carriers inside the material with increasing the temperature. A thermo-optical coefficient is defined as the rate of change of the refractive index with respect to change in the temperature $\partial n/\partial T$. It is measured in K^{-1} units, and it ranges between 10^{-3} and 10^{-6} in silicon [23].

2.2.3 Electro-optic Modulation

Both the acousto-optic and thermo-optic effects are weak in silicon, which renders the realization of Si-based thermo-optic modulators or acousto-optic modulator hideous. Moreover, these types of modulators experience a huge setback in the compatibility with the well-established CMOS technologies. As the optical modulator's purpose in the optical communication system is to link between the electric and optical domains of operation, it is more appealing to exploit the electro-optic effects of the materials in realizing optical modulators. As a result, electro-optical modulators (EOMs) are the most commonly realized device in the optical modulation field serving the optical communication systems.

When subjected to external electric field, some materials experience a change in the refractive index accordingly. This phenomenon exists as the molecules of the material could experience a change in their positions, orientations, or shapes when exposed to a static or low-frequency electric fields. This change can occur in a linear, quadratic, or any higher-order manner. We are only interested in both the linear and quadratic effects, namely the Pockels and Kerr effects, respectively. Therefore, the refractive index of electro-optic materials is represented as follows in (2.1) [23].

$$n(E) = n - \frac{1}{2} r n^3 E - \frac{1}{2} \xi n^3 E^2 + \cdots \tag{2.1}$$

where n is the refractive index of the material when there is no external voltage is applied, r and ξ are the Pockels and Kerr coefficients, respectively. In silicon, the change in the refractive index induced by the applied electric field is shown in Fig. 2-12 [23].

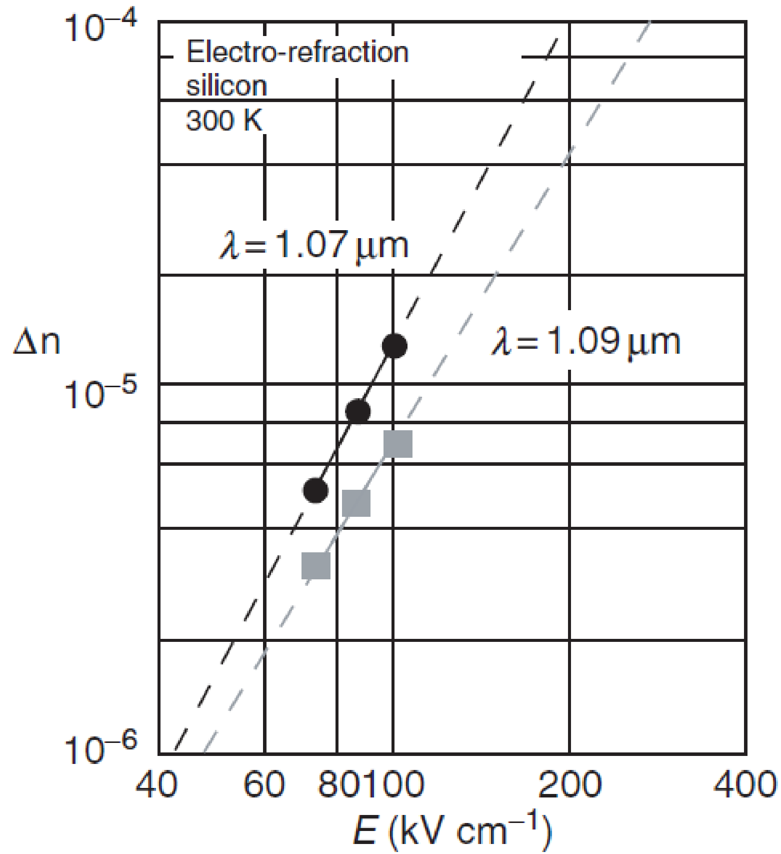

Fig. 2-12 The change in the refractive index of silicon with respect to the applied electric field at wavelengths of 1.07 µm and 1.09 µm [23].

2.3 OPTICAL MODULATOR STRUCTURES

For EOMs, there is a number of different device structures that can be employed to realize the modulation effect. In this section, the concept of operation of the Mach-Zehnder interferometers (MZIs), the multimode interferometers (MMIs), electro-absorption modulators (EAMs), subwavelength grating (SWG) waveguides, directional couplers, and ring resonators will be discussed and studied.

2.3.1 Mach-Zehnder Interferometers

The operation of MZIs depends on the fact of splitting the light power into two different optical paths and then recollecting them through Y-junctions as shown in Fig. 2-13. The refractive index of one of the arms is changed leading to a phase shift between the light in both arms at the combiner end. If a phase shift of 180° is accumulated between the two arms, no output power will survive to the other end of the MZI. For an on-off keying modulation, the following criterion has to be met according to the expression in (2.2).

$$\delta\phi = \delta\beta \cdot L$$

$$\delta\beta \cdot L = \frac{2\pi}{\lambda}\delta n_{eff} \cdot L = \pi \tag{2.2}$$

where $\delta\phi$ is the phase shift between the light in the two arms, $\delta\beta$ is the change in the propagation constants of the propagating modes inside the two arms, L is the length of the MZI arms, λ is the wavelength of operation, and δn_{eff} is the change in the effective refractive indices between the two arms.

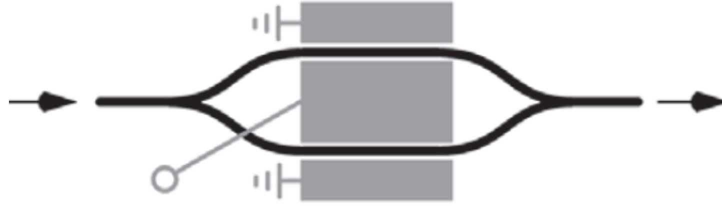

Fig. 2-13 A schematic of a simple Mach-Zehnder interferometer [4].

2.3.2 Multimode Interferometers

An MMI is basically a wide waveguide that can support a finite number of guided modes as depicted in Fig. 2-14. When the MMI is excited from the input port, the guided eigenmodes coexist in the multimode section. However, they propagate independently with each mode having its distinct velocity inside the interferometer. This phenomenon leads to an interference pattern that keeps on changing with the length of the MMI. According to the position of the output ports, the power could be split into a number of output facets. Even though, one can obtain a direct image of the input or a reversed image of it. In order to design the MMI, a specified length has to be set according to the formulae in (2.3).

$$L_\pi = \frac{4n_g W_e^{\ 2}}{3\lambda}$$

$$L = 3pL_\pi \tag{2.3}$$

where L_π is the beat length of the MMI, n_g is the slab effective index at the guiding region, W_e is the effective width of the MMI, λ is the operating wavelength, L is the designed length of the guiding region of the MMI device, and p is chosen as any even

number for a direct image, or any odd number for a reversed image. A simple illustration of the concept of operation of the MMI is shown in Fig. 2-14. As expressed in (2.2), a change in the effective refractive index inside the guiding region would affect the output pattern of the MMI. This feature can be exploited by applying electro-optic modulation to the guiding region.

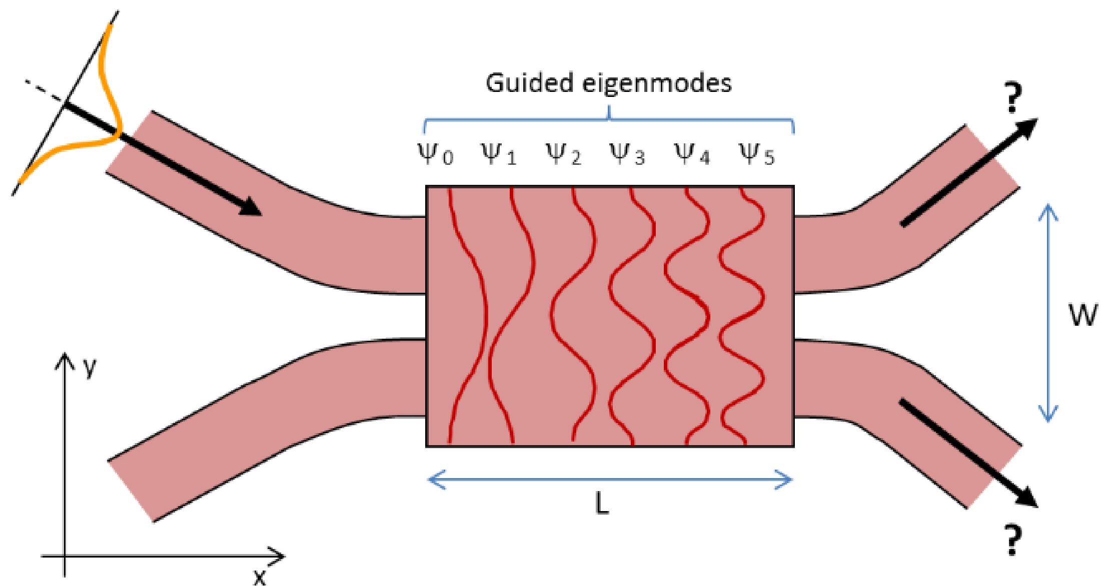

Fig. 2-14 A schematic showing a simple concept of operation of a conventional MMI [24].

2.3.3 Electro-absorption Modulators

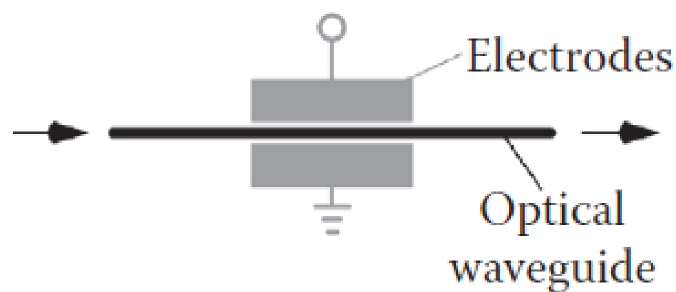

Fig. 2-15 A schematic view of an electro-absorption modulator [4].

The EAMs are simply working by directly modulating the intensity of the light while it propagates inside the waveguide. The concept of operation of this class of modulators depends on the alteration of the absorption coefficient of the electro-optic active medium due to an applied electric field. The structure of EAMs is rather simple, shown in Fig.

2-15, where electrodes around a single waveguide are used to apply an electric potential leading to a light modulation. One drawback of such modulators is that the absorption of light by the waveguide would introduce a considerable amount of heat in form of the dissipated energy.

2.3.4 Subwavelength Grating Waveguides

Depending on the ratio of a grating's periodicity with respect to the wavelength of the light subjected to it, a dielectric grating can act as a light diffractor or a homogenous material, in which the light propagates normally. Due to the huge recent advances in the nanolithography field, fabrication of photonic devices with subwavelength features is now enabled. If a dielectric periodic structure with a pitch much smaller than the wavelength of operation, the diffraction of the light due to the discontinuities of the structure will be suppressed. Instead, the light propagates normally within the structure as it treats the whole composite as a homogenous medium with an effective anisotropic refractive index tensor.

Consider the periodic structure in Fig. 2-16a, it consists of small separate rectangular Si waveguides with thickness a and a grating period of Λ deposited on a SiO_2 substrate. According to the ratio between Λ and the wavelength of operation λ, there exist three regimes of propagation in grated structures. Firstly, a radiation regime, where the wavelength of the incident light is considerably larger than the grating's period. At this case, the light experiences many diffractions and scatterings due to the discontinuities of the structure. Secondly, a Bragg reflection region, where the period of the grating is in the same order of the wavelength of light. In this scenario, the light is kept confined in the waveguide, but it reflects towards the input port. Finally, a subwavelength regime, where the wavelength is much greater than the periodicity of the grating. As mentioned above, in this case, the inhomogeneity of the structure is suppressed, and the light propagates normally through the structure in the same manner it would propagate in a homogenous waveguide with an effective refractive index tensor. These three modes of operation are illustrated in Fig. 2-16b.

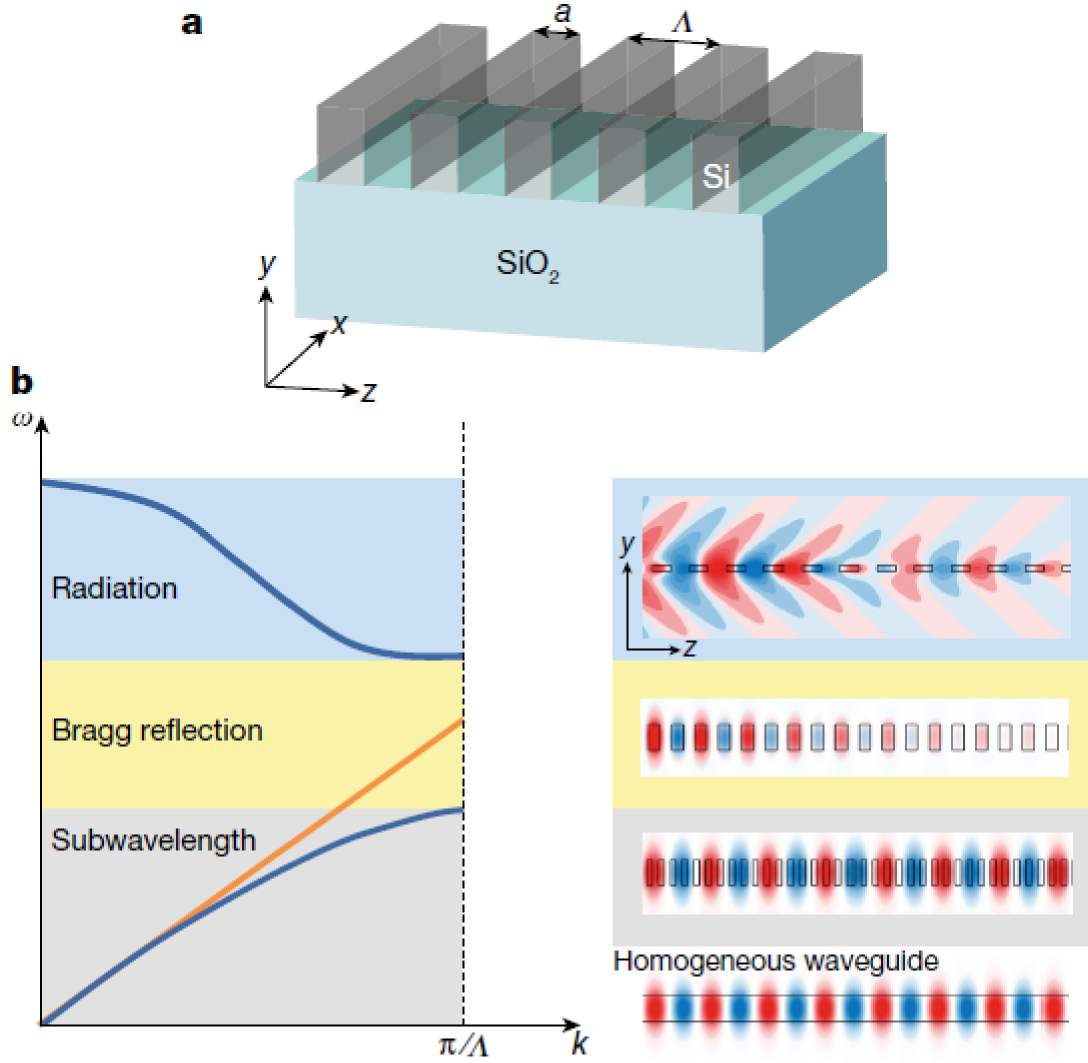

Fig. 2-16 (a) A 3D bird's eye view of a silicon-on-insulator grated structure. (b,left) The dispersion relation of the structure highlighting the three modes of operation: radiation, Bragg reflection, and subwavelength. (b,right) The field intensity profiles in the three regimes compared to a homogenous waveguide [25].

Let us consider the subwavelength grating (SWG) waveguide case, where the periodicity of the structure is much smaller than the incident wavelength. In this case, the light treats the whole composite as a homogenous material with effective anisotropic refractive index tensor as expressed in (2.4) [25].

$$n_{\parallel}^{2} = \frac{a}{\Lambda} n_1^{2} + \left(1 - \frac{a}{\Lambda}\right) n_2^{2}$$
$$n_{\perp}^{-2} = \frac{a}{\Lambda} n_1^{-2} + \left(1 - \frac{a}{\Lambda}\right) n_2^{-2} \tag{2.4}$$

where $n_{\parallel}$ is the effective refractive index of the composite when the polarization of the incident field is parallel to the periodic interfaces, $n_{\perp}$ is the effective refractive index when perpendicular to the interfaces, a is the width of the slab material, Λ is the grating period, n_1 and n_2 are the refractive indices of the slab material and the cladding material, respectively. As expected, the effective index of the composite structure gets affected by any change in the indices of the slab or cladding materials. An electro-optic effect in any of them could influence the propagation of light inside the SWG waveguide, that could lead to an alteration in the output profile of the field.

2.3.5 Directional Couplers

A simple directional coupler, like the one shown in Fig. 2-17, consists of two waveguides that come very close in some region. At this region, the modes inside the waveguides overlap causing the power to couple from one arm to the other alternatively.

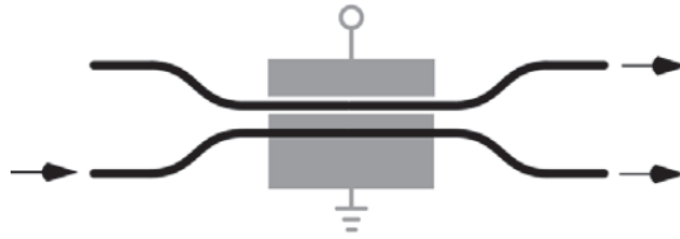

Fig. 2-17 A schematic of a simple directional coupler device [4].

If the modes at the centre of the device are studied, two fundamental propagation modes can be found, namely the 'even' and 'odd' modes. Each mode of these propagates independently with separate velocities and propagation constants β_{even} and β_{odd}. This variation leads to two scenarios, that are illustrated in Fig. 2-18. First, when the positive peak of the odd mode perfectly coincides with the peak of the even mode inside the first waveguide. At this case, all of the optical power is present at that waveguide. The other scenario is when the positive peak of the odd mode coincides with the peak of the even mode in the second waveguide. As expected, the power at this case couples to the second arm. The length required for the power to couple from one arm to the other is defined as the coupling length L_C, and it can be calculated according to the equation in (2.5).

$$L_C = \frac{\pi}{\beta_e - \beta_o} \tag{2.5}$$

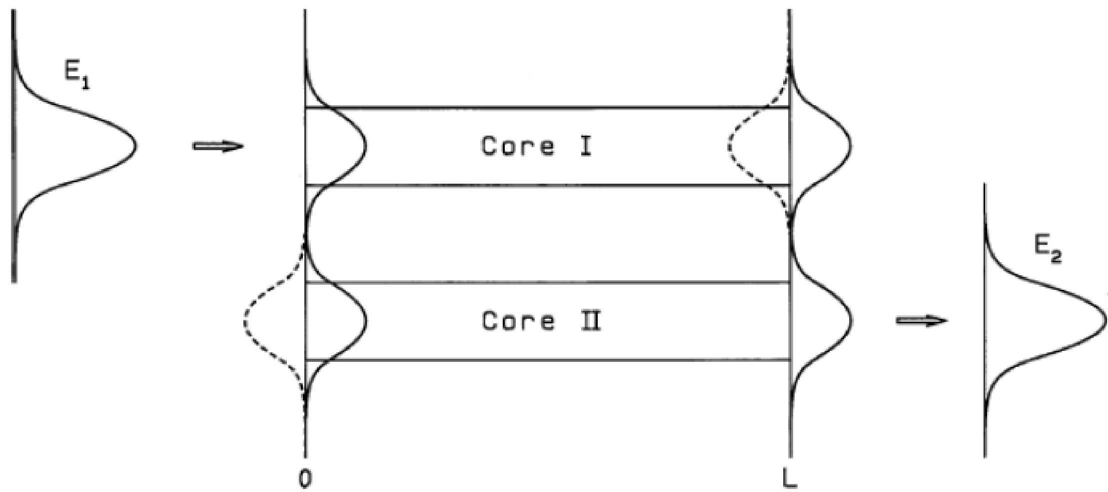

Fig. 2-18 The concept of operation of directional coupler devices [26].

2.3.6 Ring Resonators

Several optical modulators are based on filter designs. The idea is to operate near the edge of the filer's band, and when a change in the refractive index occurs that leads to a shift in the filter's response, an alteration in the transmission level can be noticed. One way of implementing this technique is through creating a resonant filter, or a notch filter. This class of filters allows the transmission of the whole spectrum of wavelengths except for the resonant wavelength. Applying external electric field would induce a change in the effective refractive index of the propagating mode leading to a shift in the resonant wavelength. If the shift is sufficient, a big alteration in the level of the transmitted power could be sensed.

One way of creating this resonance effect is by coupling a straight access waveguide or bus to a waveguide ring. The input/output access waveguide is excited with a continuous light source, while the whole ring waveguide, or a part of it, is modulated in response to an electro-optic material getting subjected to an electric field. A basic schematic illustrating the structure of ring resonators is shown in Fig. 2-19.

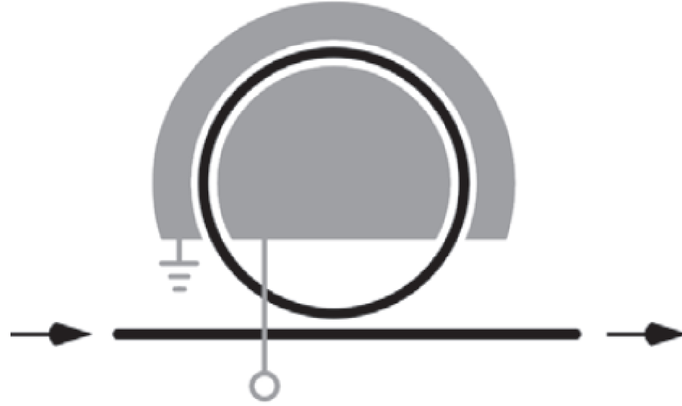

Fig. 2-19 A schematic of a simple ring resonator modulator structure [4].

In principle, there are three physical attributes of the ring modulator that can be utilized to achieve the modulation effect:

1. The effective refractive index of the mode inside the ring cavity.
2. The coupling coefficient between the access waveguide and the ring cavity.
3. The optical path losses inside the ring.

In order to meet the resonance condition in the ring resonator, the following criterion must be applied as in (2.6).

$$OPD = 2\pi R_o n_{eff} = m\lambda_{res} \tag{2.6}$$

where R_o is the outer radius of the ring cavity, n_{eff} is the effective refractive index of the mode propagating inside it, λ_{res} is the resonant wavelength, and m is the order of the ring resonator, that has to be an integer value. However, applying this condition solely does not grant a proper depth of the resonance peak. Additionally, one more condition, expressed in (2.7), has to be put in consideration to achieve critical coupling, where a minimum level of transmission occurs at the resonant wavelength.

$$T(\lambda_{res}) = \left(\frac{t-\alpha}{1-t\cdot\alpha}\right)^2 \tag{2.7}$$

where $T(\lambda_{res})$ is the transfer function of the transmission at the resonant wavelength, t is the transmission coefficient of the ring resonator, and α is the round-trip transmission

coefficient inside the ring cavity. It is noted that to achieve critical coupling, the transmission coefficient of the ring resonator has to match the round-trip losses inside the ring cavity.

2.4 ELECTRO-OPTIC ACTIVE MEDIA

One of the key aspects, that must be considered carefully when designing and EOM, is the electro-optic active material that is used to achieve the modulation effect. In fact, choosing a specific material for the design of the EOM would determine many other important factors, such as the possible electro-optic effects, the possible device structures, the preferred waveguide fabrication process, and many other characteristics.

The complex refractive index of any material can be expressed as follows

$$\bar{n} = n + i\kappa \tag{2.8}$$

where n is the real part of the refractive index, and it is responsible for the phase velocity of light inside the material. On the other hand, κ is the imaginary part of the complex refractive index, and it corresponds to the amount of attenuation the light experiences inside the crystal. In some materials, the real part n of the refractive index responds to the applied electric field greatly. In other materials, the change in κ is more dominant.

In this section, we will discuss and study some of the major types of active materials that are used in designing EOMs.

2.4.1 Semiconductors

Compared to conventional dielectric materials, semiconductors offer more interesting physical characteristics that can be applied in achieving modulation effects in optical devices. In addition to Pockels and Kerr EO effects in semiconductors, they also exhibit EA and carrier density effects. Moreover, they provide a great compatibility with current CMOS technologies. Only two classes of semiconductors are relevant to optical modulators industry: III-V semiconductors and silicon.

III-V Semiconductors

III-V semiconductors are compound materials made up from group III and group V elements. The most commonly used compounds in silicon photonics and optical communication systems are gallium arsenide GaAs and indium phosphide InP. This class of materials can be considered as the most important platform for optical communication applications. They can be utilized in designing lasers, photodetectors, transistors and modulators [4]. When it comes to optical modulators, the EA modulators are the most commonly realized class of modulators using III-V semiconductors. The Kerr effects in these materials are much stronger than the Pockels effect; however, they are accompanied by great losses and generate a high amount of heat.

Silicon

Silicon is the basis for most of the electronic industries worldwide. Most of the CMOS foundries across the globe are built on silicon technologies. Silicon-based optical devices would provide high integrability, reliability and repeatability to the industry. However, due to weak EO effects in intrinsic Si, this task is proven hideous. Other physical traits such as carrier density modulation is rather slow, and it is not practical in optical modulation.

Silicon, on the other hand, began to gain a lot of interest recently as the great advancements in lithography have led to Si/SiO_2 waveguides with small dimensions. This class of waveguides offers low propagation losses, low bend losses and high compatibility with optical fibers. Still, the absence of Pockels effect in silicon, and the presence of weak Kerr effects and EA effects lead to the difficulty of designing optical modulators that are depending solely on Si.

2.4.2 Electro-optic Polymers

Electro-optic polymers (EOPs) are dielectric materials that are invisible to light. They exhibit a high EO Pockels effect, higher than any other reported materials [4]. They have many advantages such as ease of application in the fabrication providing thin films. The change in the refractive index of an EOP is related to the voltage drop across it as follows in (2.8).

$$\Delta n_{EOP} = \frac{1}{2} n_{EOP}{}^{3} r_{33} \frac{V}{h} \tag{2.8}$$

where Δn_{EOP} is the induced change in the refractive index of the EOP, n_{EOP} is the refractive index of the polymer when there is no applied electric field, r_{33} is the electro-optic coefficient of the EOP, V is the applied potential drop across the EOP, and h is the thickness of the EOP layer. Very high electro-optic coefficients are reported; however, EOPs suffer from a weak heat resistivity as they can't withstand temperatures higher than the room temperature.

2.4.3 Graphene

Graphene is a two-dimensional material that has exotic optical and electrical properties. Since its introduction, graphene has gained a huge interest for its exotic light-matter interaction properties [27]. It serves the silicon photonics industry very well as it compensates the low light-matter interaction in intrinsic silicon. However, graphene-based modulator are limited in their performance due to the relatively low bandwidth and large power consumption [28]. Because of the monolayer nature of the graphene sheets, large areas of graphene are required in order to introduce proper device performance. The large sheets of graphene, in turn, increase the value of the RC constant of the device limiting the speed and increasing the power consumption of the device.

2.4.4 Transparent Conducting Oxides

Towards minimizing the dimensions of the EOMs in order to keep up with the technology advancements in lithography and fabrication techniques, scientific community has directed its attention to a new class of modes, which are surface plasmon polaritons (SPPs). This type of modes is the basis for plasmonic devices as they propagate along a metal-dielectric interface, leading to a high field confinement. This unprecedented confinement of light at subwavelength dimensions could overcome the diffraction limit [29]. However, since metals are present in such devices, large optical losses are introduced to the systems.

The need of the confinement introduced by plasmonics has stimulated the research towards finding novel materials that can provide the same plasmonic effects but at lower

losses. Transparent conducting oxides (TCOs) [30] are good candidates for this task. They offer optical invisibility as well as high electrical conductivity and an excess in free carriers. These characteristics provide TCOs interesting behaviour as they act like metals when exposed to electric potentials, and act as conventional dielectrics when no voltage is applied. By carefully engineering the voltage across the TCO, an epsilon-near-zero (ENZ) state can be achieved. Indium tin oxide (ITO) is the most commonly used TCO in optical communication system applications. These interesting characteristics and novelty could enable the design of EOMs with fast response, small footprint, high bandwidth, and CMOS-compatible traits. As a result, ITO-based EOMs are chosen as the core study of this thesis.

ITO Modelling

In this section, the model of ITO is studied intensively as it acts as the EO active medium in our proposed devices in this thesis. According to Drude's model, the complex permittivity of ITO can be expressed as follows [31]–[35].

$$\varepsilon = \varepsilon_\infty - \frac{\omega_p^{\ 2}}{\omega^2 + i\,\omega\gamma} \tag{2.9}$$

where ε_∞ is the high-frequency dielectric constant, ω_p is the plasma angular frequency, ω is the angular frequency, and γ is the collision frequency. The value of the plasma angular frequency changes with changing the concentration of the free carriers within the ITO film. This relationship is described in (2.10).

$$\omega_p^{\ 2} = \frac{Nq^2}{\varepsilon_0 m^*} \tag{2.10}$$

where N is the free carrier concentration inside the ITO layer, q is the fundamental charge of electron, ε_0 is the free space dielectric constant, and m^* is the electron effective mass in the ITO which is about 0.35 of the electron rest mass.

Applying different electric potentials on the ITO film leads to alterations in the concentration of free carriers within the material. The relationship between the applied gating voltage and the carriers' concentration is better understood when considering the

following scenario. Consider an ITO layer separated from a heavily doped silicon slab with an insulating dielectric. In most EOMs, the insulating material is chosen to be HfO_2 as it exhibits a high DC permittivity of about $\kappa_{HfO_2} = 25$ [34], [36]. This high dielectric constant value allows the accumulation of high concentration of free carriers at relatively small potential values. Now the gating voltage is related to the concentration of the free carriers through the expression (2.11).

$$N = N_0 + \frac{\varepsilon_0 \cdot \kappa_{HfO_2} \cdot V_g}{q \cdot t_{HfO_2} \cdot t_{acc}} \tag{2.11}$$

where N_0 is the carrier concentration in intrinsic ITO, κ_{HfO_2} is the DC permittivity of HfO_2, V_g is the applied gating voltage, t_{HfO_2} is the thickness of the HfO_2 layer, and t_{acc} is the thickness of the accumulation layer of the free carriers within the ITO layer. According to several previous designs [32], [37], t_{acc} is assumed to be around 7 nm. The standard dimensions of the ITO and HfO_2 layers in EOMs are chosen to be 10 nm and 5 nm, respectively.

In this thesis, the proposed ITO-based EOMs are designed to operate around the standard telecommunication wavelength of 1.55 µm. At this wavelength, the values of ω, ε_∞ and γ are 1.216×10^{15} s^{-1}, 3.9 and 1.8×10^{14} s^{-1}, respectively. According to equations (2.9), (2.10), and (2.11), a relationship between the applied gating voltage and the complex permittivity value of ITO is plotted in Fig. 2-20.

As shown in the above figure, increasing the value of the gating voltage leads to a decrease in the real component of the ITO's permittivity until it reaches almost zero at a potential of 2.35 V. Therefore, this value of gating voltage is chosen for the modulators proposed in this thesis. On the other hand, the imaginary part of the permittivity of ITO increases slightly with increasing the voltage.

At the chosen gating voltage of 2.35 V, the relationship between the real and imaginary components of the refractive index of ITO around the wavelength of 1550 nm is graphed in Fig. 2-21. Around the ENZ point, the phase of the ITO changes from a dielectric state to a metallic state, at which a surface plasmon could be excited. Therefore, it is crucial for our proposed devices to be designed to operate around this potential.

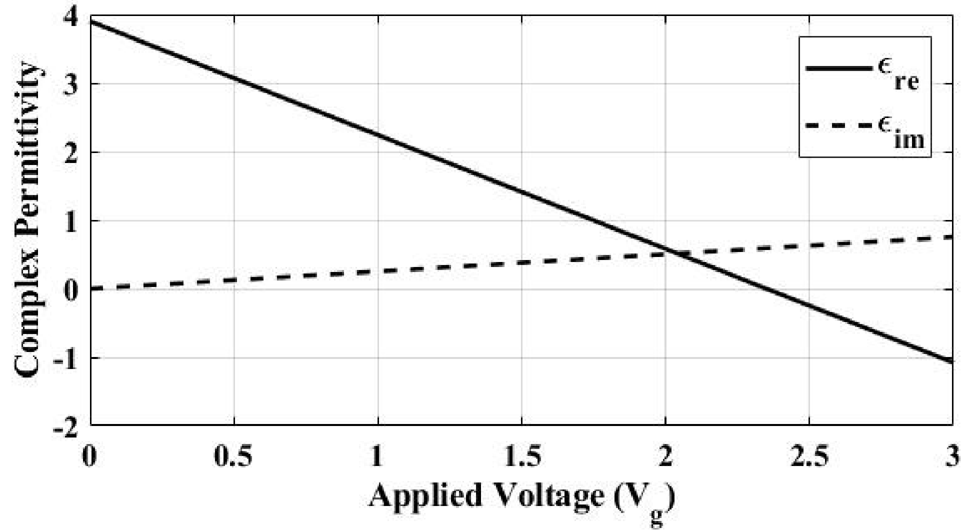

Fig. 2-20 The complex permittivity of the ITO (real part – solid line, imaginary part – dashed line) with respect to the applied gating voltage on the ITO.

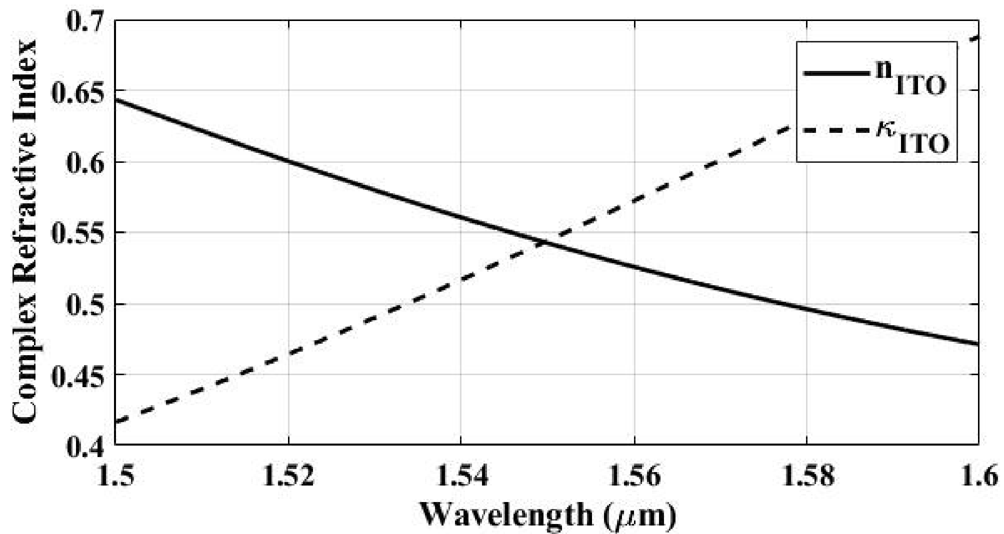

Fig. 2-21 The variation in both the real (solid line) and the imaginary (dashed line) components of the refractive index of the ITO across a range of wavelengths from 1.5 µm to 1.6 µm when exposed to a potential of 2.35 V.

2.5 OPTICAL MODULATOR PERFORMANCE PARAMETERS

In this section, we will discuss the key performance parameters of optical modulators. The factors, that we will mention here, are very important for designing and evaluating EOMs. They are used to compare between different designs and help designers in taking decisions when it comes to choosing the materials and the structure of the modulator.

2.5.1 Extinction Ratio

One of the most important performance parameters in EOMs is the extinction ratio (ER). ER is defined as the ratio between the levels of transmitted powers at both the "On" and "Off" states. It indicates the difference between the two levels at a dB scale. This value is important in deciding which photodetectors can operate with the proposed modulator device. Low ER requires very sensitive and selective photodetectors with low margin of error in order to be able to detect the '1' and '0' levels correctly. Therefore, the higher the ER the better the performance of the modulator. ER can be calculated as the following:

$$ER = 10\log\frac{P_{off}}{P_{on}} \tag{2.12}$$

where ER is the value of the ER calculated in dB, P_{off} and P_{on} are the levels of transmitted power at the "Off" and "On" states, respectively.

2.5.2 Insertion Loss

Another key factor regarding the evaluation of the modulator's performance is the insertion loss (IL). IL is defined as the amount of losses associated with the modulator device when it is in the "On" state with respect to the input power. In other word, IL represents how much losses the modulator introduces to the system. This value is very important for system-level design and architecture. It is best to minimize the IL of all the optical components on the PIC, and the modulator is no exception. High values of IL would require light sources with higher power in order to maintain an acceptable performance of the system. The estimation of IL comes as follows:

$$IL = 10\log\frac{P_{in}}{P_{on}} \tag{2.13}$$

where IL is the IL in dB, and P_{in} is the input power to the EOM.

2.5.3 Modulation Speed

The speed of the modulation process indicates how fast the modulator can respond to the incoming electronic digital signals and convert them successfully to an optical data stream. The speeds of EOMs have to at least keep up with their electronic counterparts, and even exceed their performance in order to benefit from the transition to optics to the highest extent. In ITO-based modulators, the carrier concentration process occurs almost instantaneously with negligible delay. As a result, the performance of the device is solely limited by its RC value. The maximum achievable modulation speed is estimated as follows:

$$f_{\max} = \frac{1}{2\pi RC} \tag{2.14}$$

where R is the internal resistance of the device calculated between the two electrodes on which the gating potential is applied, and C is the device's capacitance calculated across the same two terminals.

2.5.4 Energy Consumption

The energy that the modulator consumes for every bit of information it processes is a vital aspect in high-level design. It estimates the amount of energy the modulator consumes for every bit of digital data it sends. This value is related to the device's capacitance as well as the driving voltage through the expression (2.15) as follows:

$$E_{avg} = \frac{1}{2} C V^{2} \tag{2.15}$$

where E_{avg} is the average consumed energy of the modulator per bit, C is the capacitance of the device, and V is the applied voltage on the modulator.

C h a p t e r   T h r e e

3 RECENT ADVANCES IN ITO-BASED ELECTRO-OPTICAL MODULATORS

In this chapter, we review a number of recently proposed electro-optic modulators that utilize the epsilon-near-zero characteristics of ITO. The reviewed designs here depend on different structures, such as directional coupler, electro absorption modulator, and ring resonator.

3.1 SILICON ELECTRO-OPTICAL MODUALTORS BASED ON A TUNABLE PLASMONIC TRI-CORE DIRECTIONAL COUPLER [38]

3.1.1 Device Structure

The proposed device in this section is considered a three-core directional coupler with the centre waveguide is a MOS-type hybrid Si-ITO-SiO_2-Si structure. The light is modulated at the output waveguide by electrically tuning the voltage drop across the ITO layer leading to an alteration in the concentration of carriers within. The output waveguide is vertically offset as shown in Fig. 3-1. The modulator consists of two Si waveguides with widths of 450 nm and thicknesses of 250 nm. The input waveguide (bar port) is deposited directly on the buried oxide layer. On the other hand, the cross port is vertically offset by a value h_{offset} . The middle hybrid waveguide has a width of $w_p = 191$ nm and consists of a bottom 250 nm thick Si waveguide, topped by layers of ITO and SiO_2 with thicknesses of $t_m = 10$ nm and $t_d = 10$ nm, respectively. Another 250 nm thick Si slab is deposited on top of the SiO_2 layer. The centre waveguide is separated from the bar and cross ports with a gap $g = 200$ nm from both sides. The signal electrode is positioned on the top Si layer of the plasmonic waveguide, while the ground electrode is placed on a thin layer of Si that is formed by the means of selective etching to the right of the bottom Si slab in the plasmonic waveguide. The ground electrode is shown in Fig. 3-1 as golden rectangle. This thin layer section is long enough in order to guarantee optical isolation of the

propagating mode inside the plasmonic waveguide. In other words, we can neglect the effect of the ground electrode on the optical profile of the device.

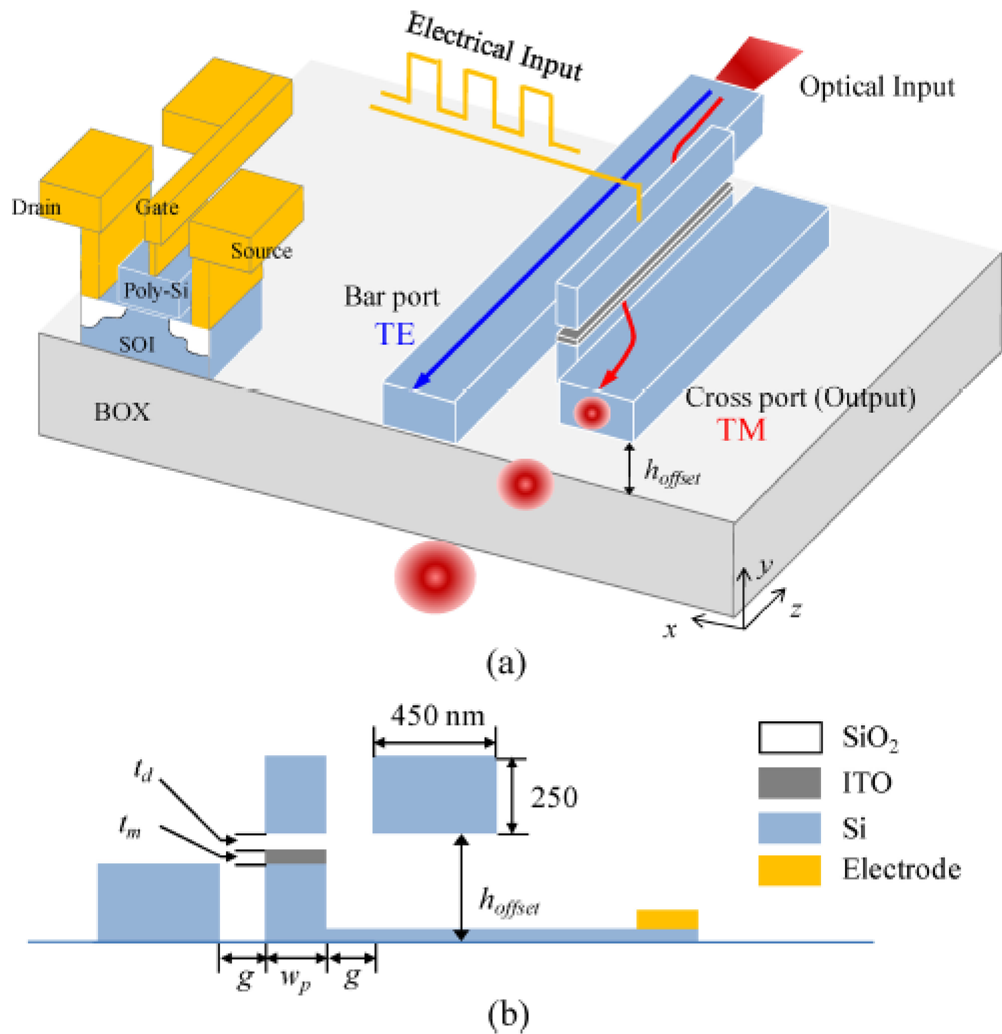

Fig. 3-1 Schematic view and the concept of operation of the proposed silicon electro-optic modulator. (a) A bird's eye view of the structure demonstrating the compatibility of the device with CMOS technologies. (b) A cross-sectional view of the device [38].

3.1.2 Concept of Operation

The input light is excited at the input waveguide and propagates along it. After that, it couples to the intermediate plasmonic waveguide, and after a coupling length, it couples out from it into the cross port. Designing the dimensions of the plasmonic waveguide for its length is equal to the coupling length of the directional coupler grants a maximum transmitted power through the output facet. At the "Off" state, no gating potential is applied on the ITO; therefore, the previously mentioned scenario occurs, and maximum power is measured at the output port. On the other hand, at the "On" state, an electric

potential of 2.0 V is applied on the intermediate waveguide leading to an adjustment of the concentration of free carriers inside the ITO film. This high concentration of carriers stimulates the formation of SPP mode at the ITO/SiO_2 interface, as shown in Fig. 3-2, which are characterized by high optical losses. This situation leads to an attenuated measured level of power at the cross port.

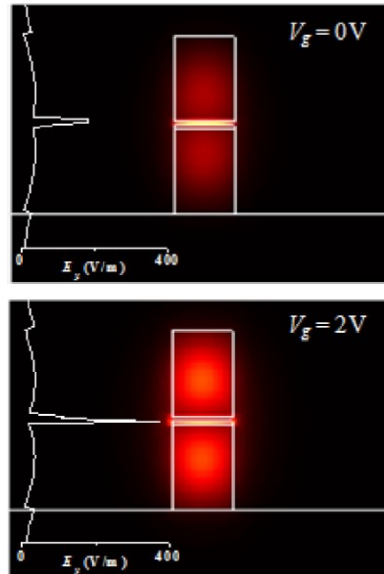

Fig. 3-2 The E_y field component measured at a cross-section of the plasmonic Si-ITO-SiO_2-Si waveguide (a) at the "Off" state and (b) the "On" state [38].

3.1.3 Results

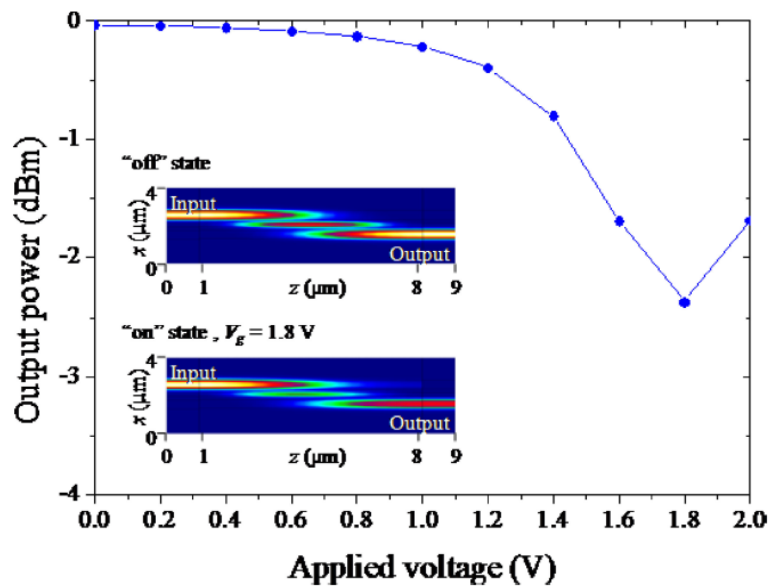

Fig. 3-3 The optical output power of the proposed electro-optical modulator at an operating wavelength of 1550 nm. The insets at the left show the field intensity distribution inside the device at both (above) "Off" state and (bottom) "On" state.

As graphed in Fig. 3-3, the output power measured at the cross-port's terminal varies against the applied voltage on the plasmonic waveguide. At no applied voltage, the "Off" state, around 99.2 % of the input power could be measured at the output facet. This yields an IL of only 0.036 dB. At a gating potential of 1.8 V, only around 57.9 % of the input power could be measured. Therefore, an ER of 2.3 dB is achieved. This performance of the device is studied at the standard telecommunication wavelength of 1.55 μm. The capacitance of the device is found to be around $C = 27.3\ \text{fF}$, which permits a maximum modulation speed of $f_{\max} = 116\ \text{GHz}$, assuming an internal impedance of $R = 50\ \Omega$. The average energy consumption per bit is around $E_{avg} = 78.8\ \text{fJ/bit}$.

3.2 ITO-INTEGRATED SILICON DIRECTIONAL COUPLER FOR ELECTR-OPTIC MODULATION APPLICATION [36]

3.2.1 Device Structure

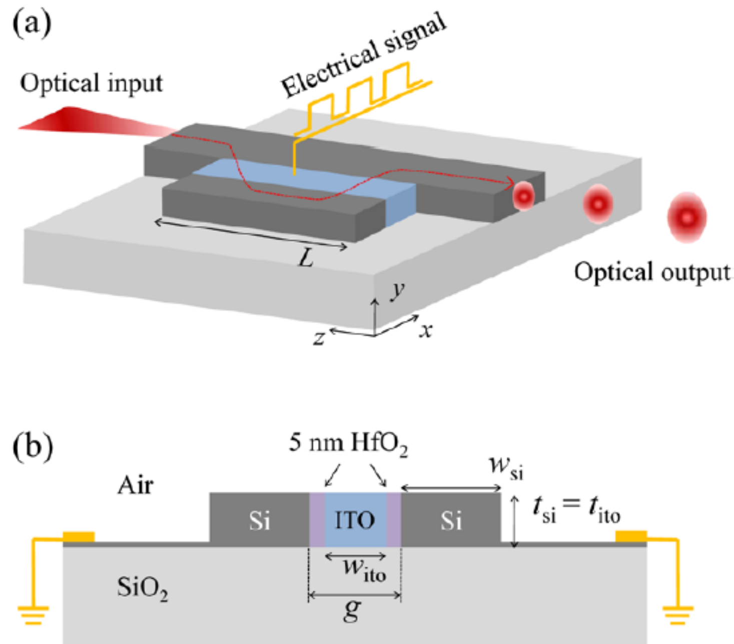

Fig. 3-4 (a) A 3D schematic of the proposed EOM device in [36]. (b) A 2D cross-sectional view of the device's structure.

In this section, another ITO-based EOM that depends on a directional coupler structure is discussed. In this device, an ITO block is placed in between two Si waveguides that constitute the directional coupler. The ITO block is separated from the Si slabs by thin 5 nm HfO_2 films as depicted in Fig. 3-4. The two silicon waveguides have dimensions of

width $w_{Si} = 300$ nm and thickness $t_{Si} = 250$ nm. They are separated from each other by a gap of $g = 200$ nm, which is filled by an ITO block with width $w_{ITO} = 190$ nm and two thin HfO_2 layers of thickness $w_{HfO_2} = 5$ nm. The signal is directly applied to the ITO block in the centre, while two ground electrodes are deposited on thin film extension of both silicon waveguides, as shown in Fig. 3-4b. A safe separation between the electrodes and the optical waveguides ensures optical isolation of the propagating modes inside the bar and cross ports.

3.2.2 Concept of Operation

The principle of operation in this photonic device is based on the coupling theory of two parallel waveguides. If the overlap length between the two Si waveguides is sufficiently enough, most of the light power couples from one arm to the other whilst passing through the ITO block in the centre. At the "Off" state, no gating voltage is applied on the ITO block. At this case, the ITO acts as a conventional dielectric material that is invisible to the light. Therefore, the coupling efficiency of the device is not affected, and maximum achievable power is measured at the output facet. On the other hand, applying an electric voltage onto the centre block of ITO increases the concentration rate of free carriers at the ITO/HfO_2 interfaces at both sides. This excess of carriers greatly affects the coupling coefficient between the two silicon waveguides. As a result, the value of the coupling length is changed which leads to a decrease in the amplitude of power received at the output end.

3.2.3 Results

Input light is excited at the facet of the input silicon port, then it couples to and back from the short silicon waveguide. At the "Off" state, when there is no applied voltage on the ITO, the coupling length of the device is unchanged, and maximum deliverable power is measured at the output end. Around 79.8 % of the input power could be measured at the output at this state yielding an IL of about 0.98 dB at a wavelength of 1.55 μm. Applying a gating potential of 2.0 V would accumulate a large concentration of free carriers at the ITO/HfO_2 interfaces. This, in return, affects the coupling length of the directional coupler leading ultimately to a decrease in the amplitude of the measured power at the output. Only around 41.9 % of the power could be measured at this state. These results achieve

an ER of about 2.8 dB. The field intensity profiles across the device in both the "Off" and "On" states are shown below in Fig. 3-5.

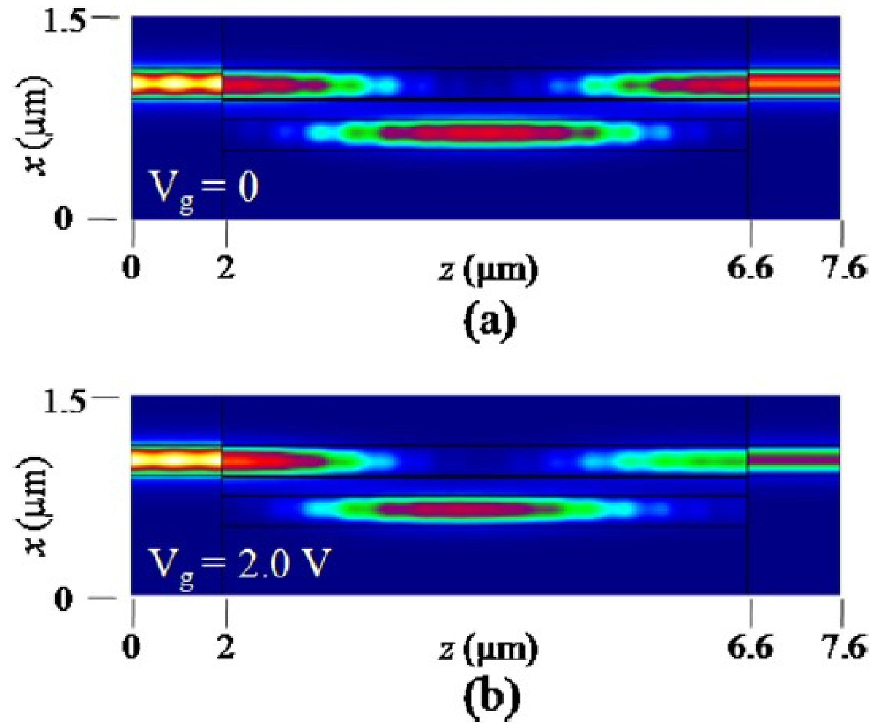

Fig. 3-5 The field intensity distribution across the device at both (a) the "Off" and (b) the "On" states [36].

3.3 HYBRID ITO TRI-CORE DIRECTIONAL COUPLER OPTICAL MODULATOR BASED ON THE EPSILON-NEAR-ZERO CHARACTERISTICS OF ITO [39]

3.3.1 Device Structure

The proposed device in this section is based on a tri-core directional coupler structure. Two Si/SiO_2 slot waveguides are separated by an intermediate hybrid plasmonic Si-SiO_2-ITO-HfO_2-Ag stack waveguide. A schematic of the EOM is illustrated in Fig. 3-6 indicating the positions of input and output ports as well as the locations of the electric electrodes. A bottom uniform 300 nm-thick silicon layer is deposited on top of the buried oxide. At the two slot waveguides, a SiO_2 layer of thickness $h_{SiO_2} = 70$ nm is sandwiched between the bottom Si slab and another 300 nm-thick Si layer as well on the top. The two slot waveguides are separated by a gap, which happens to be the width of the hybrid ITO-

integrated waveguide $w_{pl} = 300$ nm. The bottom Si and SiO_2 layers of the plasmonic waveguide are of the same dimensions of those of the slot waveguides. However, instead of the top Si layer, a stack of ITO-HfO_2-Ag is deposited on top of the SiO_2. The respective thicknesses of these layers are $t_{ITO} = 10$ nm, $t_{HfO_2} = 5$ nm, and $t_{Ag} = 10$ nm. The electric signal is applied directly on the Ag layer on top of the hybrid plasmonic waveguide at the centre. The ground signal is, on the other hand, connected to the bottom silicon slab.

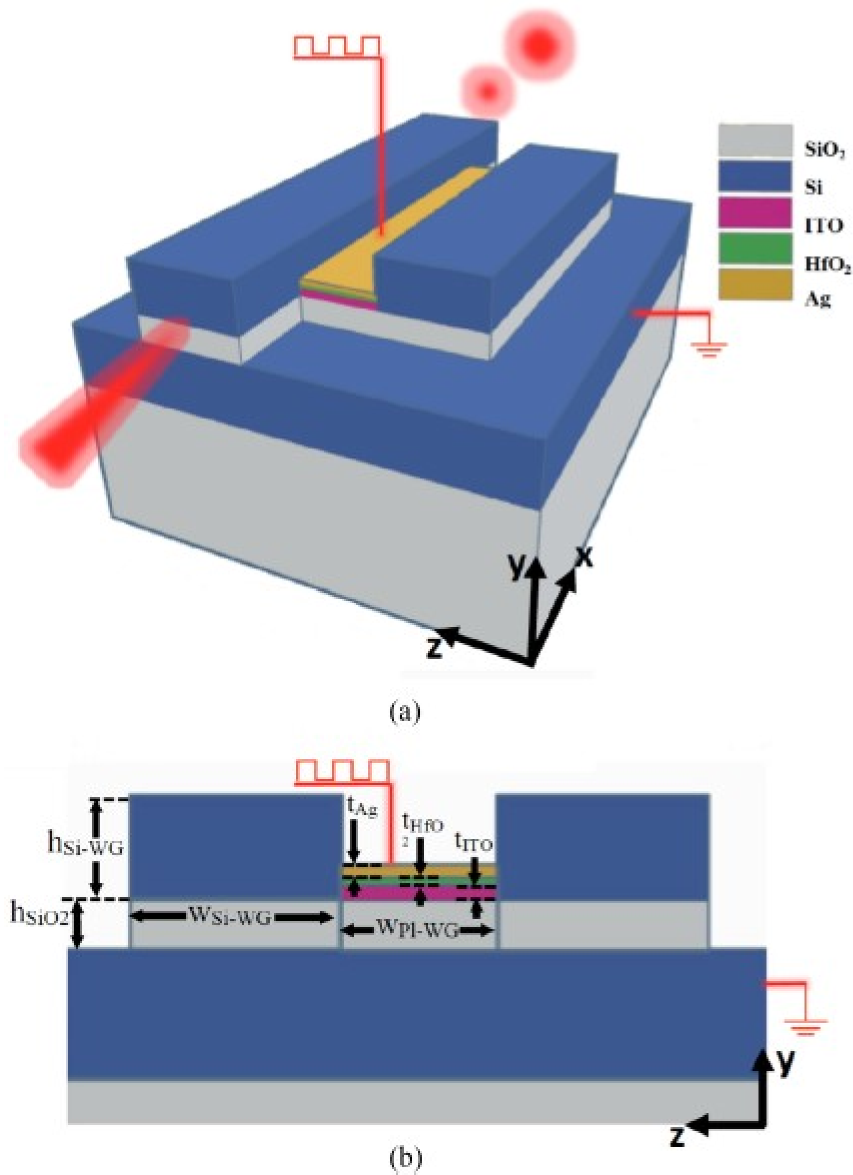

Fig. 3-6 (a) A 3D bird's eye view of the electro-optical modulator proposed in [39]. (b) A 2D cross-sectional view of the device.

3.3.2 Concept of Operation

Similar to the device discussed in 3.1 and 3.2, the principle concept of operation of this device depends on manipulating the coupling coefficient of the directional coupler through electrically tuning the ITO layer. At the “Off” state, where there is no potential drop across the ITO layer, the mode is confined in the slot SiO_2 layer as shown in Fig. 3-7a and Fig. 3-7b. At this case, the length of the hybrid modulator is designed to be equal to the coupling length of the directional coupler, hence, a maximum power output is measured. Alternatively, when applying a gating potential on the intermediate hybrid waveguide, the concentration of free carriers inside the ITO film is manipulated. This leads to an alteration in the coupling coefficient of the directional coupler affecting the level of power transmitted through the device. The mode profiles at the “On” state are plotted in Fig. 3-7c and Fig. 3-7d.

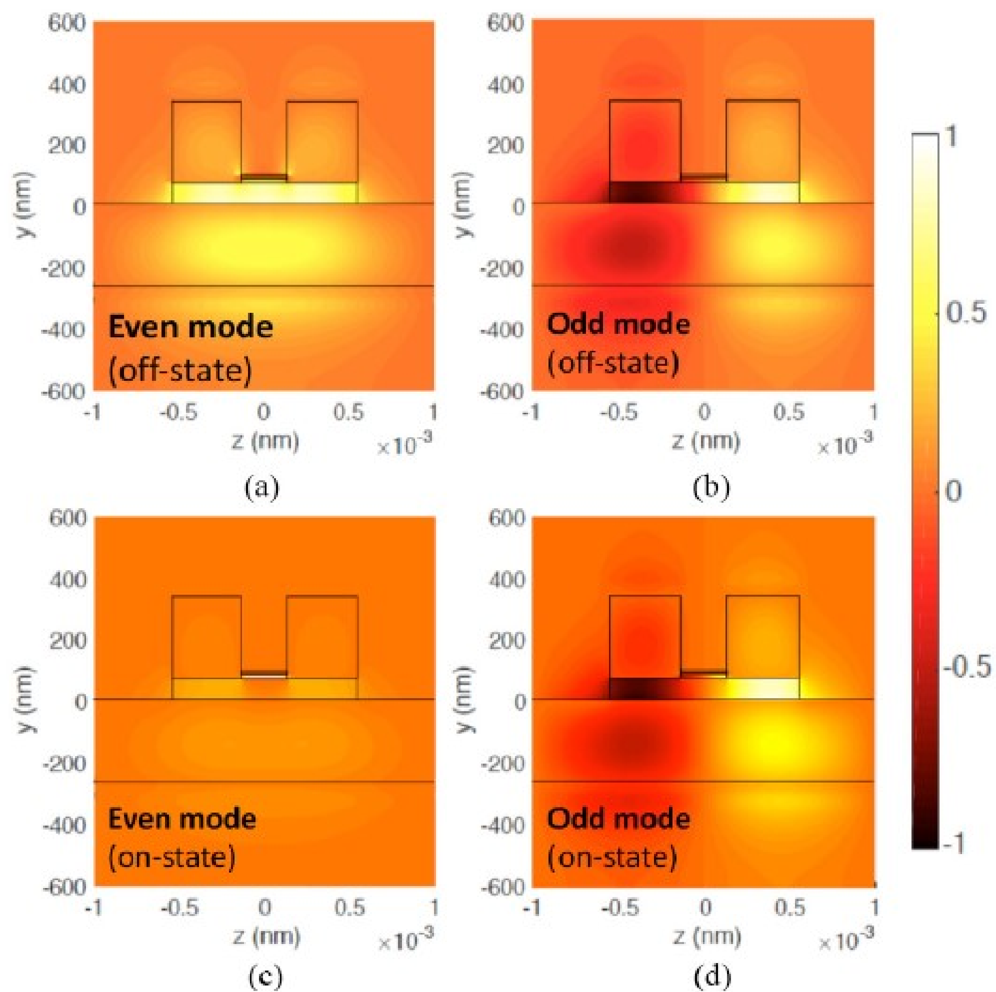

Fig. 3-7 The normalized field distributions across a cross-section cut of the device for (a) the even and (b) odd modes at the “Off” state, and (c) the even and (d) the odd modes at the “On” state [39].

3.3.3 Results

The normalized intensity of the field along the length of the device at the centre of the SiO_2 layer is graphed in Fig. 3-8. An IL and an ER of 0.06 dB and 6.1 dB, respectively, are achieved at the wavelength of 1550 nm. A maximum modulation speed of $f_{\max} = 47.5$ GHz and an average energy consumption per bit $E_{avg} = 67.1$ fJ/bit are also attained.

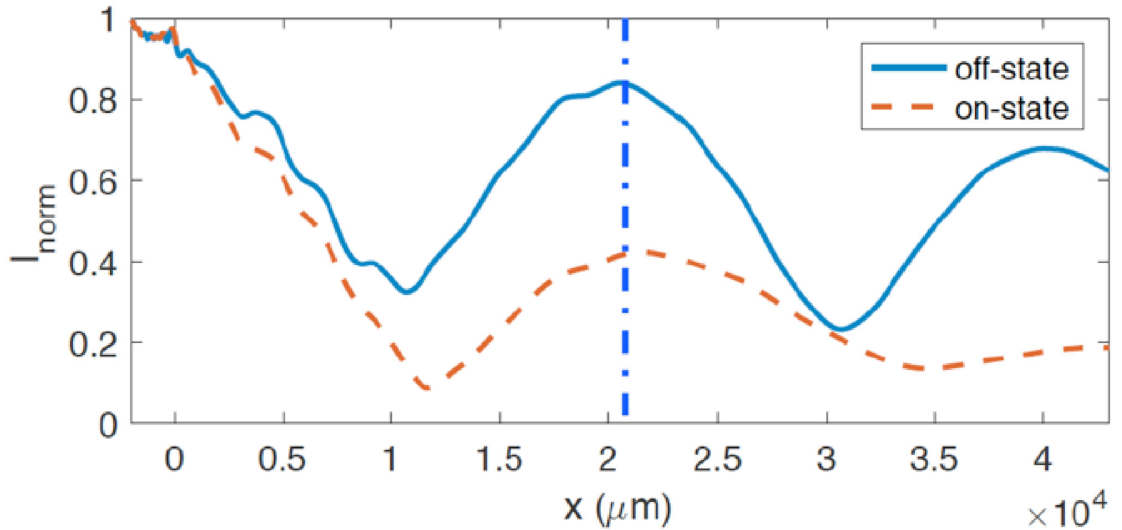

Fig. 3-8 The normalized field intensity along the device at both (solid blue) the "Off" and (dashed red) the "On" states [39].

3.4 HYBRID PLASMONIC ITO-BASED ELECTRO-ABSORPTION MODULATOR [40]

3.4.1 Device Structure

In this section, we review an EAM based on a hybrid plasmonic waveguide incorporating an ITO layer. The device is based on a Si/SiO_2 slot waveguide with the plasmonic waveguide as the modulating section in the centre. The cross-sectional and bird's eye view schematics of the device are illustrated in Fig. 3-9a and Fig. 3-9b, respectively. The input and output waveguides are standard Si-SiO_2-Si vertical slot waveguides based on the conventional SOI technology. A 70 nm thick-SiO_2 layer is sandwiched between two Si slabs of 300 nm thickness. At the modulation section, the SiO_2 layer is topped by ITO, HfO_2 and Ag layers of heights of 10 nm, 5 nm and 10 nm, respectively. This stack is

similar to the one used as an intermediate plasmonic waveguide in the device discussed in 3.3. The width of the waveguide is chosen to be 525 nm in order to ensure the mode matching in both the input/output waveguides and the hybrid plasmonic waveguide in the centre. Again, the applied potential is connected directly to the modulation section through the Ag layer, while the bottom silicon layer is connected to the ground signal.

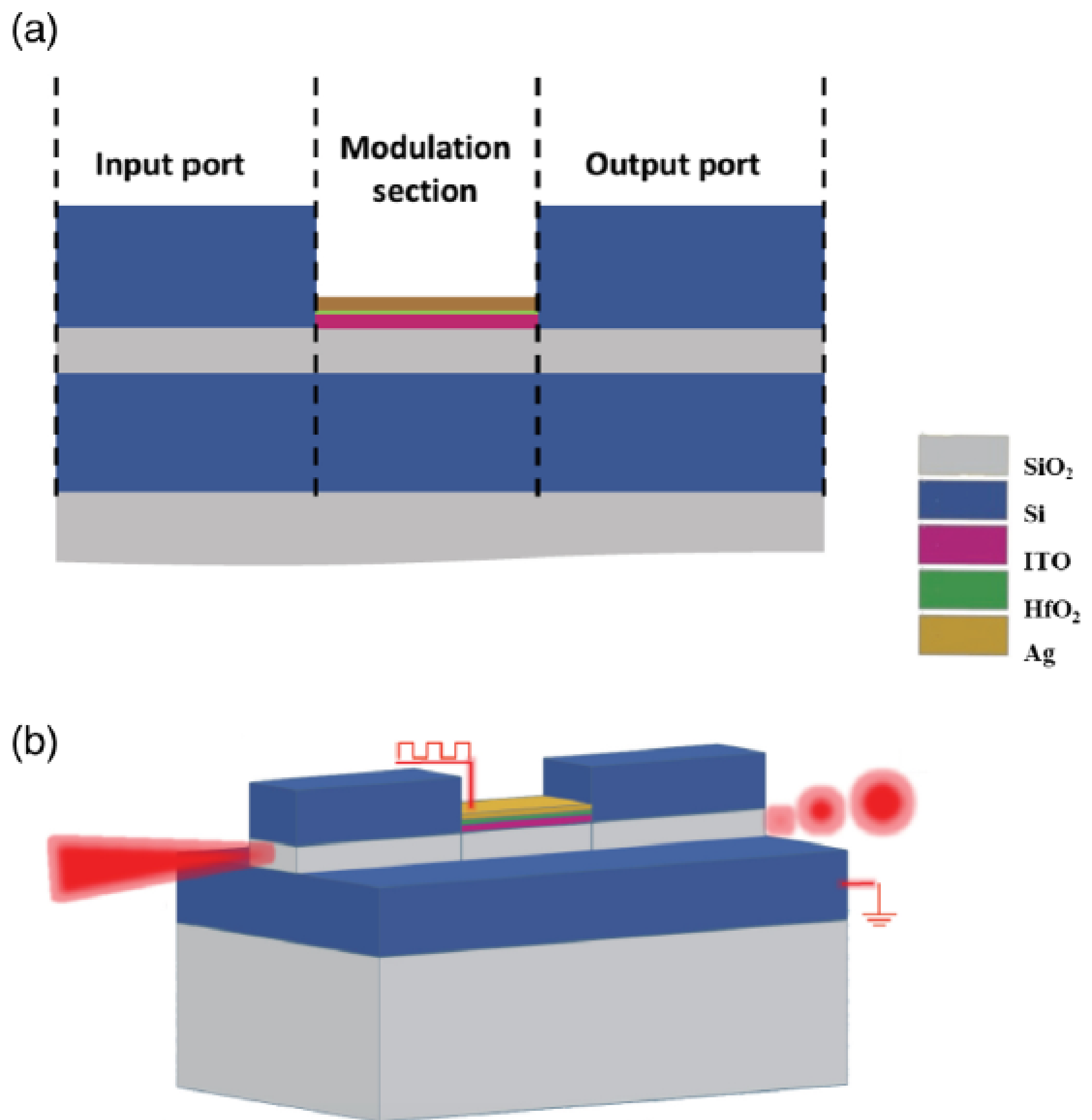

Fig. 3-9 Schematic of an electro-absorption modulator based on an ITO-integrated hybrid plasmonic waveguide as the modulation section: (a) a 2D cross-sectional view, and (b) a 3D bird's eye view [40].

3.4.2 Concept of Operation

The light is coupled to the EAM through an excitation at the input slot waveguide. It propagates along the waveguide until it reaches the interface with the modulation section. As the effective refractive indices of the modes in the slot waveguide and the hybrid plasmonic waveguide are matched, very low losses and reflections are experienced at the interface. When there is not an applied voltage on the ITO, the mode remains confined in the SiO_2 layer until it reaches the output facet with minimal IL. On the other hand, applying the gating potential to the modulation section introduces huge losses to the system as the light is strongly absorbed by the SPP modes that are formed at the ITO/HfO_2 interface. Moreover, the effective refractive index of the propagating mode inside the modulation section changes. This newly introduced mode mismatch to the device adds on the intrinsic losses of the modulator.

3.4.3 Results

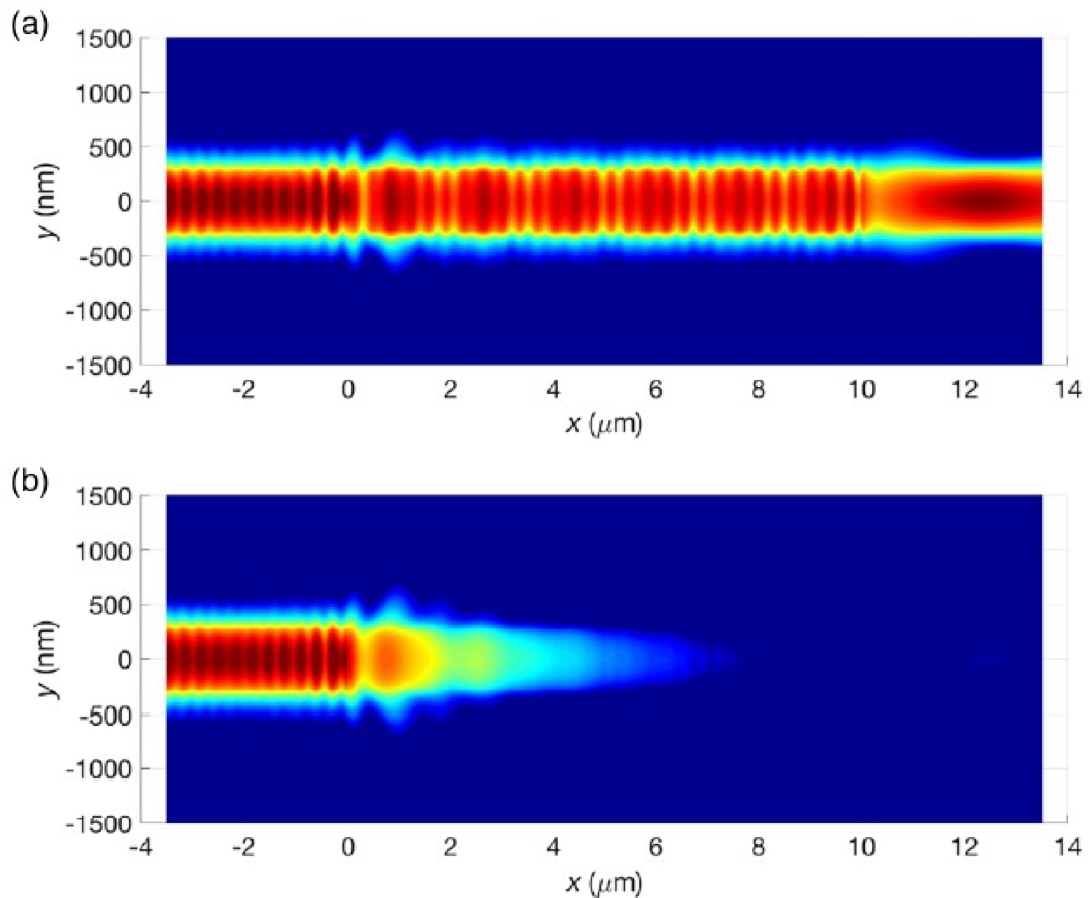

Fig. 3-10 The normalized field intensities monitored at the center of the SiO_2 slot layer along the device at both (a) the "Off" and (b) the "On" states [40].

In Fig. 3-10, the normalized field intensities along the EAM are plotted. The fields are measured at the center of the slot SiO_2 layer. At the "Off" state, an IL of about 0.69 dB is achieved. On the contrary, at the "On" state, the transmitted power level is greatly reduced due to: (1) the light absorption by the SPP modes at the ITO/HfO_2 interface due to the high concentration of free carriers inside the ITO film, and (2) the mode mismatch between the input/output slot waveguides and the coupling section. An ER of 2.3 dB for a 1 µm modulation section is also achieved at 1550 nm wavelength. This device can reach a modulation speed of about $f_{\max} = 600$ GHz and an average energy consumption of about $E_{avg} = 7$ fJ/bit.

3.5 ITO ON-CHIP ELECTRO-OPTICAL MODULATOR BASED ON RING RESONATOR STRUCTURE [41]

3.5.1 Device Structure

In this section, we discuss an EOM utilizing the ENZ characteristics of ITO in realizing a ring resonator modulator. An ITO layer is exploited in a hybrid plasmonic ring resonator structure. A standard strip silicon waveguide is the access bus, which is coupled to the mentioned ring cavity. The schematic of the device is shown in Fig. 3-11. The thickness of the Si strip waveguide is $h_{Si} = 220$ nm exploiting the standard 220 nm SOI technologies. The width of the access waveguide is chosen as $w_{strip} = 400$ nm in order to ensure single-mode operation at $\lambda = 1.55$ µm.

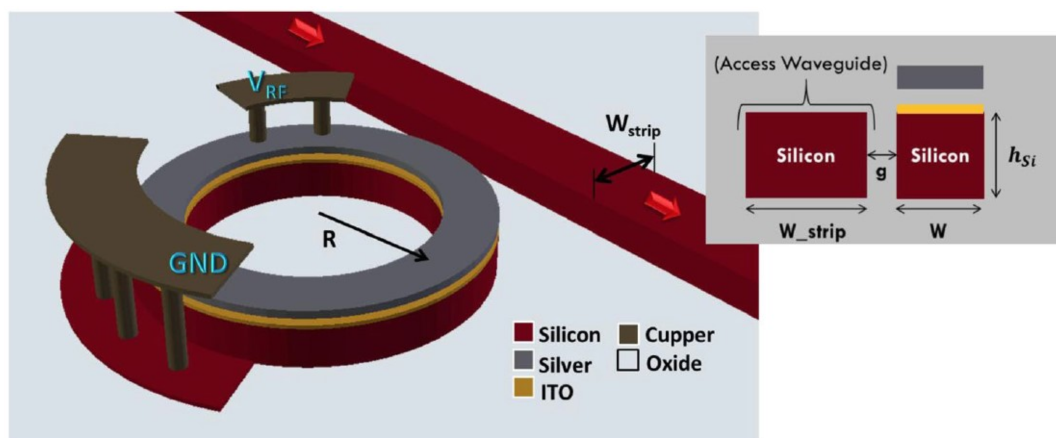

Fig. 3-11 A 3D schematic of the proposed device. An access silicon strip waveguide is coupled to a hybrid plasmonic ring resonator including an ITO layer. The inset at the right shows the cross-sectional view of the coupling region [41].

At the hybrid plasmonic cavity, the bottom 220 nm thick-Si layer is topped by ITO $h_{ITO} = 10$ nm, oxide $h_{SiO_2} = 20$ nm and silver layers. A gap of $g = 100$ nm separated between the access strip waveguide and the hybrid plasmonic waveguide. The outer radius of the ring cavity is 1 µm, and its width is $w = 200$ nm. The RF signal electrode is applied to the top silver layer of the hybrid plasmonic ring, while the ground is connected to the silicon layer of the ring as well.

3.5.2 Concept of Operation

The above-mentioned dimensions are carefully designed and optimized in order to achieve critical coupling between the access waveguide and the ring cavity. At critical coupling, maximum absorption of the resonant wavelength by the ring is achieved. Applying an RF signal on the hybrid plasmonic ring resonator creates a free carrier accumulation layer within the ITO film at the ITO/SiO_2 interface. This accumulation layer alters the effective index of refraction inside the ring cavity, which leads to an induced change in the coupling coefficients between the ring and the access waveguide. This would shift the operation of the device from critical coupling to an under-coupled region. As a result, the resonant wavelength is not absorbed well by the ring cavity. The introduced difference in the levels of transmitted power at the resonant wavelength at both cases yields a high ER.

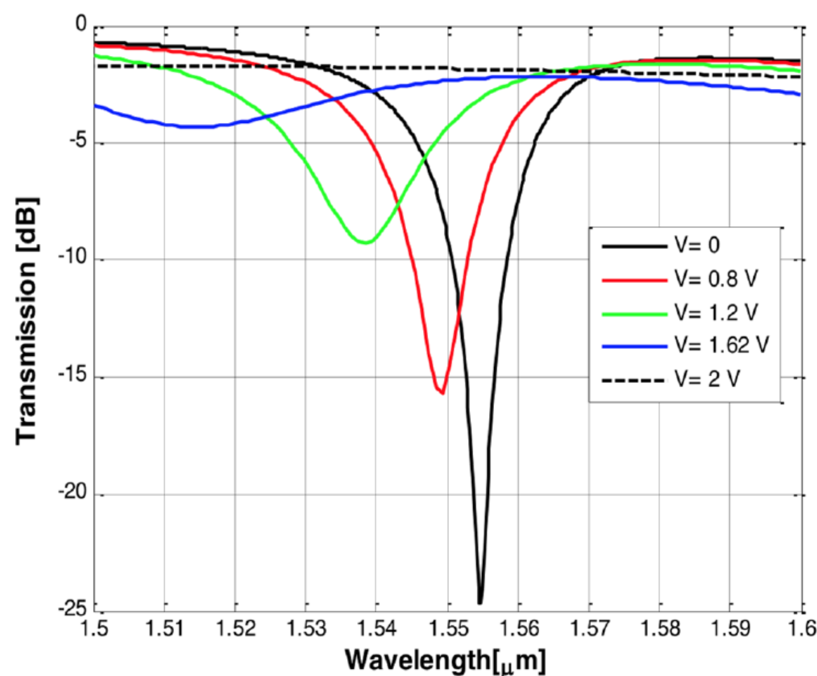

Fig. 3-12 The transmission spectra through the device at different applied voltages [41].

3.5.3 Results

At zero gating voltage, the ring resonator operates at the critically coupled point; therefore, a maximum resonance occurs and the lowest obtainable transmission level at the resonant wavelength is achieved. As shown in Fig. 3-12, at $V = 0$ V, a resonance depth of about 22.8 dB is attained around a wavelength of 1550 nm. At an applied voltage of 1.62 V, an IL of about 1.6 dB is achieved. This produces an ER of about 21.2 dB. Assuming an internal resistance of 100 Ω, this device can reach a speed limit of 1.3 THz. Moreover, an average energy consumption per bit is calculated at $E_{avg} = 3.25$ fJ/bit.

C h a p t e r   F o u r

4 RING RESONATOR ELECTRO-OPTICAL ITO-BASED MODULATOR

In this chapter, a novel silicon ring resonator modulator is proposed utilizing an ITO layer on a silicon-on-insulator (SOI) platform. A pure silicon access waveguide is introduced, and a detailed discussion of the coupling junction configuration is presented. The ITO layer is tuned to operate around the ENZ region achieving an extinction ratio (ER) of about 14 dB and a very low insertion loss (IL) of about 0.076 dB.

4.1 DEVICE STRUCTURE

As presumed by the Drude-Lorentz model, the physical origin of the EO modulation is the free carrier concentration effect. Hence, if the carrier concentration in a waveguide-type device design can be electrically modified, an EO modulation could be expected at this point. Yet, it is strongly profitable when the change in the ITO's complex permittivity has a great impact on the effective mode index of the device. Thus, a mode field enhancement technique is required as observed in plasmonics, optical cavities, or slot waveguides [72].

Consequently, a slot waveguide is chosen as the access waveguide to the device, as shown in Fig. 4-1. A SiO2 layer of 20 nm thickness is sandwiched between two 220 nm-thick Si slabs. The ring, on the other hand, has additional ITO and HfO_2 layers on top of the SiO_2 layer of thicknesses of 10 nm and 5 nm, respectively.

It is separated from the access waveguide by a 150 nm air gap. The width of the access waveguide is set to be 250 nm, while the width of the ring is 280 nm in order to compensate the mismatching index resulting from the introduction of the ITO/HfO_2 junction. The outer radius of the ring cavity is set to be 980 nm. The details of parameters' optimization and the process of choosing the mentioned specific dimensions of the device are elaborated in the next section.

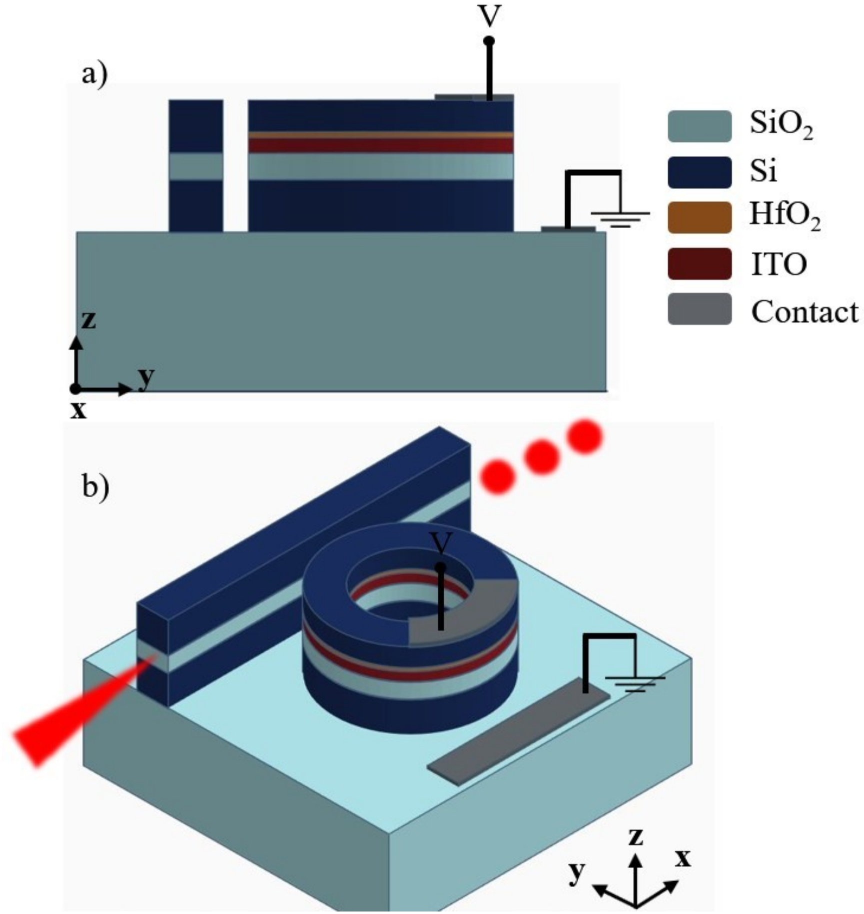

Fig. 4-1 a) A sideview schematic of the modulator device. The ring (on the right) contains an embedded ITO layer. b) A bird's eye 3D view of the modulator device with the positions of the contacts illustrated.

The refractive indices of Si, SiO_2 and HfO_2 at the operating wavelength are 3.48, 1.44 and 1.98, respectively. The top Si layer of the ring cavity is heavily doped $\left(N_d = 1\times10^{18}\ \text{cm}^{-3}\right)$ so that it could be used as a contact with relatively low resistivity $r_{Si} \approx 0.03\ \Omega\cdot\text{cm}$ [35].

4.2 MODAL ANALYSIS

4.2.1 Access Waveguide Width

As mentioned in the previous section, a horizontally slotted access waveguide structure is chosen due to its low losses as well as the good field confinement. According to the dimensions of both the bottom and top Si slabs as well as the SiO2 slot, a single mode operation is granted for a range of widths between 140 nm and 250 nm. The propagation

losses vs. this range of waveguide widths are depicted in Fig. 4-2. As expected, the losses decrease as the width of the access waveguide increases. As a result, a width of 250 nm is chosen for this design in order to grant the least propagation losses possible as well as single mode operation.

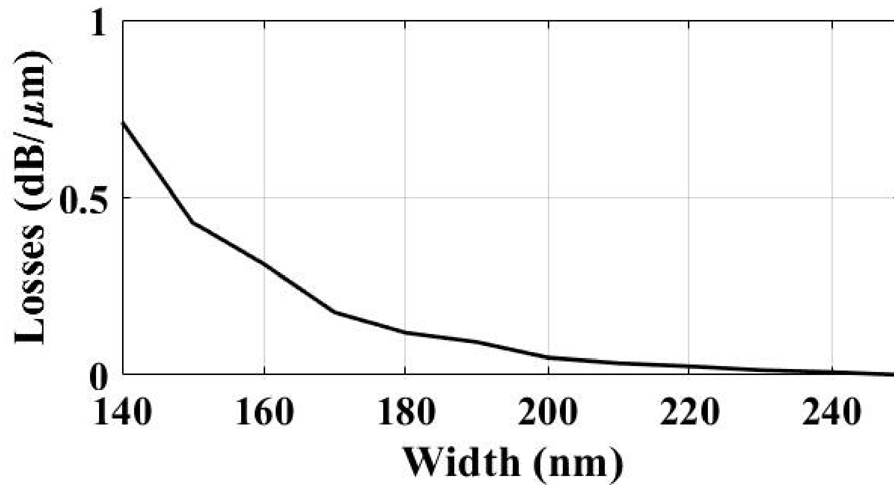

Fig. 4-2 Normalized propagation losses of the fundamental mode vs. the width of the access waveguide.

4.2.2 Ring Cavity Width

For a slotted waveguide consisting of two 200 nm-thick Si slabs and a SiO2 layer of 20 nm thick sandwiched between them, and a width 250 nm, the effective refractive index of the fundamental mode is found to be around 2.25. The introduction of the ITO/HfO2 combination in the ring cavity is expected to shift the effective index of the mode inside it. Therefore, a change in the width of the ring cavity should accommodate this difference. The effective refractive index of the fundamental mode vs. the width of the waveguide of the ring cavity is shown in Fig. 4-3.

An effective refractive index of 2.25 is achieved at a width of 280 nm. This effective index matching between the access waveguide and the ring cavity grants the least possible coupling losses. This point of operation is indicated in Fig. 4-3 as a small pale red dot.

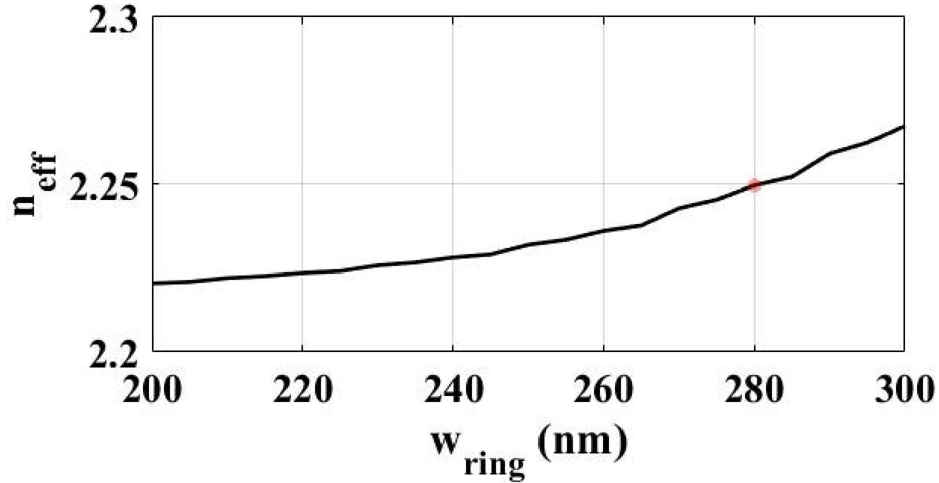

Fig. 4-3 The change in the effective refractive index of the fundamental mode inside the ring cavity vs. its width. The pale red dot indicates the intersection between the designed width and the required effective index.

4.2.3 Ring Cavity Modal Analysis

Eigenmode solver analysis with a perfect matching layer (PML) absorbing boundary conditions is used to simulate and study the modal response of the device. The propagating modes inside the ring cavity are studied in both the "On" and "Off" states. It is found that, while operating at the "On" state, the ITO acts as a conventional dielectric material; thus, most of the power is confined in the SiO2 slot layer as depicted in Fig. 4-4a. On the contrary, while at the "Off" state, the applied gating voltage of $V_g = 2.35$ V leads to an accumulation of the free carriers at the ITO/HfO2 interface. This renders a lossy mode at which the light is confined in the ITO layer as shown in Fig. 4-4b. Table I summarizes the values of the effective refractive indices of the operating modes inside the ring cavity in both "On" and "Off" states. A percentage of the electric field intensity distribution inside the ITO layer in both states is shown as well.

The resultant difference between the effective indices of the two modes at the "On" and "Off" states affects the coupling conditions. This difference in the effective indices causes a shift in the ring's resonant wavelength.

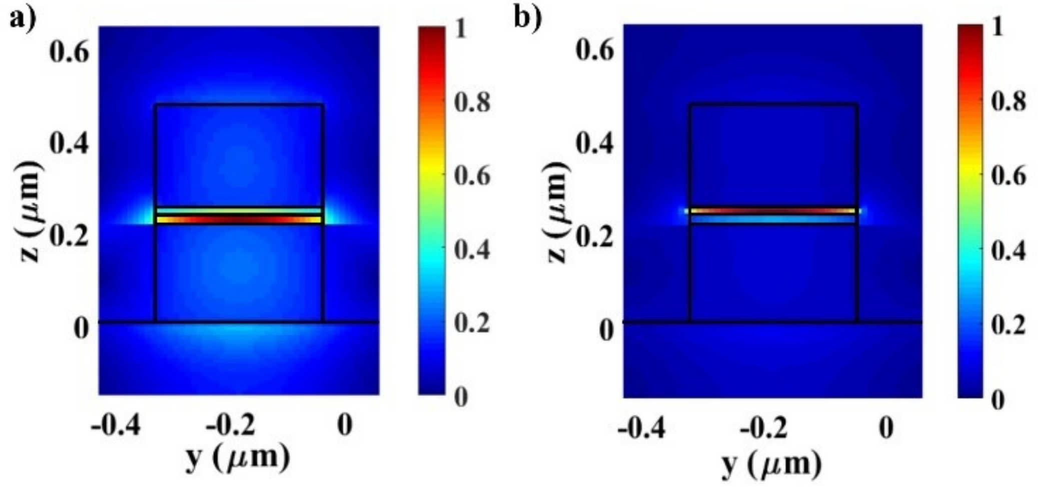

Fig. 4-4 Normalized field intensity at the ring cavity in both a) "On" state (V_g = 0 V), and b) "Off" state (V_g = 2.35 V).

Table I The effective refractive indices of the modes inside the ring cavity in both "On" and "Off" states.

State	V_g	Effective refractive index	Electric field intensity % in ITO
"On"	0 V	$2.249 + 9.032 \times 10^{-5} i$	15%
"Off"	2.35 V	2.049 + 0.284 i	60%

4.2.4 Separation Gap and Outer Radius

After choosing the widths of both the access waveguide and the ring cavity according to the previous study, an appropriate outer radius as well as a separation gap should be carefully studied. For the outer radius of the ring cavity, the optical path length difference (OPD) equation must be satisfied as follows.

$$OPD = 2\pi R_o n_{eff} = m\lambda_{res} \quad (5.1)$$

where Ro is the outer radius of the ring, n_{eff} is the effective refractive index of the propagating mode inside the cavity, m is the mode number of ring resonator (must be an integer), and λ_{res} is the resonant wavelength. For m=9, the outer radius of the ring is found to be around 980 nm.

At these dimensions, a separation gap between the access waveguide and the ring cavity should be carefully chosen in order to grant critical coupling, at which the ring achieves the maximum absorbance of the resonant wavelength. At an outer radius of 980 nm, the

transmission spectra through the ring resonator device at different separation gaps are shown in Fig. 4-5. As illustrated, the critical coupling condition is met at a separation gap of 150 nm.

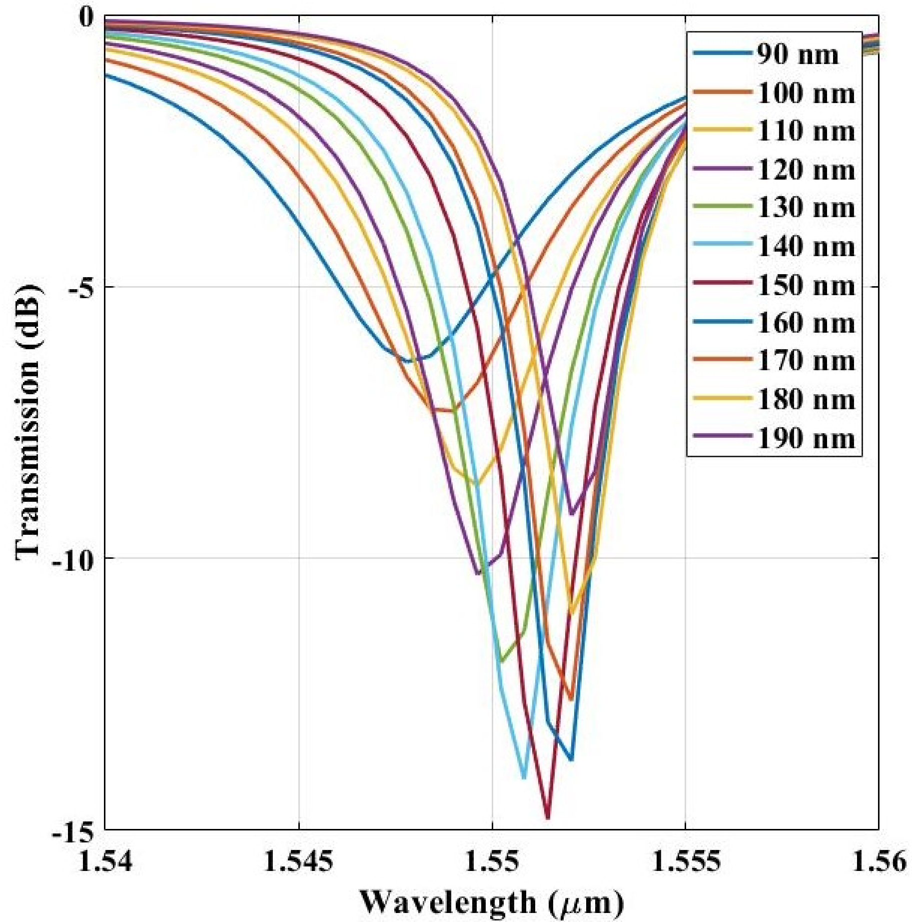

Fig. 4-5 The transmission spectra through the ring resonator of an outer radius of 980 nm at different separation gaps ranging from 90 nm to 190 nm.

4.3 RESULTS AND DEVICE PERFORMANCE

As mentioned in the previous section, switching from the "On" state to the "Off" state by applying a gating potential of 2.35 V, leads to an induced difference in the effective refractive index of the propagating mode. This difference procures a change in the coupling conditions between the access waveguide and the ring cavity leading to a shift in the resonant wavelength.

The dimensions of the access waveguide as well as the separation between it and the ring cavity are carefully designed such that a critical coupling between the access waveguide and the ring occurs. The output from a TM-excited mode presents a resonance notch in

its spectrum at the 1.55 μm wavelength. As shown in Fig. 4-6, the ER is about 14 dB while the IL is found to be around 0.076 dB at the chosen outer radius of 980 nm. The Q-factor here is chosen to be a relation between the ER and IL as in $Q = ER/IL$. This yield a Q-factor of about 185.

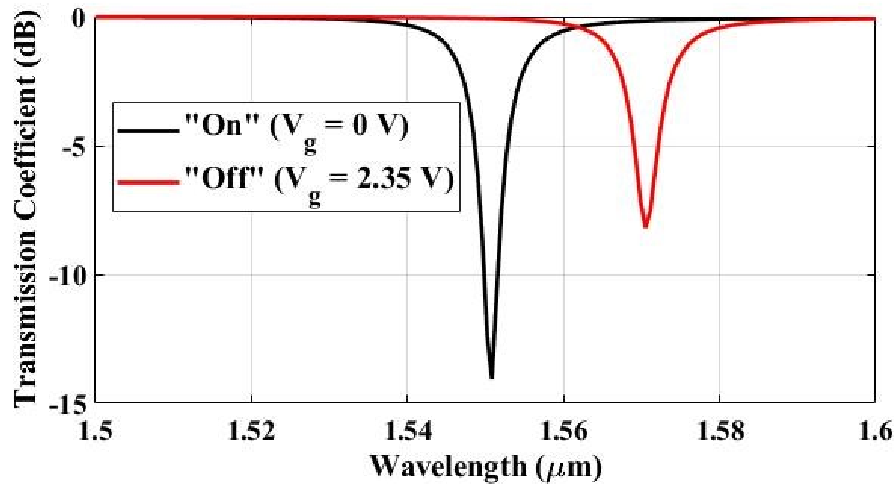

Fig. 4-6 The output spectrum of a TM-excited mode at both the "On" and "Off" states at a ring's outer radius of 980 nm.

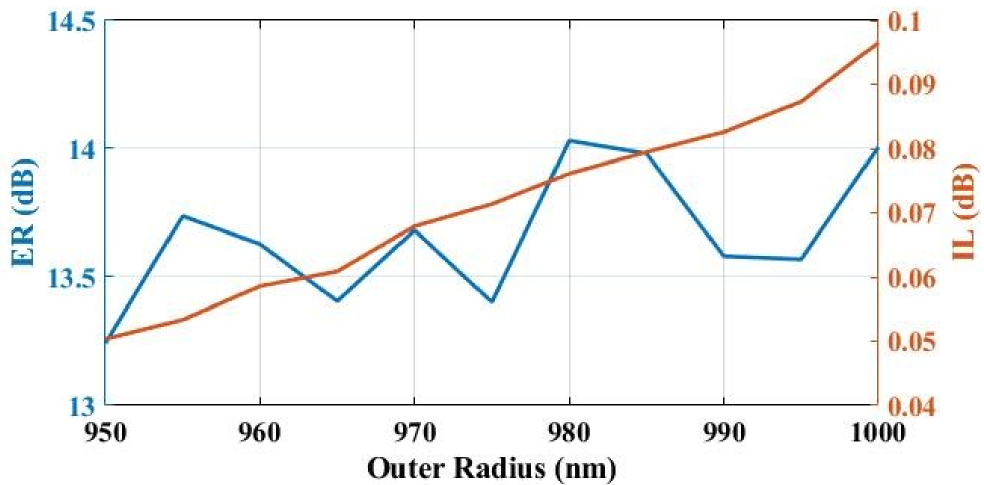

Fig. 4-7 The extinction ratios (left) and the insertion losses (right) to several devices with an outer radius ranging from 970 nm to 1 μm.

A parametric sweep of the outer radius is performed covering the range from 950 nm to 1 μm. Both the ER and the IL are plotted in Fig. 4-7. It is shown that the highest ER value occurs at an outer radius of 980 nm with the IL varying from 0.05 dB to almost 0.1 dB all over the other values. It is worth mentioning that these values are calculated at the resonant wavelengths for each device, which are shifted from the operation wavelength

of 1550 nm. The fluctuations in the ER values with the outer radius of the ring cavity are caused due to the change in the resonance conditions. Some values of the outer radius do match an exact mode of the ring resonator as in (5.1), while other radii don't.

Moreover, the ER of the device for a range of separation gaps from 90 nm to 190 nm is shown in Fig. 4-8. The highest obtainable ER value is achieved at a separation gap of 150 nm between the access waveguide and the ring cavity. These results agree with the data previously illustrated in Fig. 4-5.

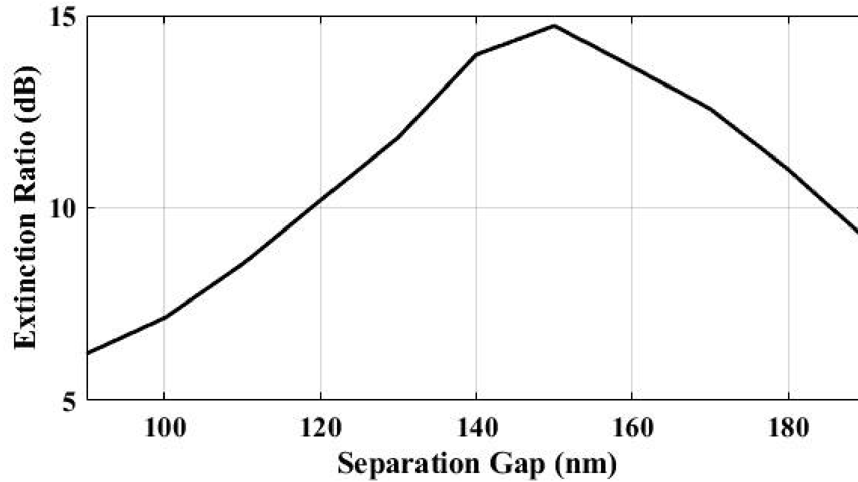

Fig. 4-8 The extinction ratio of the device at different separation gaps ranging from 90 nm to 190 nm.

The modulation speed of an optical modulator device is defined by its resistance-capacitance product as $f_{\max}^{-1} = 2\pi RC$. The capacitance here is defined as follows.

$$C = \frac{\varepsilon_{HfO_2} \times A}{t_{HfO_2}} = \frac{\varepsilon_0 \times \kappa_{HfO_2} \times \pi \times \left(R_o^{\ 2} - R_i^{\ 2}\right)}{t_{HfO_2}} \tag{5.2}$$

where R_o is the outer radius of the ring cavity while the inner radius is R_i. By applying (5.2) for the proposed device, this yields a capacitance of 65.4 fF. Assuming an internal resistance of 50 Ω, the speed limit of the modulator is calculated to be 48.67 GHz. The energy consumption of the device depends on the device's capacitance as well. It is estimated to be $E_{avg} = CV_g^{\ 2}/2$. For an applied gating potential of 2.35 V, the average energy consumption of the proposed modulator is 0.18 pJ/bit.

Table II summarizes the different performance parameters of the proposed design compared to other ITO-based modulators [36], [38], [39], [41]. All the devices proposed in [36], [38], [39] are based on directional coupler scheme. Lower values of the ER are noticed compare to the proposed device here; however, directional coupler, in general, enjoy larger bandwidth and higher robustness against any fabrication or temperature tolerances. Ring resonators, on the other hand, like in [41], can reach higher ER values and comparable IL compared to directional coupler-based devices. However, this comes at the expense of lower operating bandwidth and high sensitivity to tolerances of the system. Compared to [41], the proposed modulator achieves lower ER, but with lower IL as well. The very low value of IL of the proposed device here is achieved by not using metals in the structure. The ER / IL combination of the device yields a very much higher Q-factor, which is defined as Q = ER / IL.

Table II Summary of the performance parameters of the proposed device (in bold) compared with other ITO-based modulators.

ER *dB*	IL *dB*	E *fJ/bit*	f_{max} *GHz*	λ *μm*	V_g *V*	Q	Ref.
6.7 2.3	0.032 0.036	78.9	116	1.31 1.55	2.4	209 63.8	[38]
5	0.87	330	257	1.55	2.3	5.75	[36]
6.14 11.4	0.06 1.65	67.1 22.7	47.5 140	1.55	2.35	102 6.9	[39]
22.8	1.6	3.25	1300	1.55	1.62	36.5	[41]
14	**0.076**	**180**	**48.67**	**1.55**	**2.35**	**185**	-

4.4 CONCLUSION

An electro-optic modulator based on an ITO-integrated ring resonator is proposed here. Two distinct operating states are studied: the "On" state where no gating bias is applied to the ring cavity, and the "Off" state where a gating potential of 2.35 V is applied. Tuning the ITO layer to an ENZ region, the coupling conditions between the access slot waveguide and the ring cavity change dramatically. This difference in the effective refractive index leads to a shift in the resonance wavelength of the ring resonator.

An ER of about 14 dB and an IL of only 0.076 dB are attained at an outer radius dimension of 980 nm. The device is compact and CMOS compatible.

Chapter Five

5 DIRECTIONAL COUPLER ELECTRO-OPTICAL ITO-BASED MODULATOR

In this chapter, an EOM based on a directional coupler structure utilizing ITO as the EO active medium is proposed. A very low IL of only 0.9 dB as well as an acceptable ER of about 9 dB are attained at a standard telecommunication wavelength of 1.55 μm. An eigen mode solver as well as a finite difference time domain (FDTD) tool with perfect matched layers (PML) boundaries is used to design the device and simulate its operation indicating its overall performance.

Including the ITO layer inside the coupler arm section, rather than between the two ports of the directional coupler [36], [38], [39], brought about a much smaller footprint of the device. A reduction in size that would, in return, reduce the capacitance of the device significantly which allows a faster response of the device.

5.1 DESIGN PROCEDURE

5.1.1 Device Structure

In this section, we propose an ITO-integrated EOM based on a directional coupler device. The schematic of the device is shown in Fig. 5-1, where an access slotted waveguide couples with another waveguide including an ITO/HfO_2 combination. A horizontally slotted waveguide increases the confinement [72], which results in higher EO effects in the coupler arm.

The access waveguide consists of a SiO_2 layer of thickness of 20 nm sandwiched between two 220 nm Si slabs. The width of the access waveguide is set to be 250 nm. On the other hand, the coupler arm waveguide consists of a bottom 220 nm-thick Si slab, topped by a SiO_2, ITO and HfO_2 with thicknesses of 20 nm, 10 nm and 5 nm, respectively. A top Si layer of 205 nm thickness is deposited on the HfO_2 layer. An air gap of 100 nm separates the access waveguide from the coupler arm waveguide. The device is designed to operate at the standard telecommunication wavelength of 1.55 μm, at which the refractive indices of Si, SiO_2 and HfO_2 are 3.48, 1.44 and 1.98, respectively.

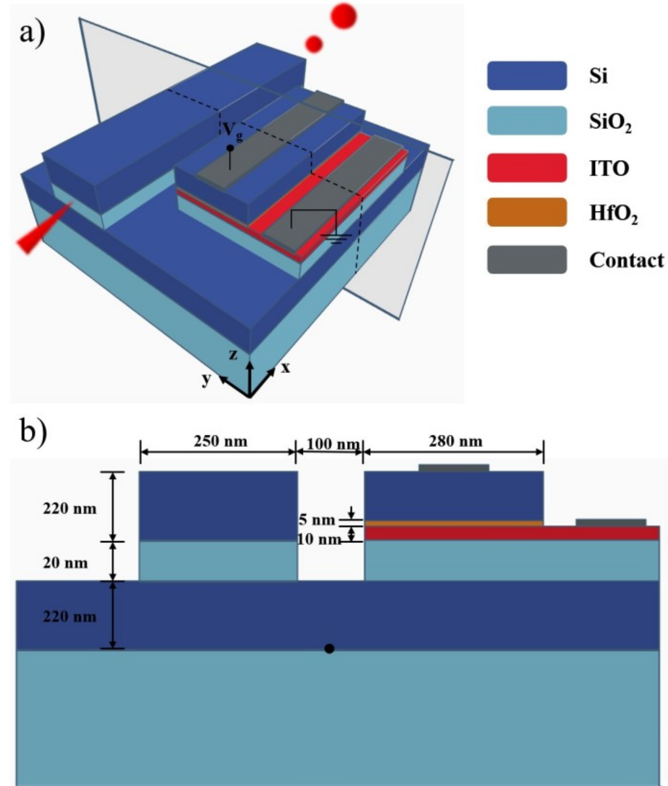

Fig. 5-1 An electro-optic ITO-integrated modulator based on a directional coupler design. a) A bird's eye view of the structure, b) A cross-sectional view taken at the section cut in (a).

For the lowest possible coupling losses between the access waveguide and the coupler arm waveguide, the effective refractive indices at both waveguides have to match. For the dimensions of the access waveguide, which are mentioned above, the effective refractive index of the fundamental TM-excited mode is about 2.25. Using an eigen mode solver tool [88], a detailed study of the effective refractive index of the propagating mode inside the coupler arm waveguide vs. its width is held. As shown in Fig. 5-2, a width of 280 nm of the coupler arm waveguide satisfies the matching condition of the directional coupler. Therefore, in our proposed device, a width of 280 nm is chosen for the coupler arm waveguide in order to grant the least possible coupling losses for the structure.

Regarding the top Si layer in the coupler arm waveguide, it acts as a contact for the applied electric signal by doping it by a moderately high concentration of $N_d = 10^{18}$ cm^{-3}, which renders a relatively low resistivity of about $r_{Si} \approx 0.03$ Ω.cm [35]. As depicted in Fig. 5-1, the metal contact, at which the gating potential is applied, is placed on top of the doped Si layer. The thickness of the Si slab as well as the ITO/HfO_2 combination assures the optical isolation of the TM-excited mode. On the other hand, the ground metal contact is

placed on an extension of the ITO layer. A safe margin is taken into consideration as well to ensure optical isolation.

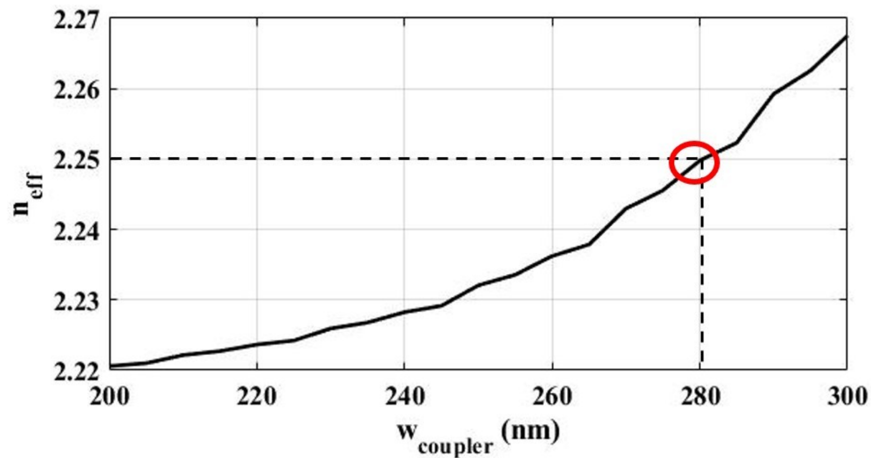

Fig. 5-2 The variation in the effective refractive index of a TM-excited mode inside the coupler section waveguide against its width.

5.1.2 Concept of Operation

As mentioned before, there are two state of operation for this proposed device; the “On” state, where there is no applied gating voltage on the coupler arm waveguide, and the “Off” state, where an electric potential of 2.35 V is applied on the device. In the “On” state, the input light beam couples to and back from the coupler arm as it is designed to be twice the coupling length (more details are elaborated in the next section). The matching of the effective refractive indices of the access waveguide and the coupler arm waveguide grants minimal coupling losses, hence minimum obtainable IL. On the other hand, at the “Off” state, an applied voltage of 2.35 V on the coupler arm waveguide leads to a high accumulation of the free carriers in the ITO layer at the ITO/HfO_2 interface. This high concentration of the free carriers introduces high losses to the system, causing a severe reduction in the output power.

For the fabrication of this device, standard techniques of photolithography and etching of 220 nm SOI platform are needed. First of all, a 20 nm of SiO_2 is grown on top of the 220 nm layer of Si. After that, a mask is used to etch the unwanted parts leaving the access waveguide as well as the coupling arm waveguide. After that the ITO film along the HfO_2 layer are deposited above the coupler arm waveguide. Finally, the top Si slabs are grown for both the access waveguide and the coupler arm waveguide.

5.2 MODAL ANALYSIS

The coupling length, which is discussed in more details in 2.3.5, of the directional coupler that is the required length for all the power to couple from one arm to the other, is estimated through the following formula.

$$L_C = \frac{\lambda}{2\left(n_{even} - n_{odd}\right)} \tag{5.1}$$

At the "On" state, the effective index of the even mode is found to be $2.319 + 9.869 \times 10^{-5}$ i, while an effective refractive index of $2.008 + 6.763 \times 10^{-5}$ i is calculated at the "Off" state. According to (5.1), the coupling length is found to be approximately 2.5 μm, for which the full power couples from one arm to the other. However, in our case, we need the power to couple from the access waveguide to the coupler arm and back again to the access waveguide. Therefore, the coupler arm waveguide's length is designed to be twice the coupling length $L_{coupler} = 5\ \mu\text{m}$. In Fig. 5-3, the normalized field intensity distributions E_z of the even and odd modes of both the "On" and "Off" states are illustrated. It can be noticed that a the "On" state, most of the field is confined in the SiO_2 layer at both the even (Fig. 5-3a) and odd (Fig. 5-3b) modes. Applying the gating potential of V_g = 2.35 V leads to a high accumulated concentration of the free carriers at the ITO/HfO_2 interface. Consequently, most of the power of the even (Fig. 5-3c) and odd (Fig. 5-3d) modes in this case are confined inside the ITO layer.

Quantitative values of the effective refractive indices for both the even and odd modes at the "On" and "Off" states are expressed in Table III. At the "Off" state, a huge increase in the imaginary parts of the effective refractive indices of the even and odd modes occurs. This explains the large losses introduced to the system at the "Off" state.

5.3 RESULTS AND DISCUSSION

As stated in the previous section, at the "On" state, the device operates as a conventional directional coupler device with the power bouncing to and from the coupler arm waveguide. Minimal coupling losses are granted due to the effective refractive index matching between the modes propagating in the access waveguide as well as the coupler arm waveguide. This case is depicted in Fig. 5-4a, where most of the input power couple

to the coupler arm waveguide and then couples back to the access waveguide. About 82% of the input power can be measured at the output facet in this case. The 18% loss in power comes back to the propagation losses associated with the fundamental TM-excited mode inside the access waveguide as well as the coupler arm waveguide. Moreover, there is also a fraction of coupling losses introduced at this case due to the lack of full matching between the effective refractive indices.

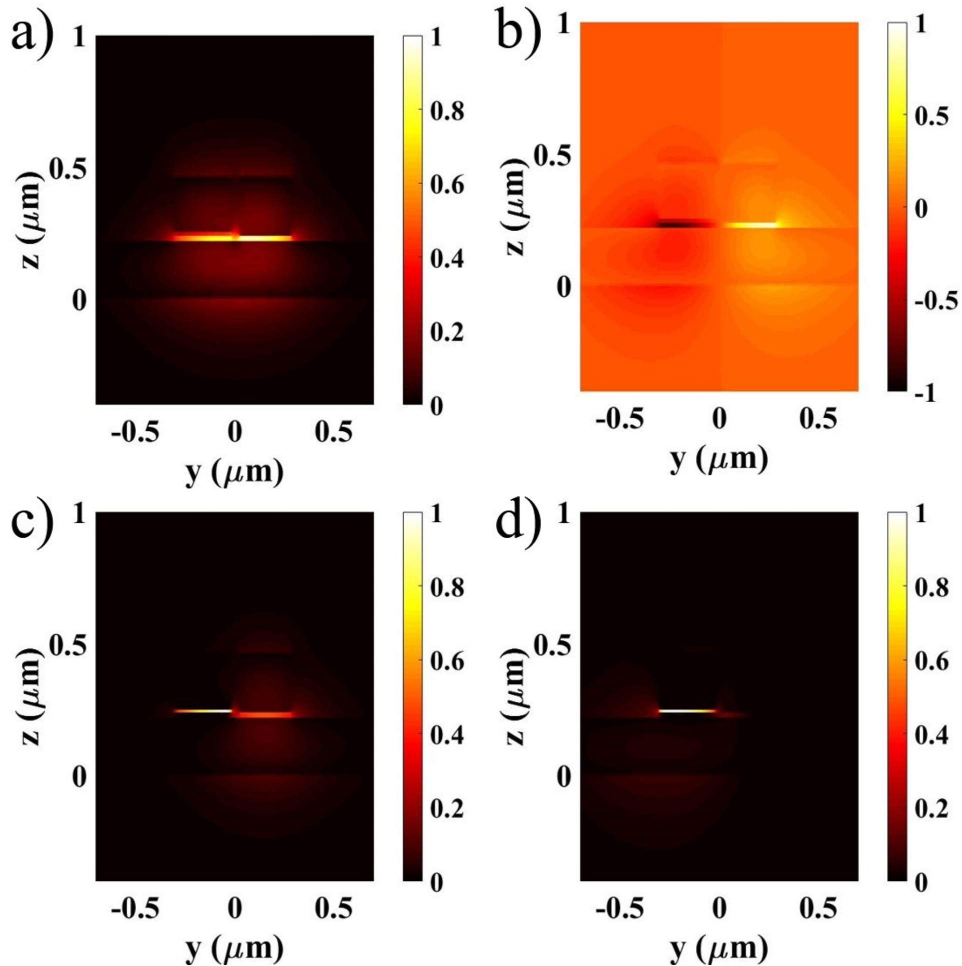

Fig. 5-3 The normalized electric field distribution E_z across a vertical plane cut of the device at the "On" state: (a) even mode – (b) odd mode, and the "Off" state: (c) even mode – (d) odd mode.

Table III Effective refractive indices of the even and odd modes at both the "On" and "Off" states

State	V_g	Mode	Effective refractive index
"On"	0 V	Even	$2.319 + 9.869 \times 10^{-5}$ i
		Odd	$2.008 + 6.763 \times 10^{-5}$ i
"Off"	2.35 V	Even	2.295 + 0.081 i
		Odd	1.925 + 0.205 i

At the "Off" state, most of the power confines inside the ITO layer near the ITO/HfO_2 interface introducing huge losses to the device. As shown in Fig. 5-4b, most of the power, which couples to the coupler arm, decays significantly. This leaves a very small portion of the power coupling back to the access waveguide and passing through the output face. Only 10% of the input power could be measured at the output for an applied potential of 2.35 V. These results yield an IL of about 0.86 dB for the device and an ER of about 9 dB at the standard telecommunication wavelength of 1.55 μm. At other important telecommunication wavelengths of operation such as the 1.49 μm and the 1.31 μm windows, the proposed device achieved an IL of 0.88 dB and an ER of 5.93 dB at 1490 nm, and an IL and ER of 1.28 dB and 4.61 dB, respectively, at the 1310 nm wavelength. These results can be greatly enhanced by modifying the dimensions of the device according to the wavelength of interest.

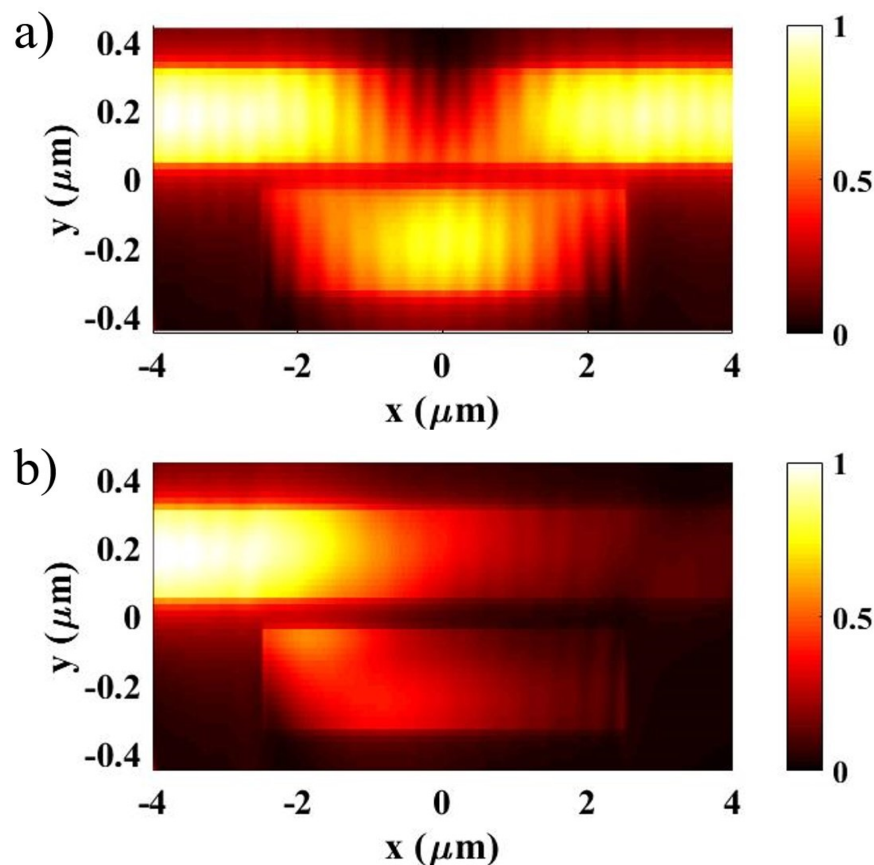

Fig. 5-4 The normalized field intensity E_z propagating through the device in both (a) the "On" state (V_g = 0 V) and (b) the "Off" state (V_g = 2.35 V).

Over a wideband of operation, from 1.4 μm to 1.7 μm, the achieved ER and IL of the device are shown in Fig. 5-5a and Fig. 5-5b, respectively. Since the imaginary part of the

refractive index of the ITO increases with the wavelength, it is noticed that the ER increases at higher wavelengths. For a separation gap of 100 nm between the access waveguide and the coupler arm waveguide, a maximum ER of about 16.5 dB is achieved at a wavelength of 1.67 μm. A reduction in the separation gap would "blue" shift the peak of the ER. At a 50 nm-gap, a maximum ER of 22.5 dB occurs at a wavelength of 1.63 μm. This reduction in the gap would increase the ER all over the spectrum, raising from 9 dB to 12 dB at the 1550 nm wavelength of operation. Further reduction is expected to offer higher ER; however, fabrication constraints would complicate the task. On the other hand, the IL doesn't experience much variation across this band at both separations, ranging from 0.8 dB to 1.6 dB all over the spectrum. Meanwhile, the values of the ER achieved by the proposed device for different gating voltages is shown in Fig. 5-6. A maximum ER of about 13 dB can be obtained at an applied potential of 2.7 V. This increase in the ER comes on the expense of a higher energy consumption of the device. An operation around the ENZ point (i.e. $V_g = 2.35$ V) ensures an ER of at least 10 dB, which is considered the minimum acceptable ER value for high performance modulators, while attaining minimal energy consumption.

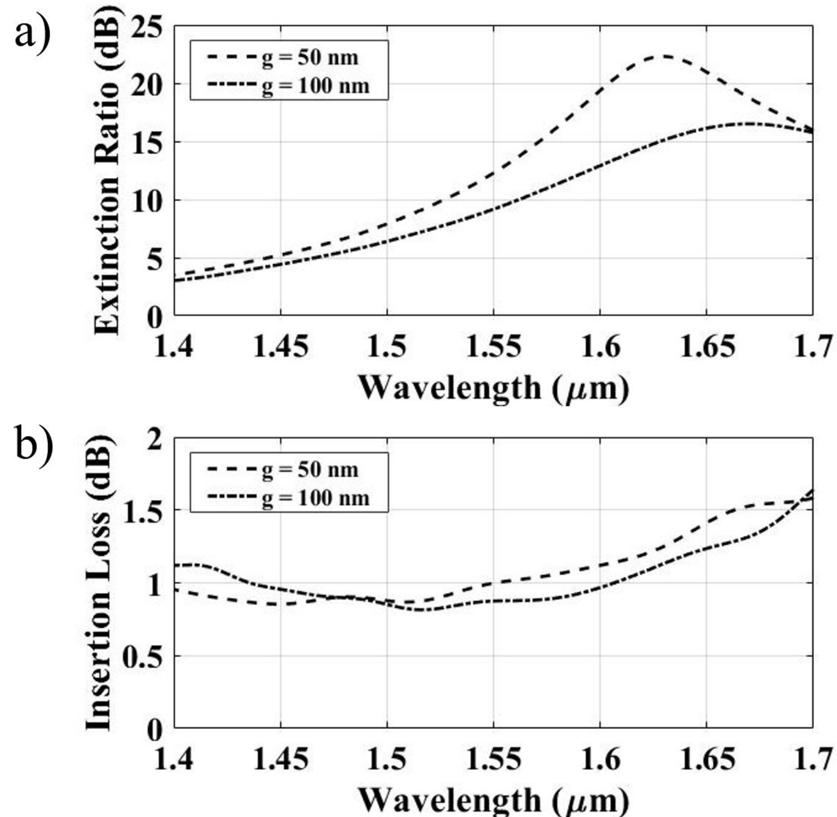

Fig. 5-5 (a) The ER and (b) IL achieved by the proposed device over a wideband of operation for a separation gap of 100 nm and 50 nm.

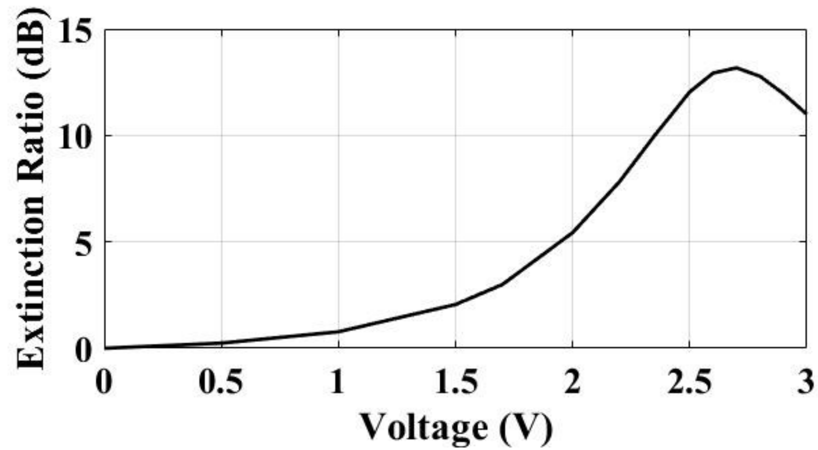

Fig. 5-6 The ER obtained from the ITO-integrated EOM for different values of gating potentials ranging from 0 V to 3 V.

An intensive electrostatic study of the device is held using an FEM-based commercial simulation tool [89]. In Fig. 5-7, the electrostatic contour lines across a cross-section of the coupler arm waveguide at an applied external potential of 2.35 V are shown.

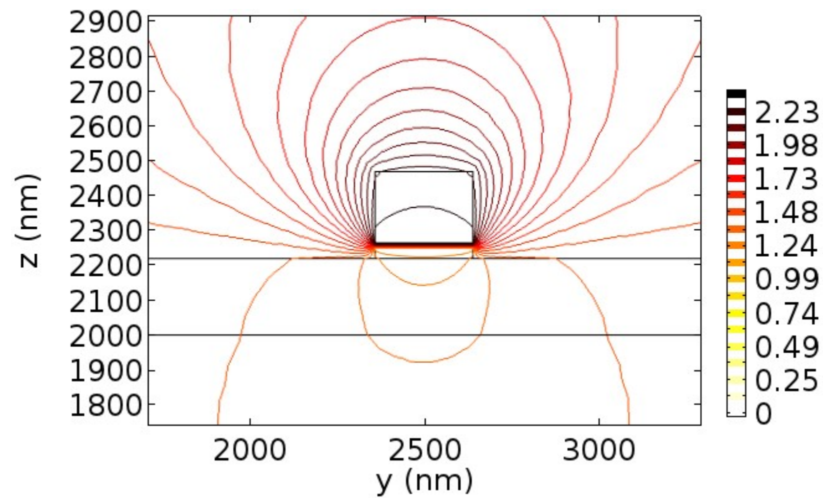

Fig. 5-7 The electrostatic contour lines across a cross-section of the coupler arm waveguide at a gating voltage of 2.35 V.

Regarding the modulation speed of the device, it is related to its resistance-capacitance (RC) product as in (5.2) [36], [38], [39]. The accumulation process of the free carriers inside the ITO happens almost instantaneously, much faster than the RC limit of the device [71]; therefore, it is safe to mention that the speed of the device depends solely on the RC component. Moreover, the average energy consumption of the device per bit is expressed in (5.3). It is function of the total capacitance of the device as well as the applied voltage.

$$f_{\max} = \frac{1}{2\pi RC} \tag{5.2}$$

$$E_{avg} = \frac{1}{2}CV^{2} \tag{5.3}$$

Using the same FEM-based simulation tool [89], the capacitance of the device is found to be around 1.57 fF. This infinitesimal capacitance yields an average energy consumption of 4.355 fJ/bit. For the internal resistance estimation, a conservative value of 500 Ω is assumed taking into consideration the resistivities imposed by the wiring in the system as well as the contacts. For these values of the resistance and capacitance, a speed of up to 200 GHz could be attained. If the quality of the system is enhanced so that the internal resistance could reach a value of 100 Ω, the ITO-based EOM would reach a speed of up to 1 THz under optimal conditions. In Table IV, a summary of the most important performance parameters of the proposed device are stated compared to those of other ITO-integrated EOM based on directional coupler devices.

Table IV A comparison between the parameters achieved by our proposed design vs. other ITO-integrated modulators based on directional coupler devices.

ER *dB*	IL *dB*	E *fJ/bit*	f_{max} *Tbits/s*	λ *μm*	L *μm*	V_g *V*	Ref.
6.7 2.3	0.032 0.036	78.9	0.116	1.31 1.55	17.6 6.6	2.4	[38]
5	0.87	330	0.257	1.55	5.6	2.3	[36]
6.14 11.4	0.06 1.65	67.1 22.7	0.0475 0.14	1.55	21 34	2.35	[39]
9.14	**0.86**	**4.35**	**1**	**1.55**	**5**	**2.35**	**-**

5.4 CONCLUSION

In this chapter, the ENZ characteristic of the ITO are utilized in designing an EOM based on a directional coupler device. The modulator operates at two distinct states, namely the “On” state and the “Off” state. At the “On” state, there is no applied voltage on the device; therefore, the ITO film acts as a conventional dielectric material. Most of the power is confined inside the slot SiO_2 layer, and minimal coupling losses are achieved by matching the effective refractive indices of the propagating modes inside the access waveguide and the coupler arm waveguide. On the other hand, at the “Off” state, a gating potential of

2.35 V is applied on the device leading to a high concentration of free carriers at the ITO/HfO_2 interface. The mode, in this case, is very lossy and leads to the decay of most of the power in the coupler arm waveguide. At the 1550 nm wavelength, an IL of about 0.86 dB as well as an ER of 9 dB are attained. The modulator can accommodate speeds up to 1 THz under optimal conditions and enhanced system. The average energy consumption per bit of the device is 4.355 fJ.

Chapter Six

6 LINEARIZED FEM SOLUTION OF THE ION-EXCHANGE NONLINEAR DIFFUSION MODEL

Ion exchange process is one of the most common techniques used in glass waveguides fabrication. This returns to many advantages such as low cost, ease of implementation and simple equipment requirements. The technology is based on the substitution of some of the host ions in the glass (typically Na^+) with other ions that possess different characteristics in terms of size and polarizability. The newly diffused ions produce a region with a relatively higher refractive index in which the light could be guided. A critical issue arises when it comes to designing such waveguides, that is carefully and precisely determining the resultant index profile. This task has been proven to be hideous as the process is generally governed by a nonlinear diffusion model with no direct general analytical solution. Furthermore, numerical solutions become unreliable – in terms of stability and mean squared error – in some cases, especially the K^+–Na^+ ion-exchanged waveguide, which is the best candidate to produce waveguides with refractive index differences compatible with those of the commercially-available optical fibers. Novel linearized finite element method formulations were used to provide a reliable tool that could solve the nonlinear diffusion model of the ion exchange in both one- and two-dimensional spaces. Additionally, the annealed channel waveguide case has been studied. In all cases, unprecedented stability and minimum mean squared error could be achieved.

6.1 INTRODUCTION TO THE PROBLEM

Ion exchange technique in glass substrates is a very ancient process [90]. The Egyptians are believed to have used this technique in coloring pots and decorating dishes back in the sixth century. Furthermore, with the spread of the Islamic culture, the usage of ion exchange to decorate glass has diffused throughout the Mediterranean basin. However, it was not until the 1960s that the ion exchange process has been used in an industrial application – glass strengthening [91], [92].

Shortly after the introduction of the integrated optics concept to the scientific community, Izawa and Nakagome [93] successfully produced the first ion-exchanged waveguide in

1972 by using a Tl^+ melt to substitute the originally-existent Na^+ ions in glass. The different size and polarizability of the Tl^+ ions compared to the Na^+ ions result in a change in the refractive index beneath the glass surface. This area could act as a waveguide core in which the light would be guided due to its relatively higher refractive index than its surrounding cladding region. A year later, Giallorenzi *et al* [94] produced Ag^+–Na^+ ion-exchanged waveguides.

Since these contributions, ion-exchanged waveguides have been intensively used in many integrated optics-related applications [95]–[100]. Moreover, several reviews [101]–[106], in which this technology has been studied, were published. This newly adopted technology had a huge potential due to the high compatibility, low cost and low propagation losses of the glass waveguides. On the other hand, the ion exchange process is an easy fabrication technique and it requires simple manufacturing equipment.

One challenge that faces the designers of ion-exchanged waveguides is lacking a reliable tool that could precisely predict the physical parameters involved in the process. In general, the ion exchange model is governed by a nonlinear diffusion equation [107], [108], [108]–[112] that has no general analytical solution.

In previous work [113], we have introduced a solution to the nonlinear diffusion model of the ion exchange process based on finite element method formulations with unprecedented stability and minimum mean squared error. In this chapter, we further extend our solution to involve two-dimensional (2D) spaced problems as well as the annealed channel waveguide case.

6.2 ION EXCHANGE PROCESS MODELING

Since the incoming exchanged ions need to diffuse into the glass substrate occupying their suitable sites of the host glass network, the ion exchange process can be considered as a double-diffusion process. For simplicity, only the thermally driven waveguides are discussed. Thus, any effect of applied external field is neglected. Applying the Nernst-Einstein equation [105] for ionic conductivity, we have

$$j_1 = -D_1 \nabla c_1 + \left(c_1 D_1 q / fkT \right) E \tag{4.1}$$

$$j_2 = -D_2 \nabla c_2 + \left(c_2 D_2 q / fkT \right) E$$

Here, "1" and "2" are used to label the exchanging ions and the original ions, respectively. c_i, D_i and j_i are the concentration, the diffusion coefficient and the number flux of ions of species i, respectively. Furthermore, q is the proton charge, k is Boltzmann's constant, E is the total electric field (the sum of any external applied field and the internal field due to unequal ion mobilities of the exchanging ions and the original ones). Finally, f is a correlation factor that relates to the Haven ratio [114] and account for the failure of the Nernst-Einstein relation in predicting the diffusion coefficient value in real glasses [101].

For meeting the local charge neutrality condition, $c_1 + c_2$ must be equal to c_0, the total concentration of the mobile atoms in the glass. This implies a new constraint as c_0 is always constant [105].

$$\nabla c_1 + \nabla c_2 = 0 \tag{4.2}$$

After the continuity equation is applied

$$\frac{\partial c_1}{\partial t} + \nabla \cdot \vec{j_1} = 0 \tag{4.3}$$

this leaves us with the final general form of the ion exchange process model mainly governed by a nonlinear diffusion relation as follows [105], [115]

$$\frac{\partial C}{\partial t} = \frac{D}{1 - \alpha C} \left[\nabla^2 C + \frac{\alpha \left(\nabla C \right)^2}{1 - \alpha C} - \frac{q E_{ext}}{kT} \nabla C \right] \tag{4.4}$$

where $C = c_1 / c_0$ is the normalized concentration of the exchanged ions, and we have relabeled D_1 as D which is the diffusion coefficient of the exchanged species, $\alpha = 1 - D_1 / D_2$ is the Stewart coefficient [116] relating the diffusion coefficients of the two ionic species and ∇ is the differential operator. E_{ext} is the external applied field, and as previously stated, this is assumed to be absent (i.e $E_{ext} = 0$). This reduces (4.4) into the following

$$\frac{\partial C}{\partial t} = \frac{D}{1 - \alpha C} \left[\nabla^2 C + \frac{\alpha \left(\nabla C \right)^2}{1 - \alpha C} \right] \tag{4.5}$$

Now, (4.5) can be rewritten in a more common form [110], [112] as follows

$$\frac{\partial C}{\partial t} = \nabla \cdot \left(\frac{D}{1-\alpha C} \nabla C \right) \tag{4.6}$$

In this chapter, we specifically focus on an interesting ionic pair, which is the K^+/Na^+ exchanged waveguide. This specific model is used in fabricating integrated optical devices with refractive index differences compatible with those of the optical fibers as well as providing low losses. However, in this case, the value of the Stewart coefficient α approaches unity [112], and numerical instabilities may occur when trying to solve for the exchanged ions concentration.

To overcome these stability problem, different novel linearized Finite Element Method (FEM) techniques are proposed in both one-dimensional (1D) [113] and two-dimensional (2D) spaces. The stability and accuracy of the different methods outperforms the current numerical methods and provide a good tool for highly nonlinear diffusion problem, in general.

6.3 LINEARIZED FINITE ELEMENT METHOD FORMULATIONS

The first step towards the solution is introducing a new slack variable Z [112], [113], such that

$$dZ = \tilde{I} \tag{4.7}$$

where $\tilde{I}$ $/(1-\alpha C)$. By substituting (4.7) into the original equation expressed in (4.6), we can reach a simpler linear equation instead of the nonlinear model as follows

$$\frac{\partial C}{\partial t} = \nabla^2 \cdot Z \tag{4.8}$$

Applying the piecewise linear function finite element method scheme to (4.8) as in Ref. [113], we get

$$MC^{n+1} = \Delta t \left(F - KZ^{?} \right) + MC^{n} \tag{4.9}$$

where M and K are the global mass and stiffness matrices, respectively, and F is the global load vector. C^n is the normalized concentration of the exchanged ions at the current time step n , C^{n+1} is the normalized concentration of the exchanged ions at the next time step $n+1$, and Δt is the time step size. Note that a question mark '?' is used

as a superscript for Z because it is still not determined at what time step we should include it in the expression. According to whether Z^n or Z^{n+1} is used in Eq. (4.9), different solutions are introduced.

However, before proceeding further in solving the problem, a direct relation between C and Z are needed to be established. From Eq. (4.7), it can be deduced that

$$Z = -\frac{D}{\alpha}\ln\left(1-\alpha C\right) \tag{4.10}$$

6.3.1 Forward-time Technique

The simplest, fastest and most direct solution is the forward-time (FT) technique, where Z^n is used in Eq. (4.9) instead of $Z^?$. This yields the following reproduction of Eq. (4.9)

$$MC^{n+1} = \Delta t\left(F - KZ^n\right) + MC^n \tag{4.11}$$

In this case, we can express the system as a simple matrix problem as follows

$$MC^{n+1} = F_{eff} \tag{4.12}$$

where F_{eff} is the effective global load vector, and $F_{eff} = \Delta t\left(F - KZ^n\right) + MC^n$. Now, by using matrix inversion method, we can easily solve for C^{n+1} at each time iteration starting with the initial condition at t_0. The boundary conditions are applied at each time step. The respective values of Z^n at each time iteration are computed using the direct $C-Z$ relation in (4.10).

6.3.2 Backward-time Technique

Another solution is concluded when using Z^{n+1} in (4.9). This technique is called the backward-time (BT), and we get

$$MC^{n+1} = \Delta t\left(F - KZ^{n+1}\right) + MC^n \tag{4.13}$$

It is obvious that this approach is not as simple as the FT technique as we have both C^{n+1} and Z^{n+1} in the equation. To be able to solve this more complicated system, we have to separate the "$n+1$" terms in one side of the equation as well as get rid of the Z^{n+1} expression. One way for doing so is using the relation expressed in (4.7) as follows

$$\because \tag{4.14}$$

$$\therefore Z^{n+1} - Z^{n} = \tilde{I} \quad \cdots \quad ^{-1} - C^{n} \Big)$$

$$\therefore Z^{n+1} = Z^{n} + \tilde{I} \quad \cdots \quad ^{-1} - C^{n} \Big)$$

By substituting (4.14) into (4.13), we now reach a simpler expression that satisfies the previously mentioned conditions.

$$\Big[M + \Delta t K \tilde{I} \quad \cdots \tag{4.15}$$

Now we can easily express this system as follows

$$M_{eff} C^{n+1} = F_{eff} \tag{4.16}$$

where M_{eff} and F_{eff} are the effective global mass matrix and the load vector, respectively. $M_{eff} = M + \Delta t K \tilde{I} \quad \cdots$ and $F_{eff} = \Delta t \Big(F - KZ^{n} + K\tilde{I} \quad \cdots + MC^{n}$.

Now, (4.16) of the BT technique becomes similar to (4.12) of the FT technique with only slight change in the values of the global effective mass matrix and effective load vector. The same solution steps of the FT technique can be repeated here to solve for C^{n+1} at each time iteration.

6.3.3 Crank Nicholson Technique

In another technique, which is the Crank-Nicholson (CN), a time average value of Z (i.e. $\left[Z^{n+1} + Z^{n} \right] / 2$) is used in (4.9), reaching the following solution

$$MC^{n+1} = \Delta t \left[F - \frac{1}{2} K \left(Z^{n+1} + Z^{n} \right) \right] + MC^{n} \tag{4.17}$$

Following the same procedure used in the BT technique to simplify the expression and get rid of the Z^{n+1} term, we can reach the following

$$\left[M + \frac{\Delta t}{2} K \tilde{I} \quad \cdots \tag{4.18}$$

Which is also can be expressed in a simple matrix-form equation as

$$M_{eff} C^{n+1} = F_{eff} \tag{4.19}$$

where $M_{eff} = M + \Delta t K\tilde{I}$ and $F_{eff} = \Delta t \left(F - KZ^{n} + K\tilde{I} \quad 2 \right) + MC^{n}$.

Now, the same solution steps of the previous two techniques can be applied to this technique as well. It should be mentioned here that the CN solution does not affect neither the time nor the size of the computation; however, it is supposed to offer more accuracy and higher stability to the solution.

Table V A summary of the values of the global mass matrices M_{eff} and load vectors F_{eff} of the three mentioned techniques FT, BT and CN.

	M_{eff}	F_{eff}
FT	M	$\Delta t \left(F - KZ^{n} \right) + MC^{n}$
BT	$M + \Delta t K\tilde{I}$	$\Delta t \left(F - KZ^{n} + K\tilde{I} \right. + MC^{n}$
CN	$M + \Delta t K\tilde{I}$	$\Delta t \left(F - KZ^{n} + K\tilde{I} \quad 2 \right) + MC^{n}$

In Table V, we sum up the different values of M_{eff} and F_{eff} for the three techniques. Additionally, Fig. 6-1 shows a simple flowchart of the solution process used in the three techniques.

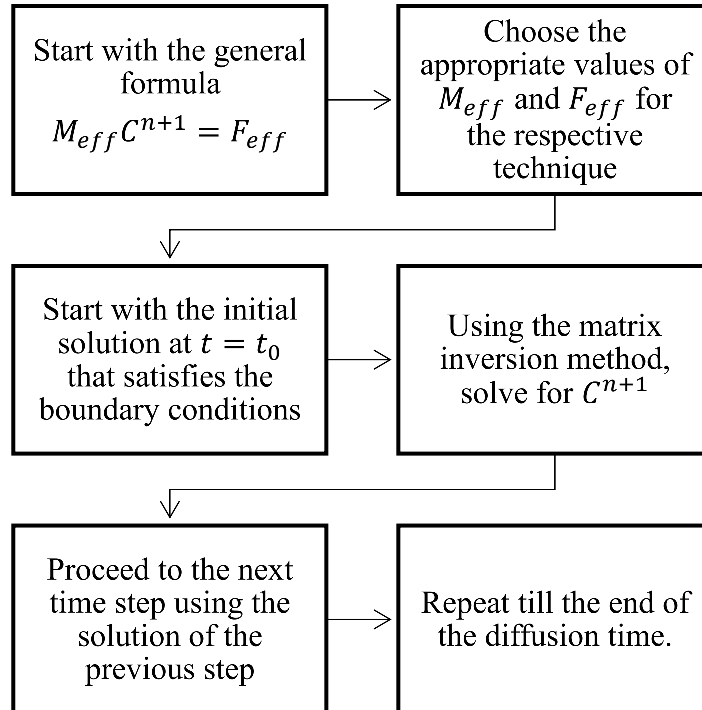

Fig. 6-1 A simple flowchart of the solution process.

6.4 RESULTS AND DISCUSSION

The above-mentioned techniques are applied to the nonlinear diffusion model of the ion exchange process with different values of α, constant diffusion coefficient $D = 0.0186\ \mu m^2/min$, constant diffusion time $T = 1800\ min$, constant step time $\Delta t = 0.1\ min$ and step size $\Delta x = 0.5\ \mu m$. The results for the 1D forward-time, backward-time and Crank-Nicholson techniques were discussed in previous work [113]. In Table VI, a mean squared error for every technique is calculated compared to the numerical solutions obtained through a commercially-available FEM-based tool – COMSOL Multiphysics [89].

Table VI The mean squared error of the three techniques (FT, BT and CN) compared to the numerical solution obtained by an FEM-based commercially-available tool – COMSOL Multiphysics.

The Stewart coefficient α		**0.9**	**0.95**	**0.98**	**0.9999**
Mean squared error	Forward-time technique	3.8144e-06	1.2887e-06	Not stable	Not stable
	Backward-time technique	3.8216e-06	1.2923e-06	3.9943e-06	1.8488e-05
	Crank-Nicholson technique	3.8178e-06	1.2903e-06	3.9836e-06	1.9244e-05

The forward-time technique failed to solve the previous problem of numerical instabilities at near-unity values of α. Unstable solutions were obtained at nearly $\alpha = 0.98$. Fortunately, both the backward-time and Crank-Nicholson techniques could successfully overcome the aforementioned instability problem, and stable results were produced at values of α as large as 0.9999. It is obvious that this novel approach, which is based on the finite element method, provides unprecedented stability to the solution of the ion exchange process model.

In this chapter, we further extend our studies by using both the BT and CN techniques to solve the 2D version of the nonlinear diffusion model. The same stability conditions could be reached and the results are shown in Fig. 6-2 and Fig. 6-3.

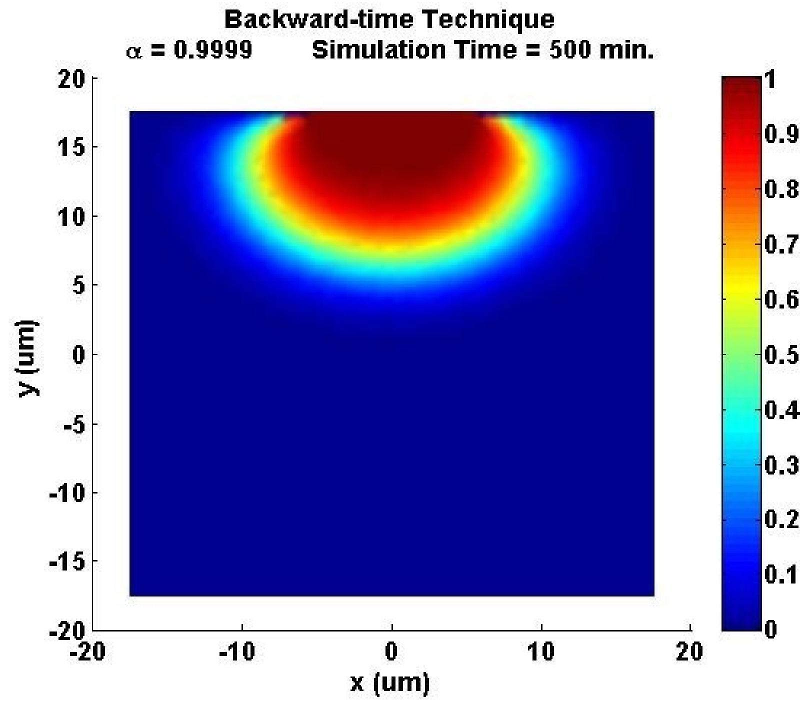

Fig. 6-2 2D BT technique normalized concentration map at $\alpha = 0.9999$, diffusion coefficient $D = 0.0186\ \mu m^2/min$, constant diffusion time $T = 500\ min$ and constant step size $\Delta t = 0.1\ min$ and $\Delta x = \Delta y = 0.875\ \mu m$.

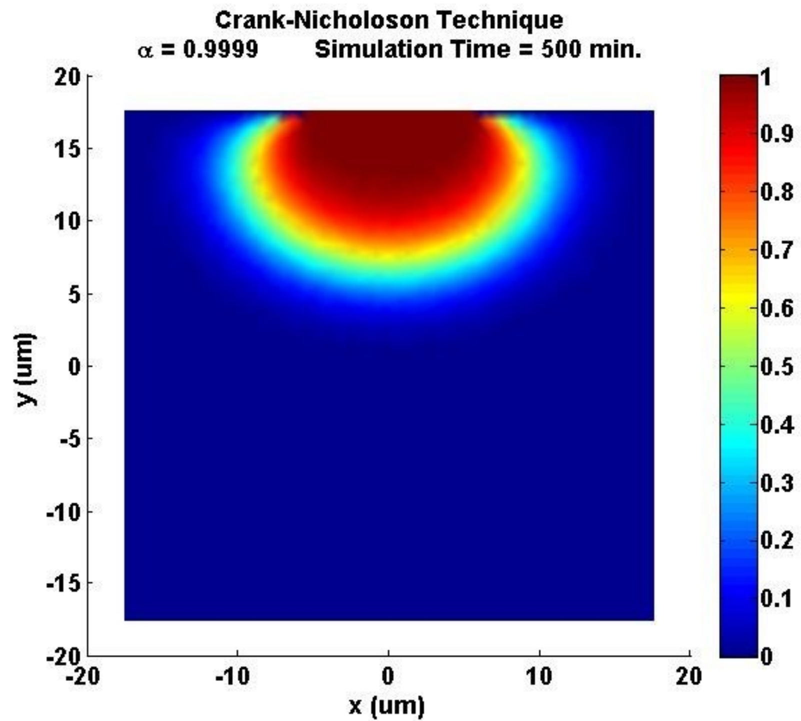

Fig. 6-3 2D CN technique normalized concentration map at $\alpha = 0.9999$, diffusion coefficient $D = 0.0186\ \mu m^2/min$, constant diffusion time $T = 500\ min$ and constant step size $\Delta t = 0.1\ min$ and $\Delta x = \Delta y = 0.875\ \mu m$.

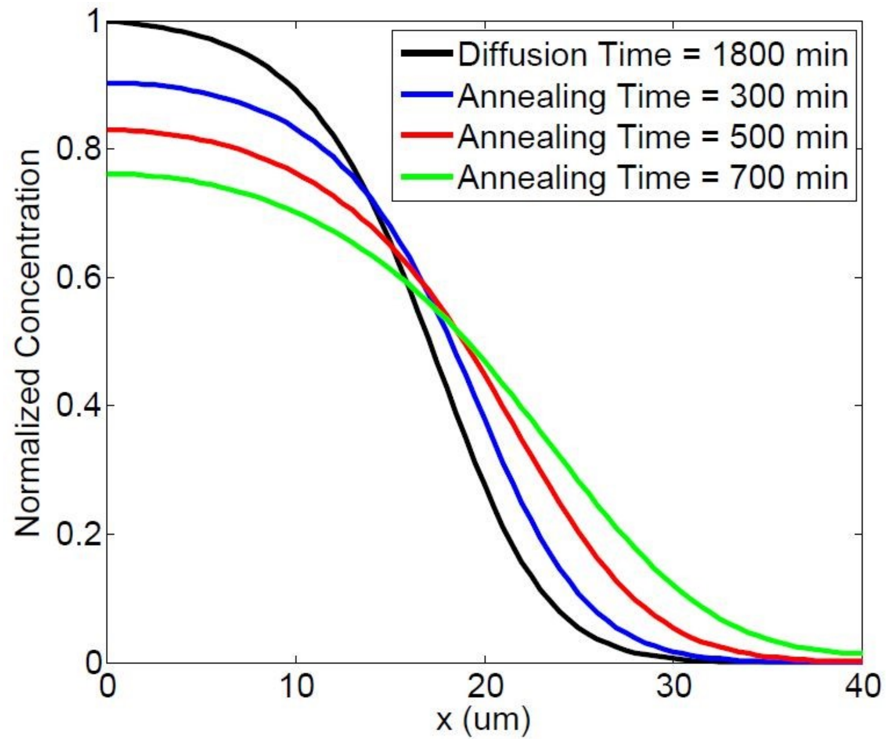

Fig. 6-4 1D backward-time technique normalized concentration profile at $\alpha = 0.99$, normal diffusion time 1800 min, and total annealing time 700 min. The normalized concentrations after 300 min and 500 min of annealing are also illustrated.

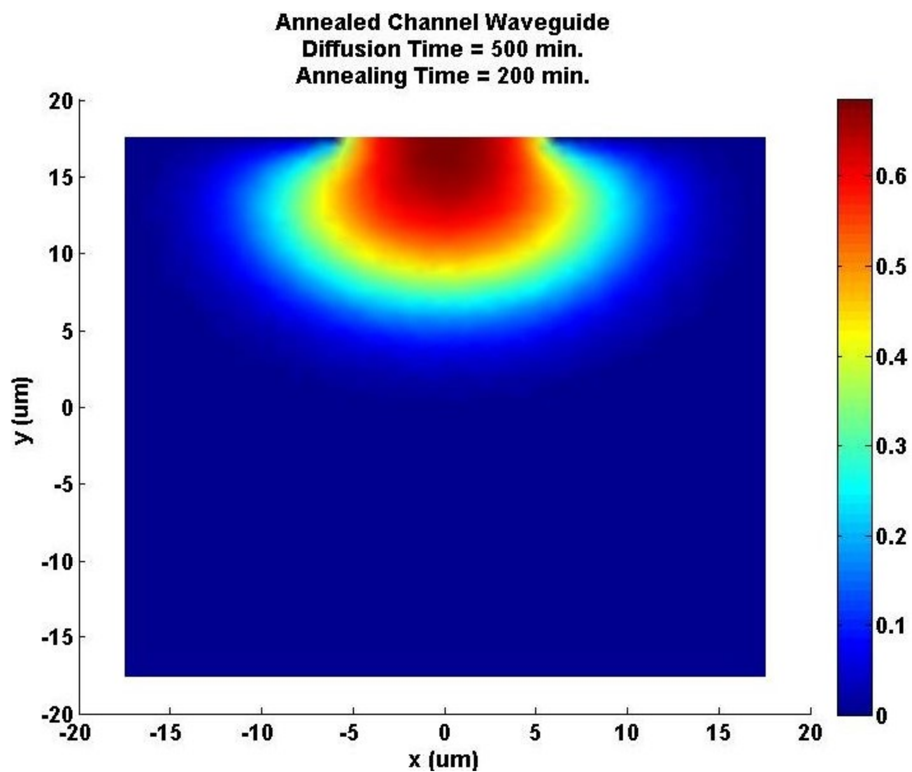

Fig. 6-5 2D backward-time technique normalized concentration map at $\boldsymbol{\alpha = 0.99}$. A total diffusion time of $\mathbf{500\ min}$ is followed by an annealing time of $\mathbf{200\ min}$, diffusion coefficient $\boldsymbol{D = 0.0186\ \mu m^2/min}$ and constant step size $\boldsymbol{\Delta t = 0.1\ min}$ and $\boldsymbol{\Delta x = \Delta y = 0.875\ \mu m}$.

For further verification, the annealed channel waveguide case was studied. Here, the ion exchange process is stopped after a certain time of diffusion. Hence, the initial condition of every time step becomes the result of the preceding one without imposing the boundary conditions repeatedly. This decreases the mismatch losses compared to the surface waveguide case which is previously discussed. Fig. 6-4 shows the results obtained through the backward-time technique at $\alpha = 0.99$ for an annealing time of 700 min preceded by 1800 min of diffusion time. The 2D case is shown in Fig. 6-5. A total diffusion time of 500 min is followed by an annealing duration of 200 min.

6.5 CONCLUSION

Different novel finite element method techniques are used in solving the nonlinear diffusion model of the ion exchange process for glass waveguides in both one- and two-dimensional spaces. Unprecedented very highly stable solutions are presented, with the Stewart coefficient α reaching as large values as 0.9999 for both surface waveguide and annealed channel waveguide. Moreover, minimum mean squared errors [113] are achieved compared to any reported previous work [112].

Chapter Seven

7 SILICON PHOTONICS FABRICATION AND CHARACTERIZATION EFFORTS

In the previous chapter, we introduced a computational-based solution for fabrication-related challenge. A linearized model based on finite element method formulation is proposed to solve an instability problem that arises when solving the 2nd order nonlinear diffusion expression of ion exchange waveguides. In this chapter, we introduce our efforts in developing different fabrication techniques for different silicon photonics applications. The chapter includes a main section: silicon and silicon dioxide growth, photolithography and etching for standard SOI technologies fit for near-infrared applications.

7.1 MASK LAYOUT

For the design of the mask, we have included some basic components for generic photonic applications. The components include 90° bends, 180° bends, straight waveguides, and directional couplers. In Fig. 7-1, an overall broad view of the layout of different mask components is shown, while closer views of the same components are depicted in Fig. 7-2. A very close-up view of a directional coupler of the fabricated mask is shown in

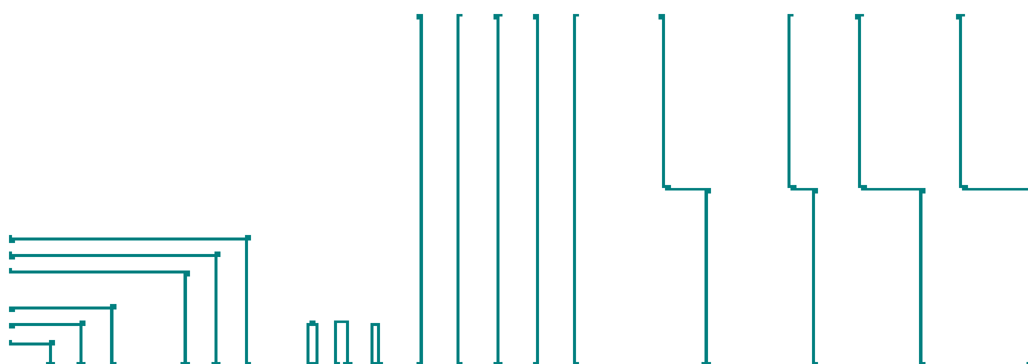

Fig. 7-1 A broad view of the different components included in the mask layout. The components are (from left to right): 90° bends, 180° bends, straight waveguides, and directional couplers.

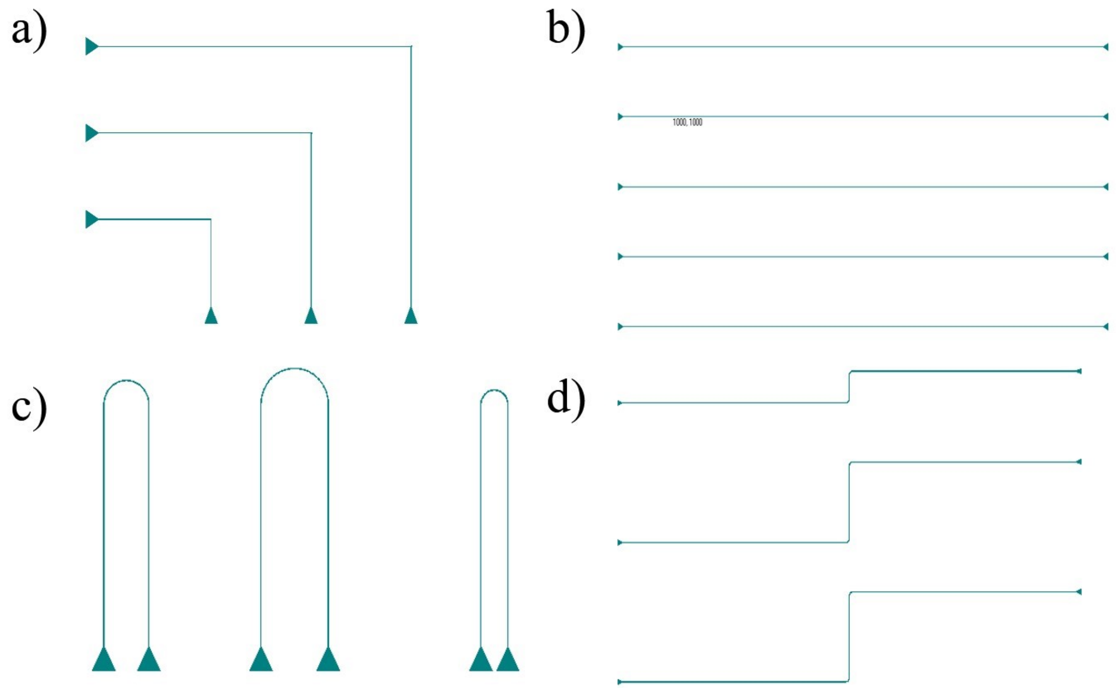

Fig. 7-2 Closer views of the different components of the mask. (a) 90º bends, (b) straight waveguides, (c) 180º bends, and (d) directional couplers.

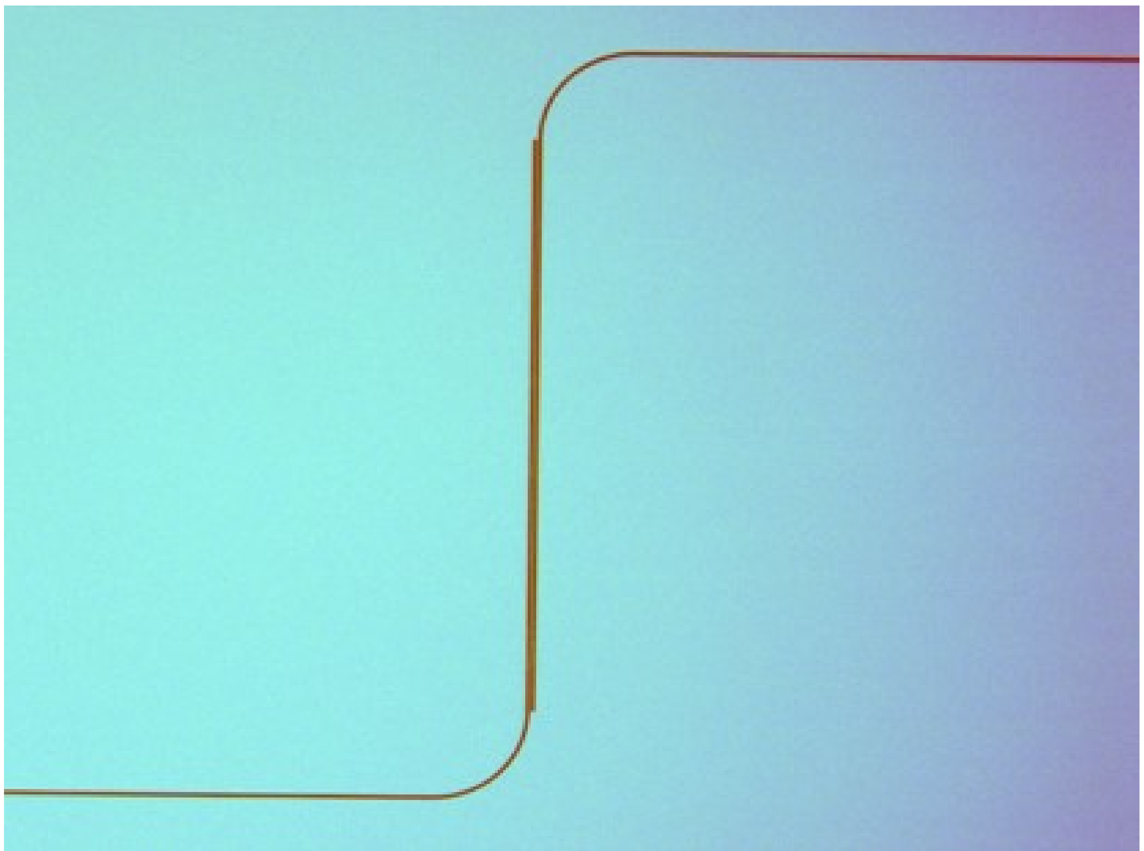

Fig. 7-3 A very close-up view of a directional coupler of the fabricated mask. Two 90º bends along the directional coupler are shown.

7.2 FABRICATION SEQUENCE

Regardless of the waveguide intended to be fabricated, the following generic steps are followed:

- Cleaning the wafer with acetone, isopropyl alcohol (IPA) and deionized (DI) water.
- Depositing the device layer using a plasma-enhanced chemical vapor deposition (PE-CVD).
- Depositing the photoresist.
- Ultraviolet (UV) exposure through the mask.
- Deep reactive ion etching (DRIE) using inductively coupled plasma (ICP).
- Photoresist removal.

7.3 SILICON-ON-INSULATOR

In this section, we discuss the efforts made in synthesizing silicon-on-insulator (SOI) waveguides for near-infrared applications. We start with a standard N-type 111 Si wafer provided from University Wafer [117]. First, the wafer is cleaned intensively with acetone, IPA and DI water. After that, it is dried by the means of N_2 gas. The wafer is then ready for entering the PE-CVD for SiO_2 and Si deposition. The required thickness of the SiO_2 layer is intended to be more than 1 micron. At a temperature of 350°C, pressure of 1.6 torr and RF power of 140 W, the following gases are flowed into the chamber with the following standard cubic centimeter per minute (sccm) for 40 minutes: SiH_4 (20 sccm), N_2O (1500 sccm), and N_2 (980 sccm). Table VII includes a summary of all the parameters of the SiO_2 deposition recipe. In Fig. 7-4, an SEM image is taken at the cross-section of the wafer after the deposition of SiO_2 and Si. The thickness of the SiO_2 layer is found to be around 1.25 microns, which match the desired thickness of more than 1 micron.

Table VII A summary of the recipe's parameters for SiO_2 deposition

PARAMETER	VALUE	UNIT
SIH_4	20	sccm
N_2O	1500	sccm
N_2	980	sccm
PRESSURE	1.6	torr
RF POWER	140	W
TEMPERATURE	350	ºC
TIME	40	minutes

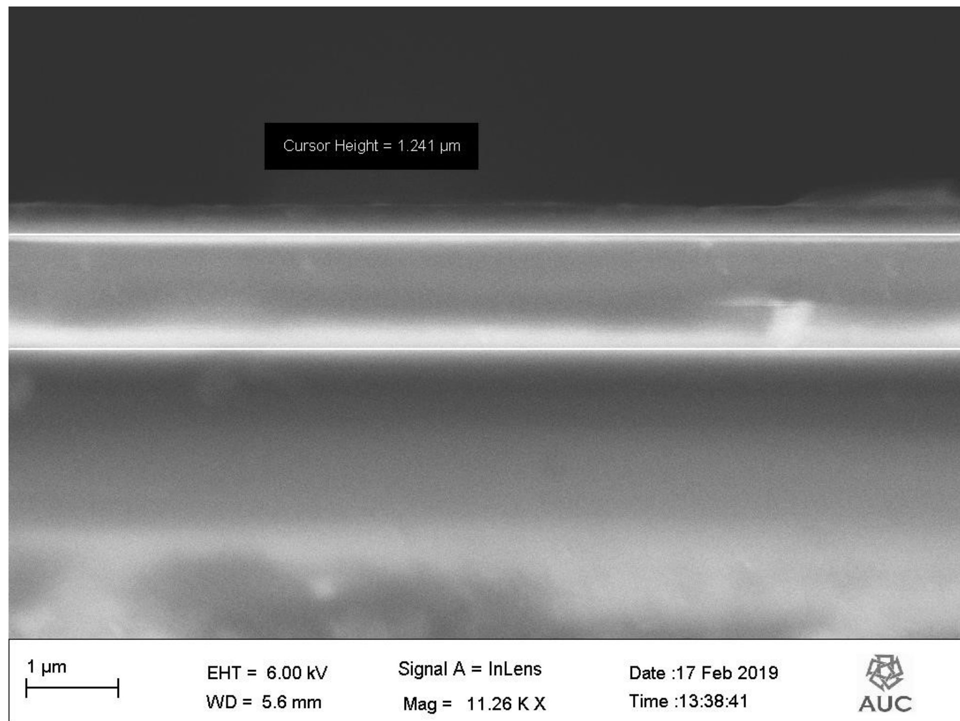

Fig. 7-4 A cross-sectional SEM image taken after the deposition of the SiO_2 and Si layers. The thickness of the SiO_2 layer is depicted in the image.

After the deposition of the SiO_2 layer, the wafer once again enters the PE-CVD for Si deposition. The required thickness is estimated to be around 300 nm for good mode confinement inside the core of the waveguide. Now, at a temperature of 350ºC, pressure

of 1.8 torr, and RF power of 75 W, SiH_4 and He gases are flowed inside the chamber at 20 sccm and 980 sccm, respectively, for a time of 1 hour. A summary of the recipe's parameters is given in Table VIII, while an SEM image of the wafer is shown in Fig. 7-5.

Table VIII A summary of the recipe's parameters for Si deposition

PARAMETER	VALUE	UNIT
SIH_4	20	sccm
HE	980	sccm
PRESSURE	1.8	torr
RF POWER	75	W
TEMPERATURE	350	ºC
TIME	60	minutes

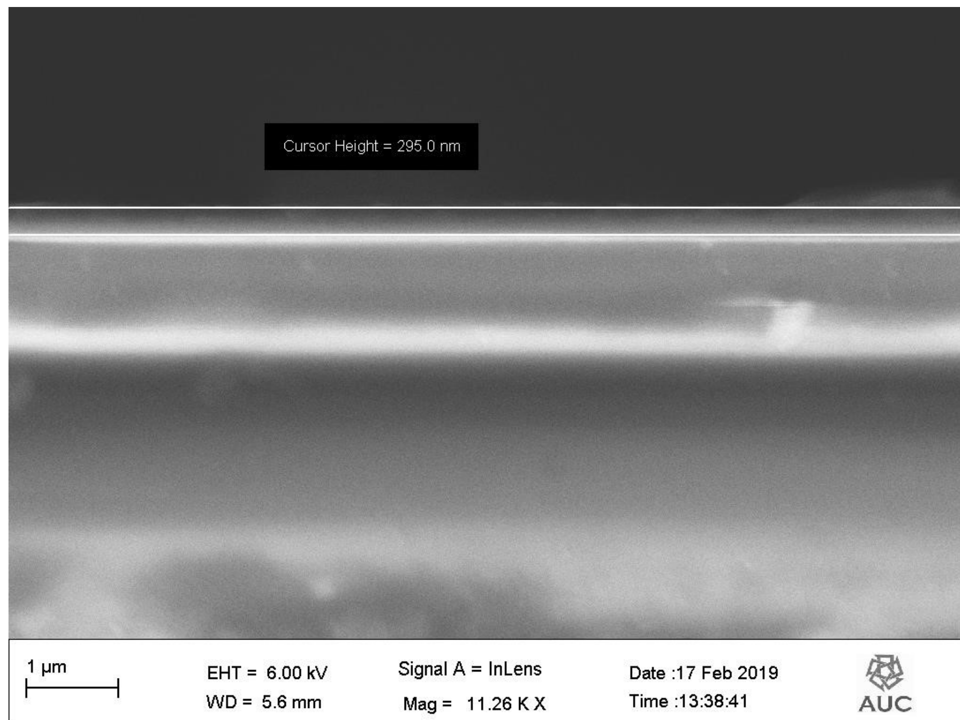

Fig. 7-5 A cross-sectional SEM image taken after the deposition of the SiO_2 and Si layers. The thickness of the Si layer is depicted in the image.

After the deposition of both the SiO_2 and Si layers, the wafer is prepared for the photolithography procedure. First, the wafer is prebaked at a temperature of 150ºC for

about 10 minutes. This step is essential for the removal of the absorbed water on the surface of the silicon when exposed to the air humidity [118]. In order to make the surface of the substrate hydrophobic (i.e. water-repellent and thus photoresist-attractive), the wafer is treated with Hexamethyldisilazane (HMDS), a non-polar adhesion promoter. This step is considered a common method to enhance the adhesion of the photoresist to the wafer. After that, the wafer is baked again at a temperature of 120ºC for about 2 minutes to initiate the chemical bonding of HMDS to the substrate surface, before depositing the photoresist and spin coating it at a velocity of 4000 rounds per minute (RPM). After the deposition of the photoresist, a post-baking at a temperature of 100ºC for 50 seconds is performed. Next, a mask alignment device is used to expose the wafer to UV radiation for 30 seconds. After that, the exposed photoresist is removed by submerging the wafer in a DI water / AZ developer solution with 4:1 ratio for 3 minutes.

Now, the wafer has a deposited photoresist layer only at the unexposed parts to the UV light. Using a DRIE based on ICP, we can remove the 300 nm-thick silicon layer that was previously exposed to the UV radiation. At a temperature of 10ºC, a pressure of 15 mtorr, an RF power of 30 W and ICP power of 1200 W, C_4F_8 and SF_6 gases are flowed by a rate of 40 sccm and 20 sccm, respectively. The etch rate at these conditions is estimated to be around 100 nm per minute. Therefore, a recipe time of about 3 minutes is required to etch the 300 nm Si layer. A summary of the parameters of the recipe is given in Table IX.

Table IX A summary of the recipe's parameters for Si etching at a rate of 100 nm/min.

PARAMETER	VALUE	UNIT
C_4F_8	40	sccm
SF_6	20	sccm
PRESSURE	15	mtorr
RF POWER	30	W
ICP POWER	1200	W
TEMPERATURE	10	ºC
TIME	3	minutes

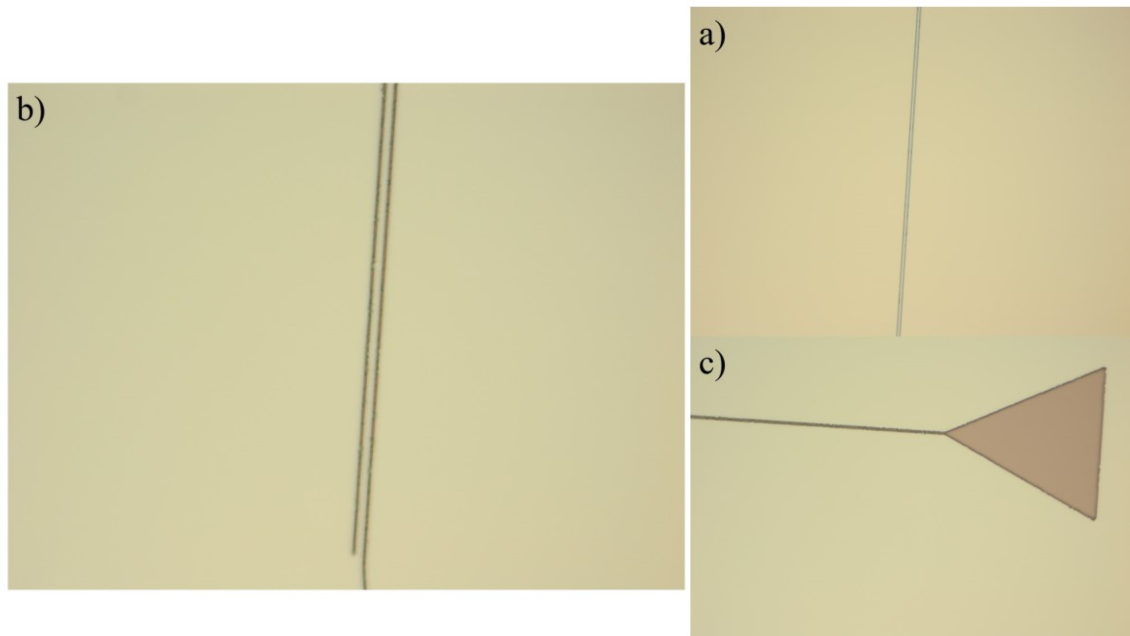

Fig. 7-6 Optical microscope images of some of the fabricated components: (a) directional coupler, (b) a close-up view of a directional coupler, and (c) input/output tapered waveguide.

7.4 CONCLUSION

In this chapter, our efforts in fabricating and characterizing silicon-on-insulator (SOI) waveguides for near-infrared applications are reviewed. Starting with a conventional N-type Si wafer, an oxide layer is deposited using a PE-CVD. After that, the Si device layer is deposited as well. A photolithography process using a mask with generic optical components is performed. Finally, using an ICP-DRIE device, the top Si layer is etched according to the mask features. Optical microscope images of some components are shown above.

This work is considered a step towards a final realization of the designs proposed in chapters 4 and 5. An efficient coupling technique to/from the chip is needed. For example, grating couplers or deep trenches for edge fiber coupling are among some examples that can be used to couple light into and out from the structures. An efficient strip-to-slot waveguide converter can also be implemented in order to reduce the losses. Further steps of deposition, photolithography and etching are performed when needed according to the architectures of the devices.

C h a p t e r   E i g h t

8 CONCLUSION AND FUTURE WORK

Driven by the huge increase in information data over the past two decades, the traditional CMOS technologies, which are the bases for most of the existent electronic devices, have been pushed towards their physical limits. Since the 1970s, optical fiber industry has been proven successful in large-scale communications as they constitute the intercontinental internet network. They offer higher data rates, more network capacities, and more security. However, the constant increasing need for a larger number of components on the chip and higher clock frequencies have added more layers of chip complexity. All of these factors have stimulated an urge need for integrating optical components along their electronic counterparts in the same application specific electronic and photonic integrated circuit (ASEPIC).

Silicon photonics industry has gained a lot of attention since its emergence for its factory-compatibility with the CMOS foundries across the globe. The most promising applications of this technology is biosensing and telecommunications. An integrated on-chip optical communication system includes many components such as lasers, photodetectors, multiplexers, switches, filters, resonators, optical interconnects, splitters, combiners and junctions. However, the most crucial component of the system is the optical modulator as it takes in the digital electronic data and carries them on a continuous light beam. In other words, it modulates one of the physical properties of the light (i.e. amplitude, phase, or wavelength) according to the input electronic digital data (i.e. ones and zeros).

Any optical modulator has three key characteristics, which determine its performance: (1) the modulation scheme, (2) the device's geometrical structure, and (3) the electro-optic active medium, which is responsible for the modulation effect in the device. Compared to acousto-optic and thermo-optic modulation, electro-optic modulation is the most commonly used form of optical modulation in the field. This class of modulators depends on the alteration of the optical properties of the active material in response to an applied voltage. Many electro-optic devices were proposed recently based on a number of different structures. The most commonly used structures in optical modulators are Mach-

Zehnder interferometers, multimode interferometers, electro-absorption modulators, subwavelength grating waveguides, directional couplers and ring resonators.

Unfortunately, intrinsic silicon exhibits weak electro-optic effects; therefore, it would require very large modulators to achieve proper performance. This size mismatch between the photonic components and their electronic counterparts would render the task of their integration on one chip a hideous task. Towards miniature optical modulator devices, the scientific community has directed its attention to a new class of modes, which is surface plasmon polaritons (SPPs). They propagate along a metal-dielectric interface localizing the field in subwavelength dimensions, which overcome the 'diffraction limit'. However, the presence of metals in the devices introduce large insertion losses.

The utilization of transparent conducting oxides (TCOs), especially indium tin oxide (ITO), in optical modulators has gained a great attention recently for their exotic characteristics. They are invisible to light at most of the spectrum, while having high electric conductivity and an excess of free carriers. By electrically tuning the ITO, the concentration of free carriers can greatly increase at an ITO/dielectric interface forming SPP modes. Consequently, ITO can exhibit a metal-like behavior, but only under specific conditions; otherwise, it acts as a conventional dielectric material with low optical losses and high transmittance. At certain value of gating potential, ITO can reach an epsilon-near-zero (ENZ) state, where very large losses are introduced to the device.

In this thesis, we proposed two novel electro-optical modulator devices with the ITO acting as the active material. The first device is based on a ring resonator structure. An IL of 0.075 dB and an ER of 14 dB were achieved at a standard telecommunication wavelength of 1550 nm. The other device is based on a directional coupler structure, and an IL and ER of 0.86 dB and 9 dB, respectively, are attained. The ring resonator device achieves a better performance overall; however, it suffers from a narrow bandwidth of operation and deterioration in the performance with low fabrication or temperature tolerances. On the other hand, the directional coupler-based EOM achieves less performance, but it provides a larger bandwidth of operation and a great resistance to fabrication tolerances and temperature fluctuations.

In the future, we are planning to engage more in the fabrication and characterization processes of on-chip electro-optical modulators to extend the work presented here.

REFERENCES

[1] R. W. Burns, *Communications: an international history of the formative years*, vol. 32. IET, 2004.

[2] R. W. Burns, “Soemmering, Schilling, Cooke and Wheatstone, and the electric telegraph,” in *Papers Presented at the Sixteenth IEE Week-End Meeting on the History of Electrical Engineering*, 1989, pp. 70–79.

[3] G. E. Moore, “Cramming More Components Onto Integrated Circuits,” *Proc. IEEE*, vol. 86, no. 1, pp. 82–85, Jan. 1998, doi: 10.1109/JPROC.1998.658762.

[4] A. Chen and E. Murphy, Eds., *Broadband Optical Modulators: Science, Technology, and Applications*, 0 ed. CRC Press, 2016.

[5] “Cisco Global Cloud Index: Forecast and Methodology, 2016–2021 White Paper - Cisco.” [Online]. Available: https://www.cisco.com/c/en/us/solutions/collateral/service-provider/global-cloud-index-gci/white-paper-c11-738085.html. [Accessed: 25-Jul-2019].

[6] “Industry Data | NCTA — The Internet & Television Association.” [Online]. Available: https://www.ncta.com/industry-data. [Accessed: 25-Jul-2019].

[7] K. Billerbeck, *Electro-optic and photorefractive materials: proceedings of the international.* Place of publication not identified: Springer, 2012.

[8] P. Cheben, R. Soref, D. Lockwood, and G. Reed, Eds., *Silicon Photonics*, vol. Advances in Optical Technologies. Hindawi Publishing Corporation, 2008.

[9] Y. Kurosaka *et al.*, “On-chip beam-steering photonic-crystal lasers,” *Nat. Photonics*, vol. 4, no. 7, pp. 447–450, Jul. 2010, doi: 10.1038/nphoton.2010.118.

[10] M. Feng *et al.*, “On-chip integration of GaN-based laser, modulator, and photodetector grown on Si,” *IEEE J. Sel. Top. Quantum Electron.*, vol. 24, no. 6, pp. 1–5, 2018.

[11] P. Dong, “Silicon photonic integrated circuits for wavelength-division multiplexing applications,” *IEEE J. Sel. Top. Quantum Electron.*, vol. 22, no. 6, pp. 370–378, 2016.

[12] A. Liu *et al.*, “Wavelength division multiplexing based photonic integrated circuits on silicon-on-insulator platform,” *IEEE J. Sel. Top. Quantum Electron.*, vol. 16, no. 1, pp. 23–32, 2009.

[13] Z. Wang, M. Ma, and L. R. Chen, “Integrated optical add-drop multiplexer in SOI based on mode selection and Bragg reflection,” *IEEE Photonics Technol. Lett.*, vol. 30, no. 24, pp. 2107–2110, 2018.

[14] L.-W. Luo *et al.*, “WDM-compatible mode-division multiplexing on a silicon chip,” *Nat. Commun.*, vol. 5, p. 3069, 2014.

[15] L. Han, S. Liang, J. Xu, L. Qiao, H. Zhu, and W. Wang, “Simultaneous wavelength-and mode-division (de) multiplexing for high-capacity on-chip data transmission link,” *IEEE Photonics J.*, vol. 8, no. 2, pp. 1–10, 2016.

[16] L. Han, B. P.-P. Kuo, N. Alic, and S. Radic, “Ultra-broadband multimode 3dB optical power splitter using an adiabatic coupler and a Y-branch,” *Opt. Express*, vol. 26, no. 11, pp. 14800–14809, 2018.

[17] M. B. Rahaim and T. D. Little, “Toward practical integration of dual-use VLC within 5G networks,” *IEEE Wirel. Commun.*, vol. 22, no. 4, pp. 97–103, 2015.

[18] M. Ayyash *et al.*, “Coexistence of WiFi and LiFi toward 5G: concepts, opportunities, and challenges,” *IEEE Commun. Mag.*, vol. 54, no. 2, pp. 64–71, 2016.

[19] P. Ge, X. Liang, J. Wang, C. Zhao, X. Gao, and Z. Ding, “Optical filter designs for multi-color visible light communication,” *IEEE Trans. Commun.*, vol. 67, no. 3, pp. 2173–2187, 2018.

[20] J. Bashir, E. Peter, and S. R. Sarangi, “A survey of on-chip optical interconnects,” *ACM Comput. Surv. CSUR*, vol. 51, no. 6, p. 115, 2019.

[21] M. A. Taubenblatt, “Optical interconnects for large scale computing systems: Trends and challenges,” in *Photonic Networks and Devices*, 2018, p. NeTh3F. 2.

[22] H. Jia, T. Zhou, X. Fu, J. Ding, L. Zhang, and L. Yang, “Four-port mode-selective silicon optical router for on-chip optical interconnect,” *Opt. Express*, vol. 26, no. 8, pp. 9740–9748, 2018.

[23] S. Libertino and A. Sciuto, “Electro-Optical Modulators in Silicon,” in *Optical Interconnects*, vol. 119, L. Pavesi and G. Guillot, Eds. Berlin, Heidelberg: Springer Berlin Heidelberg, 2006, pp. 53–95.

[24] “Multi Mode Interferrometers — IPKISS 3.1 documentation.” [Online]. Available: http://docs.lucedaphotonics.com/3.1/picazzo/filters/mmi/index.html. [Accessed: 24-Jul-2019].

[25] P. Cheben, R. Halir, J. H. Schmid, H. A. Atwater, and D. R. Smith, “Subwavelength integrated photonics,” *Nature*, vol. 560, no. 7720, p. 565, Aug. 2018, doi: 10.1038/s41586-018-0421-7.

[26] K. Okamoto, *Fundamentals of optical waveguides*, 2nd ed. Amsterdam ; Boston: Elsevier, 2006.
[27] M. Liu *et al.*, "A graphene-based broadband optical modulator," *Nature*, vol. 474, no. 7349, pp. 64–67, Jun. 2011, doi: 10.1038/nature10067.
[28] G. Kovacevic, C. Phare, S. Y. Set, M. Lipson, and S. Yamashita, "Ultra-high-speed graphene optical modulator design based on tight field confinement in a slot waveguide," *Appl. Phys. Express*, vol. 11, no. 6, p. 065102, May 2018, doi: 10.7567/APEX.11.065102.
[29] D. K. Gramotnev and S. I. Bozhevolnyi, "Plasmonics beyond the diffraction limit," *Nat. Photonics*, vol. 4, no. 2, pp. 83–91, Feb. 2010, doi: 10.1038/nphoton.2009.282.
[30] V. E. Babicheva, A. Boltasseva, and A. V. Lavrinenko, "Transparent conducting oxides for electro-optical plasmonic modulators," *Nanophotonics*, vol. 4, no. 1, Jan. 2015, doi: 10.1515/nanoph-2015-0004.
[31] F. Michelotti, L. Dominici, E. Descrovi, N. Danz, and F. Menchini, "Thickness dependence of surface plasmon polariton dispersion in transparent conducting oxide films at 1.55 µm," *Opt. Lett.*, vol. 34, no. 6, pp. 839–841, 2009.
[32] E. Feigenbaum, K. Diest, and H. A. Atwater, "Unity-Order Index Change in Transparent Conducting Oxides at Visible Frequencies," *Nano Lett.*, vol. 10, no. 6, pp. 2111–2116, Jun. 2010, doi: 10.1021/nl1006307.
[33] A. Melikyan *et al.*, "Surface plasmon polariton absorption modulator," *Opt. Express*, vol. 19, no. 9, pp. 8855–8869, 2011.
[34] C. Lin and A. S. Helmy, "Dynamically reconfigurable nanoscale modulators utilizing coupled hybrid plasmonics," *Sci. Rep.*, vol. 5, no. 1, Dec. 2015, doi: 10.1038/srep12313.
[35] G. Sinatkas, A. Pitilakis, D. C. Zografopoulos, R. Beccherelli, and E. E. Kriezis, "Transparent conducting oxide electro-optic modulators on silicon platforms: A comprehensive study based on the drift-diffusion semiconductor model," *J. Appl. Phys.*, vol. 121, no. 2, p. 023109, Jan. 2017, doi: 10.1063/1.4973896.
[36] J.-S. Kim and J. T. Kim, "Silicon electro-optic modulator based on an ITO-integrated tunable directional coupler," *J. Phys. Appl. Phys.*, vol. 49, no. 7, p. 075101, Feb. 2016, doi: 10.1088/0022-3727/49/7/075101.
[37] A. O. Zaki, K. Kirah, and M. A. Swillam, "Hybrid plasmonic electro-optical modulator," *Appl. Phys. A*, vol. 122, no. 4, Apr. 2016, doi: 10.1007/s00339-016-9843-y.
[38] Jin Tae Kim, "Silicon Optical Modulators Based on Tunable Plasmonic Directional Couplers," *IEEE J. Sel. Top. Quantum Electron.*, vol. 21, no. 4, pp. 184–191, Jul. 2015, doi: 10.1109/JSTQE.2014.2346623.
[39] M. Y. Abdelatty, M. M. Badr, and M. A. Swillam, "Compact Silicon Electro-Optical Modulator Using Hybrid ITO Tri-Coupled Waveguides," *J. Light. Technol.*, vol. 36, no. 18, pp. 4198–4204, Sep. 2018, doi: 10.1109/JLT.2018.2863571.
[40] M. Y. Abdelatty, "High-speed hybrid plasmonic electro-optical absorption modulator exploiting epsilon-near-zero effect in indium-tin-oxide," *J. Nanophotonics*, vol. 12, no. 03, p. 1, Aug. 2018, doi: 10.1117/1.JNP.12.036011.
[41] M. A. Swillam, A. O. Zaki, K. Kirah, and L. A. Shahada, "On Chip Optical Modulator using Epsilon-Near-Zero Hybrid Plasmonic Platform," *Sci. Rep.*, vol. 9, no. 1, p. 6669, Dec. 2019, doi: 10.1038/s41598-019-42675-z.
[42] H. Mekawey, Y. Ismail, and M. A. Swillam, "Dynamic routing control through bends for Si sub-micrometer optical interconnects," presented at the SPIE OPTO, San Francisco, California, United States, 2017, p. 101081F, doi: 10.1117/12.2250638.
[43] C. Vernoux *et al.*, "Flexible long-range surface plasmon polariton single-mode waveguide for optical interconnects," *Opt. Mater. Express*, vol. 8, no. 2, p. 469, Feb. 2018, doi: 10.1364/OME.8.000469.
[44] S.-C. Hung, S.-J. Lin, J.-J. Chao, C.-Y. Chang, M.-J. Lin, and C.-F. Lin, "Formation of Crystalline Si Optical Waveguides on Bulk (100) Si Substrate as a New Platform for On-Chip Interconnect Applications," *J. Light. Technol.*, vol. 35, no. 11, pp. 2266–2272, Jun. 2017, doi: 10.1109/JLT.2016.2646381.
[45] Y. Ding *et al.*, "Efficient graphene based electro-optical modulator enabled by interfacing plasmonic slot and silicon waveguides," p. 14.
[46] C. Wang, M. Zhang, B. Stern, M. Lipson, and M. Lončar, "Nanophotonic lithium niobate electro-optic modulators," *Opt. Express*, vol. 26, no. 2, p. 1547, Jan. 2018, doi: 10.1364/OE.26.001547.
[47] Z. Yu, J. Zheng, P. Xu, W. Zhang, and Y. Wu, "Ultracompact Electro-Optical Modulator-Based $Ge_2 Sb_2 Te_5$ on Silicon," *IEEE Photonics Technol. Lett.*, vol. 30, no. 3, pp. 250–253, Feb. 2018, doi: 10.1109/LPT.2017.2783928.

[48] N. H. Fouad, A. O. Zaki, D. C. Zografopoulos, R. Beccherelli, and M. A. Swillam, "Low power hybrid plasmonic microring-on-disks electro-optical modulators," *J. Nanophotonics*, vol. 11, no. 1, p. 016014, Mar. 2017, doi: 10.1117/1.JNP.11.016014.

[49] D. C. Zografopoulos, M. A. Swillam, and R. Beccherelli, "Electro-optic modulators based on hybrid plasmonic micro-ring-disk resonators with femtojoule switching energy," *Appl. Phys. A*, vol. 122, no. 12, p. 1039, Dec. 2016, doi: 10.1007/s00339-016-0529-2.

[50] I. Demirtzioglou *et al.*, "Frequency comb generation in a silicon ring resonator modulator," *Opt. Express*, vol. 26, no. 2, p. 790, Jan. 2018, doi: 10.1364/OE.26.000790.

[51] Z. Wang *et al.*, "Resonance control of a silicon micro-ring resonator modulator under high-speed operation using the intrinsic defect-mediated photocurrent," *Opt. Express*, vol. 25, no. 20, p. 24827, Oct. 2017, doi: 10.1364/OE.25.024827.

[52] T. Baba *et al.*, "50-Gb/s ring-resonator-based silicon modulator," *Opt. Express*, vol. 21, no. 10, p. 11869, May 2013, doi: 10.1364/OE.21.011869.

[53] H. Fujiwara and M. Kondo, "Effects of carrier concentration on the dielectric function of ZnO:Ga and In 2 O 3 : Sn studied by spectroscopic ellipsometry: Analysis of free-carrier and band-edge absorption," *Phys. Rev. B*, vol. 71, no. 7, Feb. 2005, doi: 10.1103/PhysRevB.71.075109.

[54] R. Soref and B. Bennett, "Electrooptical effects in silicon," *IEEE J. Quantum Electron.*, vol. 23, no. 1, pp. 123–129, Jan. 1987, doi: 10.1109/JQE.1987.1073206.

[55] R. Deng *et al.*, "Modulation of carrier concentration and microstructure for high performance Bi x Sb 2-x Te 3 thermoelectrics prepared by rapid solidification," *J. Solid State Chem.*, vol. 264, pp. 141–147, Aug. 2018, doi: 10.1016/j.jssc.2018.04.038.

[56] A. A. R. Mohamed, L. A. Shahada, and M. A. Swillam, "Electro-Optic Plasmonic Modulator With Direct Coupling to Silicon Waveguides," *IEEE Photonics J.*, vol. 9, no. 6, pp. 1–7, Dec. 2017, doi: 10.1109/JPHOT.2017.2757014.

[57] A. Abbas and M. Swillam, "Electro-optic polymeric reflection modulator based on plasmonic metamaterial," in *Organic Photonic Materials and Devices XX*, San Francisco, United States, 2018, p. 49, doi: 10.1117/12.2300567.

[58] M. Ayata *et al.*, "High-speed plasmonic modulator in a single metal layer," *Science*, vol. 358, no. 6363, p. 630, Nov. 2017, doi: 10.1126/science.aan5953.

[59] M. Y. Abdelatty, A. O. Zaki, and M. A. Swillam, "Hybrid silicon plasmonic organic directional coupler-based modulator," *Appl. Phys. A*, vol. 123, no. 1, Jan. 2017, doi: 10.1007/s00339-016-0656-9.

[60] C. Hoessbacher *et al.*, "Optical Interconnect Solution With Plasmonic Modulator and Ge Photodetector Array," *IEEE Photonics Technol. Lett.*, vol. 29, no. 21, pp. 1760–1763, Nov. 2017, doi: 10.1109/LPT.2017.2723727.

[61] C. Hoessbacher *et al.*, "Plasmonic modulator with >170 GHz bandwidth demonstrated at 100 GBd NRZ," *Opt. Express*, vol. 25, no. 3, p. 1762, Feb. 2017, doi: 10.1364/OE.25.001762.

[62] D. C. Zografopoulos *et al.*, "Amplitude modulation in infrared metamaterial absorbers based on electro-optically tunable conducting oxides," *Appl. Phys. A*, vol. 124, no. 2, p. 105, Feb. 2018, doi: 10.1007/s00339-017-1506-0.

[63] K. Shi, R. R. Haque, B. Zhao, R. Zhao, and Z. Lu, "Broadband electro-optical modulator based on transparent conducting oxide," *Opt. Lett.*, vol. 39, no. 17, p. 4978, Sep. 2014, doi: 10.1364/OL.39.004978.

[64] F. X. Fu Xu and Y. S. Yu Sun, "Efficient second harmonic generation between photonic and plasmonic modes in a tunable transparent conducting oxide waveguide," *Chin. Opt. Lett.*, vol. 14, no. 3, pp. 031901–031904, 2016, doi: 10.3788/COL201614.031901.

[65] Y.-W. Huang *et al.*, "Gate-Tunable Conducting Oxide Metasurfaces," *Nano Lett.*, vol. 16, no. 9, pp. 5319–5325, Sep. 2016, doi: 10.1021/acs.nanolett.6b00555.

[66] X. Hu, Q. Chen, L. Wen, L. Jin, H. Wang, and W. Liu, "Modulating Spatial Light by Grating Slot Waveguides With Transparent Conducting Oxides," *IEEE Photonics Technol. Lett.*, vol. 28, no. 15, pp. 1665–1668, Aug. 2016, doi: 10.1109/LPT.2016.2565507.

[67] K. Shi and Z. Lu, "Optical modulators and beam steering based on electrically tunable plasmonic material," *J. Nanophotonics*, vol. 9, no. 1, pp. 093793–093793, 2015.

[68] V. J. Sorger, N. D. Lanzillotti-Kimura, R.-M. Ma, and X. Zhang, "Ultra-compact silicon nanophotonic modulator with broadband response," *Nanophotonics*, vol. 1, no. 1, Jan. 2012, doi: 10.1515/nanoph-2012-0009.

[69] D. B. Tice, S.-Q. Li, M. Tagliazucchi, D. B. Buchholz, E. A. Weiss, and R. P. H. Chang, "Ultrafast Modulation of the Plasma Frequency of Vertically Aligned Indium Tin Oxide Rods," *Nano Lett.*, vol. 14, no. 3, pp. 1120–1126, Mar. 2014, doi: 10.1021/nl4028044.

[70] M. M. Badr, M. Y. Abdelatty, and M. A. Swillam, “Ultra-fast Silicon Electro-optic Modulator based on ITO-integrated Directional Coupler,” *Phys. Scr.*, 2019, doi: 10.1088/1402-4896/ab0ce1.

[71] U. Koch, C. Hoessbacher, J. Niegemann, C. Hafner, and J. Leuthold, “Digital Plasmonic Absorption Modulator Exploiting Epsilon-Near-Zero in Transparent Conducting Oxides,” *IEEE Photonics J.*, vol. 8, no. 1, pp. 1–13, Feb. 2016, doi: 10.1109/JPHOT.2016.2518861.

[72] Y. Ismail, H. Mekawey, R. Gamal, and M. A. Swillam, “Potential of slot waveguides for silicon-based optical interconnects,” *SPIE Newsroom*, Mar. 2017, doi: 10.1117/2.1201611.006750.

[73] Z. Sun, A. Martinez, and F. Wang, “Optical modulators with 2D layered materials,” *Nat. Photonics*, vol. 10, no. 4, p. 227, Apr. 2016, doi: 10.1038/nphoton.2016.15.

[74] L.-L. Yu *et al.*, “Plasma optical modulators for intense lasers,” *Nat. Commun.*, vol. 7, p. 11893, Jun. 2016, doi: 10.1038/ncomms11893.

[75] L. Zhou, Y. Zhou, M. Wang, Y. Zhong, Y. Xia, and J. Chen, “Microwave Signal Processing using High Speed Silicon Optical Modulators,” in *Asia Communications and Photonics Conference*, 2016, pp. AS2E–2.

[76] W. Yao, G. Gilardi, M. K. Smit, and M. J. Wale, “Performance Degradation of Integrated Optical Modulators Due to Electrical Crosstalk,” *J. Light. Technol.*, vol. 34, no. 13, pp. 3080–3086, Jul. 2016, doi: 10.1109/JLT.2016.2572222.

[77] J. Cervantes-L, D. I. Serrano-Garcia, Y. Otani, and B. Cense, “Mueller-matrix modeling and characterization of a dual-crystal electro-optic modulator,” *Opt. Express*, vol. 24, no. 21, p. 24213, Oct. 2016, doi: 10.1364/OE.24.024213.

[78] Q. Xu, B. Schmidt, S. Pradhan, and M. Lipson, “Micrometre-scale silicon electro-optic modulator,” *Nature*, vol. 435, no. 7040, pp. 325–327, May 2005, doi: 10.1038/nature03569.

[79] G. T. Reed, G. Mashanovich, F. Y. Gardes, and D. J. Thomson, “Silicon optical modulators,” *Nat. Photonics*, vol. 4, no. 8, pp. 518–526, Aug. 2010, doi: 10.1038/nphoton.2010.179.

[80] M. R. Watts, W. A. Zortman, D. C. Trotter, R. W. Young, and A. L. Lentine, “Vertical junction silicon microdisk modulators and switches,” *Opt. Express*, vol. 19, no. 22, pp. 21989–22003, 2011.

[81] J.-H. Han, F. Boeuf, S. Takagi, and M. Takenaka, “High-modulation-efficiency InGaAsP/Si hybrid MOS optical modulator with Mach-Zehnder interferometer,” *ArXiv Prepr. ArXiv170202245*, 2017.

[82] M. Shahzad *et al.*, “Infrared surface plasmons on heavily doped silicon,” *J. Appl. Phys.*, vol. 110, no. 12, p. 123105, Dec. 2011, doi: 10.1063/1.3672738.

[83] D. Chatzidimitriou, G. Sinatkas, T. Christopoulos, A. Pitilakis, E. E. Kriezis, and O. Tsilipakos, “Carrier-controlled nanophotonic components for routing and modulation operations,” in *2016 5th International Conference on Modern Circuits and Systems Technologies (MOCAST)*, 2016, pp. 1–4, doi: 10.1109/MOCAST.2016.7495141.

[84] J. Liu *et al.*, “Flexible terahertz modulator based on coplanar-gate graphene field-effect transistor structure,” *Opt. Lett.*, vol. 41, no. 4, p. 816, Feb. 2016, doi: 10.1364/OL.41.000816.

[85] Y. Hu *et al.*, “Broadband 10 Gb/s operation of graphene electro-absorption modulator on silicon,” *Laser Photonics Rev.*, vol. 10, no. 2, pp. 307–316, 2016.

[86] N. Kinsey, C. DeVault, J. Kim, M. Ferrera, V. M. Shalaev, and A. Boltasseva, “Epsilon-near-zero Al-doped ZnO for ultrafast switching at telecom wavelengths,” *Optica*, vol. 2, no. 7, p. 616, Jul. 2015, doi: 10.1364/OPTICA.2.000616.

[87] K. Shi and Z. Lu, “Field-effect optical modulation based on epsilon-near-zero conductive oxide,” *Opt. Commun.*, vol. 370, pp. 22–28, Jul. 2016, doi: 10.1016/j.optcom.2016.02.062.

[88] “MODE Solutions | Waveguide Mode Solver and Propagation Simulator.” [Online]. Available: https://www.lumerical.com/tcad-products/mode/. [Accessed: 27-Sep-2018].

[89] “COMSOL Multiphysics® Modeling Software.” [Online]. Available: https://www.comsol.com/. [Accessed: 27-Sep-2018].

[90] P. Mazzoldi and C. Sada, “A trip in the history and evolution of ion-exchange process,” *Mater. Sci. Eng. B*, vol. 149, no. 2, pp. 112–117, Mar. 2008, doi: 10.1016/j.mseb.2007.11.038.

[91] S. S. Kistler, “Stresses in Glass Produced by Nonuniform Exchange of Monovalent Ions,” *J. Am. Ceram. Soc.*, vol. 45, no. 2, pp. 59–68, 1962, doi: 10.1111/j.1151-2916.1962.tb11081.x.

[92] A. K. Varshneya, “Chemical Strengthening of Glass: Lessons Learned and Yet To Be Learned,” *Int. J. Appl. Glass Sci.*, vol. 1, no. 2, pp. 131–142, 2010, doi: 10.1111/j.2041-1294.2010.00010.x.

[93] T. Izawa and H. Nakagome, “Optical waveguide formed by electrically induced migration of ions in glass plates,” *Appl. Phys. Lett.*, vol. 21, no. 12, pp. 584–586, Dec. 1972, doi: 10.1063/1.1654265.

[94] T. G. Giallorenzi, E. J. West, R. Kirk, R. Ginther, and R. A. Andrews, “Optical Waveguides Formed by Thermal Migration of Ions in Glass,” *Appl. Opt.*, vol. 12, no. 6, pp. 1240–1245, Jun. 1973, doi: 10.1364/AO.12.001240.

[95] A. H. Reshak, K. N. Khor, M. M. Shahimin, and S. A. Z. Murad, “Copper ion-exchanged channel waveguides optimization for optical trapping,” *Prog. Biophys. Mol. Biol.*, vol. 112, no. 3, pp. 118–123, Aug. 2013, doi: 10.1016/j.pbiomolbio.2013.05.003.

[96] A. Choudhary, S. Dhingra, B. D’Urso, P. Kannan, and D. P. Shepherd, “Graphene Q-Switched Mode-Locked and Q-Switched Ion-Exchanged Waveguide Lasers,” *IEEE Photonics Technol. Lett.*, vol. 27, no. 6, pp. 646–649, Mar. 2015, doi: 10.1109/LPT.2015.2389631.

[97] F. Wang, B. Chen, E. Y. B. Pun, and H. Lin, “Alkaline aluminum phosphate glasses for thermal ion-exchanged optical waveguide,” *Opt. Mater.*, vol. 42, pp. 484–490, Apr. 2015, doi: 10.1016/j.optmat.2015.02.007.

[98] S. de Bonnault, D. Bucci, P.-J. Zermatten, P. G. Charette, and J. E. Broquin, “Hybrid metallic ion-exchanged waveguides for SPR biological sensing,” in *Integrated Optics: Devices, Materials, and Technologies XIX*, 2015, vol. 9365, p. 93650D, doi: 10.1117/12.2077648.

[99] L. F. Shen, B. J. Chen, H. Lin, and E. Y. B. Pun, “Praseodymium ion doped phosphate glasses for integrated broadband ion-exchanged waveguide amplifier,” *J. Alloys Compd.*, vol. 622, pp. 1093–1097, Feb. 2015, doi: 10.1016/j.jallcom.2014.11.033.

[100] X.-J. Cui, L.-L. Wang, H.-K. Zhang, and T. Chen, “<!-- *** Custom HTML *** -->$KTiOPO_4$ double barrier optical waveguides produced by Rb^+-K^+ ion exchange and subsequent He^+-ion irradiation,” *Opt. Eng.*, vol. 55, no. 3, p. 036107, Mar. 2016, doi: 10.1117/1.OE.55.3.036107.

[101] R. Terai and R. Hayami, “Ionic diffusion in glasses,” *J. Non-Cryst. Solids*, vol. 18, no. 2, pp. 217–264, Sep. 1975, doi: 10.1016/0022-3093(75)90022-8.

[102] R. V. Ramaswamy and R. Srivastava, “Ion-exchanged glass waveguides: a review,” *J. Light. Technol.*, vol. 6, no. 6, pp. 984–1000, Jun. 1988, doi: 10.1109/50.4090.

[103] S. Honkanen *et al.*, “Recent advances in ion exchanged glass waveguides and devices,” Apr-2006. [Online]. Available: https://www.ingentaconnect.com/content/sgt/ejgst/2006/00000047/00000002/art00008. [Accessed: 17-Jul-2019].

[104] J.-E. Broquin, “Glass integrated optics: state of the art and position toward other technologies,” in *Integrated Optics: Devices, Materials, and Technologies XI*, 2007, vol. 6475, p. 647507, doi: 10.1117/12.706785.

[105] A. Tervonen, S. K. Honkanen, and B. R. West, “Ion-exchanged glass waveguide technology: a review,” *Opt. Eng.*, vol. 50, no. 7, p. 071107, Jul. 2011, doi: 10.1117/1.3559213.

[106] G. C. Righini and A. Chiappini, “Glass optical waveguides: a review of fabrication techniques,” *Opt. Eng.*, vol. 53, no. 7, p. 071819, Mar. 2014, doi: 10.1117/1.OE.53.7.071819.

[107] H. Saarikoski, R.-P. Salmio, J. Saarinen, T. Eirola, and A. Tervonen, “Fast numerical solution of nonlinear diffusion equation for the simulation of ion-exchanged micro-optics components in glass,” *Opt. Commun.*, vol. 134, no. 1, pp. 362–370, Jan. 1997, doi: 10.1016/S0030-4018(96)00552-4.

[108] P. Y. Choo, J. A. Frantz, J. T. A. Carriere, D. L. Mathine, R. K. Kostuk, and N. N. Peyghambarian, “Measurement and modeling of ion-exchange parameters for IOG-10 glass,” *Opt. Eng.*, vol. 42, no. 10, pp. 2812–2816, Oct. 2003, doi: 10.1117/1.1605736.

[109] B. R. West, P. Madasamy, N. Peyghambarian, and S. Honkanen, “Modeling of ion-exchanged glass waveguide structures,” *J. Non-Cryst. Solids*, vol. 347, no. 1, pp. 18–26, Nov. 2004, doi: 10.1016/j.jnoncrysol.2004.09.013.

[110] S. Sebastiani, S. Berneschi, M. Brenci, G. Nunzi-Conti, S. Pelli, and G. C. Righini, “Simple approach to calculate the refractive index profile of ion-exchanged waveguides,” *Opt. Eng.*, vol. 44, no. 5, p. 054602, May 2005, doi: 10.1117/1.1914802.

[111] G. Li, K. A. Winick, H. C. Griffin, and J. S. Hayden, “Systematic modeling study of channel waveguide fabrication by thermal silver ion exchange,” *Appl. Opt.*, vol. 45, no. 8, pp. 1743–1755, Mar. 2006, doi: 10.1364/AO.45.001743.

[112] M. A. Swillam, D. A. Khalil, and A. H. Morshed, “Effect of the fabrication and design parameters on the performance of multimode interference devices made by ion exchange: a detailed study,” *J. Opt. Pure Appl. Opt.*, vol. 10, no. 12, p. 125301, Oct. 2008, doi: 10.1088/1464-4258/10/12/125301.

[113] M. M. Badr and M. A. Swillam, “Solving the nonlinear diffusion model of the ion exchange process using finite element method,” in *Proc. of SPIE Vol*, 2017, vol. 10098, pp. 100981X–1.

[114] Y. Haven and J. Stevels, “Note on the mechanism of ionic transport in glass,” in *Proc. 4th Int. Congress on Glass*, 1965, vol. 343.

[115] J. Albert and J. W. Y. Lit, “Full modeling of field-assisted ion exchange for graded index buried channel optical waveguides,” *Appl. Opt.*, vol. 29, no. 18, pp. 2798–2804, Jun. 1990, doi: 10.1364/AO.29.002798.

[116] G. Stewart and P. Laybourn, “Fabrication of ion-exchanged optical waveguides from dilute silver nitrate melts,” *IEEE J. Quantum Electron.*, vol. 14, no. 12, pp. 930–934, 1978.
[117] “University Wafer - The Leading Supplier of Silicon Wafers and other Semiconductorss,” 01-Oct-2018. [Online]. Available: https://www.universitywafer.com. [Accessed: 29-Dec-2019].
[118] “Application Notes for photolitografy with technical informations for photoresists, solvents, developers and etchants.” [Online]. Available: https://www.microchemicals.com/downloads/application_notes.html. [Accessed: 30-Dec-2019].